# Bioinspired functional SLIPSs and wettability gradient surfaces and their synergistic cooperation and opportunities for enhanced condensate and fluid transport

# Bioinspired functional SLIPSs and wettability gradient surfaces and their synergistic cooperation and opportunities for enhanced condensate and fluid transport

Fengyong Lv [a] *, Fang Zhao [a], Daolai Cheng [a], Zhiguang Dong [a], Hongwei Jia [b], Xin Xiao [b,c] †, Daniel Orejon [d,e] ‡

[a] School of Urban Construction and Safety Engineering, Shanghai Institute of Technology, Shanghai 201418, China

[b] School of Environmental Science and Engineering, Donghua University, Shanghai 201620, China

[c] Shanghai Institute of Pollution Control and Ecological Security, Shanghai, 200092, China

[d] Institute for Multiscale Thermofluids, School of Engineering, The University of Edinburgh, Edinburgh EH9 3FD, Scotland, UK

[e] International Institute for Carbon-Neutral Energy Research (WPI-I2CNER), Kyushu University, 744 Motooka, Nishi-ku, Fukuoka 819-0395, Japan

## Abstract

Bioinspired smart functional surfaces have received increasing attention in recent years owed to their tunable wettability and enhanced droplet transport suggesting them as excellent candidates for industrial and nanotechnology-related applications. More specifically, bioinspired slippery lubricant infused porous surfaces (SLIPSs) have been proposed for their low adhesion enabling continuous dropwise condensation (DWC) even of low-surface tension fluids. Functional surfaces with chemical and/or structural wettability gradients have also been exploited empowering spontaneous droplet transport in a controlled manner. Current research has focused on the better understanding of the mechanisms and intimate interactions taking place between liquid droplets and functional surfaces or on the forces imposed by differences in surface wettability and/or by Laplace pressure owed to chemical or structural gradients. Nonetheless, less attention has been paid to the synergistic cooperation of efficiently driving droplet transport via chemical and/or structural patterns on a low surface energy/adhesion background imposed by SLIPSs, with the consequent promising potential for microfluidics and condensation heat transfer applications amongst others. This review provides a detailed and timely overview and summary on recent advances and developments on bioinspired

* Corresponding author. Email address: fengyonglv@126.com (F. Y. Lv)

† Corresponding author. Email address: xin.xiao@dhu.edu.cn (X. Xiao)

‡ Corresponding author. Email address: D.Orejon@ed.ac.uk (D. Orejon)

SLIPSs and on wettability gradient surfaces with focus on their synergistic cooperation for condensation and fluid transport related applications. Firstly, the fundamental theory and mechanisms governing complex droplet transport on homogeneous, on wettability gradient surfaces and on inclined SLIPSs are introduced. Secondly, recent advances on the fabrication and characterization of SLIPSs and functional surfaces are presented. Then, the condensation performance on such functional surfaces comprising chemical or structural wettability gradients is reviewed and their applications on condensation heat transfer are summarized. Last a summary outlook highlighting the opportunities and challenges on the synergistic cooperation of SLIPSs and wettability gradient surfaces for heat transfer as well as future perspective in modern applications are presented.

**Keywords:**

Slippery lubricant infused porous surfaces SLIPSs; Bioinspired functional surfaces; Structural and/or chemical wettability gradients; Driving force; Directional transport; Condensation heat transfer enhancement

**Highlights:**

- Recent progress on bioinspired SLIPSs and chemical/structured gradient surfaces is reviewed
- Wettability gradient surfaces provide an additional driving force facilitating droplet transport
- SLIPSs reduce droplet-surface interactions inducing continuous and spontaneous droplet self-removal.
- Synergistic cooperation of wettability gradient surfaces and SLIPSs are considered
- Opportunities on wettability gradient surfaces and SLIPS for condensation and energy related applications are highlighted

## Table of Contents

## 1. Introduction

With the rapid development of modern society, the concern of efficient thermal management and the sustainable and efficient utilization of energy have attracted extensive attention from the scientific community and industry[1]. Energy is one of the most pressing challenges the society is facing at a global level and ensuring affordable and sustainable access for all is contemplated within the United Nations Sustainable Development Goal 7: Affordable and clean Energy[2]. More in particular, condensation phase-change heat transfer, microfluidics, water harvesting, anti-icing, water treatment, desalination and/or self-cleaning represents a huge potential in enhancing energy-savings for energy-related applications amongst others. Aiming to enhance the performance of such applications via surface modification empowering low adhesion, accurate fluid transport, enhanced heat transfer, etc., amongst others, advanced surfaces enabling a wide range of capabilities and functionalities are excellent candidates[3, 4]. To achieve such functional surfaces wettability and/or surface structuring are the common routes and approaches, which will be specifically introduced in this review. Advanced functional surfaces have also the potential to contribute to the United Nations Sustainable Development Goal 6: Clean Water and Sanitation[2]. The relevance of advance functional surfaces to a plethora of everyday life and industrial applications is then established.

In the particular case of condensation phase-change, wettability and surface structure play a paramount role on the final morphology of the condensate that is typically classified into two categories[5]: filmwise condensation (FWC) and dropwise condensation (DWC)[6-9]. When looking into the heat transfer performance, up to one order of magnitude greater coefficients are reported for DWC when compared to FWC[7, 9-13]. The effective implementation of high efficient functional and advanced surfaces performing in a DWC fashion, can in turn increase the overall efficiency of a fire coal power plant in up to 1%[14] and reduce the energy consumption in modern data centers, which could prompt savings in the order of hundreds of megatons of equivalent $CO_2$ emissions worldwide just from power generation alone[15]. On one hand FWC ensues on high energy surfaces, i.e. high surface wettability[16-18], such as metal surfaces traditionally used in industry in the condenser side[19]. On such high wettability surfaces, the condensate nucleates and grows forming a condensate film that spreads on the surface and gradually deteriorates the heat transfer performance because of its large thermal resistance[6]. On the other hand, DWC typically occurs on low energy advanced functional surfaces, i.e., low surface wettability, such as smooth hydrophobic surfaces[9, 20-22], superhydrophobic surfaces (SHSs)[12, 23-26] and slippery liquid-infused porous surfaces (SLIPSs)[27-31]. Sustained continuous DWC requires rapid shedding of droplets from the advanced functional surface, crucial in improving the

condensation heat transfer performance[32]. On smooth hydrophobic surfaces, condensing droplets grow with advancing contact angles ca. 120° exhibiting a spherical cap, while on SHSs condensing droplets typically grow displaying perfect spherical shapes[33, 34] while they remain on the surface due to the imposed surface adhesion and pinning to the surface[23-25, 35-37]. Then, departure occurs once the gravity acting on the droplet overcomes the hysteresis force[38-41]. As condensation develops, the surface is easily occupied by the condensing droplets, which eventually inhibit the condensation performance as each individual droplet exerts an additional heat transfer resistance between the condensing vapor and the surface[29, 42-44]. More recently, SLIPSs inspired by Nepenthes pitcher plant have been developed exploiting the foundations of SHSs fabrication[45-48]. SLIPSs are typically fabricated by infusing a non-volatile lubricant within the porous micro- and/or nano-structures of the SHS[49]. Owed to the presence of the lubricant in between the structures, the contact angle hysteresis of droplet on SLIPSs is greatly decreased when compared to SHS[50], and the droplet can easily shed from the surface via gravitational forces once the hysteresis is overcome[29, 51]. Of importance is to stress here the smaller droplet departure diameter on SLIPSs when compared to SHS[42]. After a shedding event sweeping the surface takes place, re-nucleation and local increase on heat transfer occurs on the refreshed areas until bigger droplets form on the surface via direct condensation and coalescence[52]. Since condensed droplets with the diameter less than 100 μm are responsible for nearly 85.0% of total heat transfer[53], the detachment of small-sized droplet from the advanced functional surface can obviously enhance the condensation performance, which plays a dominant role in improving the overall performance and heat transfer efficiency in energy-related applications.

Despites the low contact angle hysteresis and low adhesion of the condensate on SLIPSs, droplet shedding frequency may not be high enough to ensure high heat transfer outputs as per their long sweeping periods. For example, a large number of nucleated droplets with sizes in the sub-millimeter range cannot shed from the SLIPS as gravitational force is not high enough to overcome the adhesion to the surface. Hence, controlling and manipulating droplet transport without external energy input is essential to induce the shedding from the advanced functional surface of such small droplets with the consequent enhance in the heat transfer performance[54-56]. Recently, the spontaneous motion of micrometer condensing droplets towards bigger droplets with sizes in the order of hundreds of micrometers has been reported on SLIPSs as per the capillary induced motion of small-sized droplets located within the lubricant meniscus of the bigger-sized ones[53]. Nonetheless, such spontaneous motion cannot be accurately controlled as per the randomness of nucleation and droplet growth during condensation phase-change. In order to counteract such shortcomings, an additional driving force can

be imposed to small-sized droplets in order to induce the effective transport from one region to the desired reservoir. Inspired by the remarkable liquid collection capabilities of natural plants and insects[57, 58], driving forces generated from droplet coalescence, surface structural and/or chemical wettability gradients and Laplace pressure gradients can be imposed to small-sized droplets to induce the desired droplet motion on the advanced functional surface[59, 60]. While coalescence between neighboring small-sized droplets can drive the random movement and positioning of the newly coalesced droplet; chemical or structural gradients (patterned wettability and surface curvature respectively) in addition to well designed surface structures inducing additional Laplace pressure within the droplets, can on the other hand effectively induce the accurate droplet directional transport from one place to region of interest[61-65]. Therefore, the careful design and exploitation of coupling directional transport via wettability gradients during condensation phase-change introduced here represent significant advances and opportunities for microfluidics, interfacial nanotechnology and two-phase heat transfer applications amongst others.

The above perspective indicates that the controlled directional transport and shedding of small-sized droplets on advanced functional surfaces can accelerate the droplet removal and re-nucleation processes playing a critical role in enhancing the condensation heat transfer performance. To this end, bioinspired SLIPSs comprising structural or chemical wettability gradients represent huge potential to interfacial nanotechnology and industrial, in particular to condensation heat transfer-related fields, which have been summarized in **Fig. 1**.

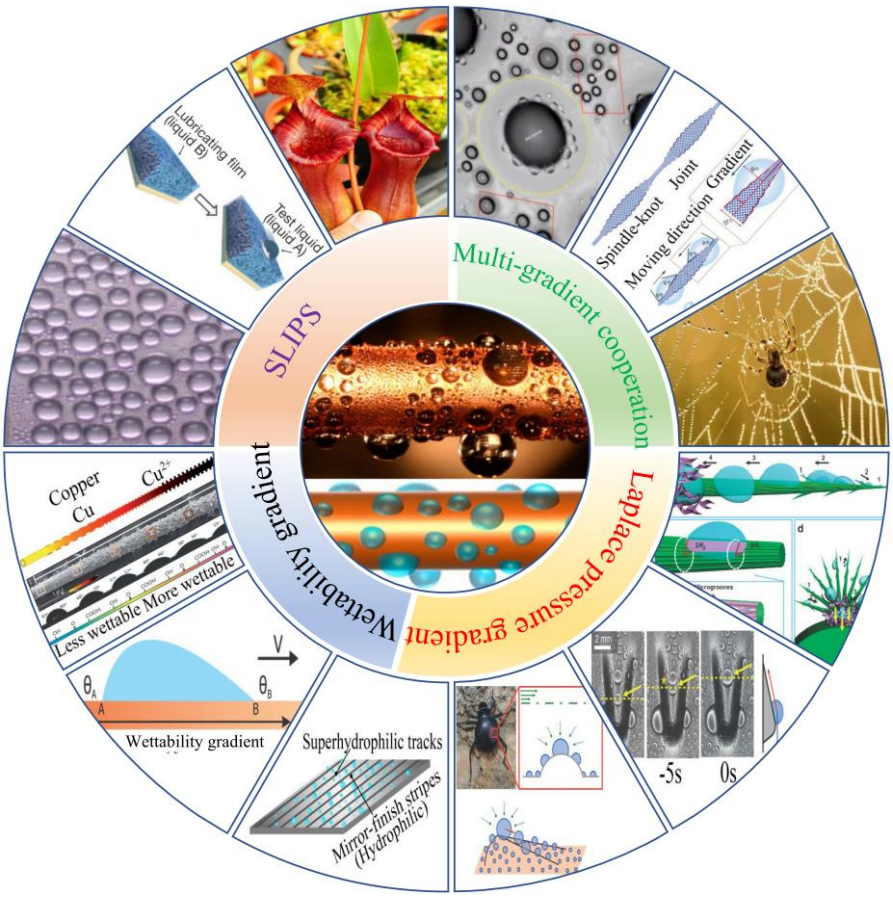


**Fig. 1. State-of-art research on SLIPSs, wettability gradient surfaces, structured surfaces inducing an effective Laplace pressure gradients, and research works including the cooperation effect of multiple effects.**

This paper presents a review of recent progress in bioinspired SLIPSs, chemical and/or structural wettability gradient surfaces, and the combination of implementing chemical and/or structural wettability gradient within SLIPSs, along with their applications, which is arranged as follows. Fundamental theory and state-of-the-art fabrication of bioinspired SLIPSs and chemical and/or structural wettability gradient surfaces are introduced first. Then, the applied investigations inducing the droplet motion as a consequence of an imposed driving force, i.e., structural and/or chemical wettability gradient and/or Laplace pressure, during condensation and the droplet transport are described. Condensation heat transfer-related applications making use of bioinspired SLIPSs and gradient structure are summarized, introduced and discussed for the first time as well. We conclude with a personal overview and potential opportunities on the combination of SLIPSs and structural and/or chemical wettability gradient functional surfaces opening up further research topics and future applications. We note here that other active external forces inducing droplet transport such as Leidenfrost, temperature gradients, acoustic waves, vapor gradients, vibration, and/or magnetic fields are excluded from this review. More details on these manipulation techniques and mechanisms can be found in the recent works of Dai et al.[66], Li et al.[67] and Malinowski et al.[68].

## 2. Fundamentals of droplet directional transport on bioinspired SLIPSs and/or chemical or structural wettability gradients

### 2.1 Fundamentals of wetting and directional droplet transport

Typically, on a horizontal surface a droplet remains stationary on the surface while the morphology and shape of the droplet adopted depends on the physicochemical properties of the surface, i.e., surface structure and wettability, the thermophysical properties of the fluid, i.e., surface tension, and those of the surrounding ambient[69, 70]. On an inclined or a vertical surface a droplet may move under gravitational forces[40, 41]. The balance of forces for a droplet sitting on an inclined solid surface represented in **Fig. 2**(a) involve a gravitational force pulling the droplet downwards $F_g$ while a pinning force or hysteresis force $F_h$ opposes to the movement following Equation 1[40, 41]:

$$F_g - F_h = \rho V g \sin\alpha - \gamma \pi D_b (\cos\theta_r - \cos\theta_a) \quad (1)$$

where $\rho$ and $V$ are the density and the volume of the fluid droplet, $g$ is the gravity acceleration and $\alpha$ is the inclination angle of the surface all relevant to the gravitational forces; while $\gamma$ is the liquid-gas surface tension, $D_b$ is the droplet base diameter and $\theta_a$ and $\theta_r$ are the advancing and receding contact angles respectively dictating the hysteresis force and the eventual pinning force to the surface. For a droplet to move, gravitational forces must overcome hysteresis ones, i.e., $F_g > F_h$.

Aiming to induce controlled droplet motion without the need for gravity and/or external forces applied, surface free energy gradients via chemical and/or structural contrast and/or Laplace pressure gradients have been proposed. On one hand, the seminal work of Chaudhury and Whitesides demonstrated the motion of a droplet uphill, i.e., against gravity, solely due to an imposed patterned wettability[71]. In this work and in subsequent works on microfluidics and droplet manipulation, a driving force $F_w$ owed to wettability or structural gradients overcoming the hysteresis force $F_h$ must be imposed to induce the effective droplet motion where $F_w > F_h$[71, 72]. Surface wettability gradients inducing a driving force and the motion of a droplet from the less wetting to the more wetting region, i.e., from the lower to the higher solid fraction region, aiming to minimize the overall droplet surface energy, can be generated by either a patterned wettability as in **Fig. 2**(b)[73-75], surface structure[72, 76-79] and/or the combination of both wettability and surface structure[80]. In the specific case of wetting driving force $F_w$ arising from a surface wettability gradient represented in **Fig. 2**(b) can be expressed as[71, 81, 82]:

$$F_w = \int_{L_l}^{L_m} \gamma(\cos\theta_a - \cos\theta_r)\, dl \quad (2)$$

where d$l$ is the integrating variable from the less wettable region ($L_l$) to the more wettable region ($L_m$).

In the case of a solely structural gradient on a homogeneous hydrophobic structured background comprising a solid fraction gradient as represented in **Fig. 2**(c), the following wetting driving force $F_w$ derived from the Cassie-Baxter equation can be applied[83, 84]:

$$F_w = (\gamma_{sv} - \gamma_{sl})_R + (\gamma_{sl} - \gamma_{sv})_L = \gamma(\cos\theta_R^* - \cos\theta_L^*) = \gamma(\cos\theta_Y + 1)\Delta\varphi \quad (3)$$

where $\gamma_{sv}$ and $\gamma_{sl}$ are the solid-vapor and the solid-liquid surface tensions, $\theta^*$ and $\theta_Y$ are the effective contact angle given by the Cassie-Baxter equation and the intrinsic contact angle on the smooth hydrophobic surface, and $\Delta\varphi$ is the solid fraction difference between the right R and left L contrasting units. On the other hand, driving force can be also induced by imposing a shape gradient of the surface, i.e., by a conical shape, causing a Laplace pressure gradient between the front and rear wetting fronts, which eventually enables and propels the droplet towards the region with larger curvature radius[85, 86]. The Laplace force $F_{Laplace}$ generated by a conical shape/spine represented in **Fig. 2**(d) can be described as follows[87-89]:

$$F_{Laplace} = -\int_{R_S}^{R_L} S_{TCL} \frac{2\gamma}{(r+R_o)^2} \sin\beta \, dz \quad (4)$$

where $R_o$ and $r$ are the droplet radius and local radius of the conical spine, respectively, $R_S$ and $R_L$ are the local radii of the conical spine at the two opposite fronts of the droplet, respectively, $S_{TCL}$ is the contact area between droplet and conical spine, $\beta$ represents the half apex angle of the conical spine, and d$z$ denotes the integrating variable along the diameter of the conical spine.

As mentioned above, the droplet motion is hindered by the hysteresis force $F_h$ typically quantified by the contact angle hysteresis[87], where smaller contact angle hysteresis is beneficial for the droplet movement and the droplet can move spontaneously once the driving force arising from surface wettability gradient and/or that of the Laplace pressure gradient overcame the hysteresis force. For more details on the mechanisms and advances on droplet transport on solid surfaces the reader is referred to the review of Malinowski et al.[68].

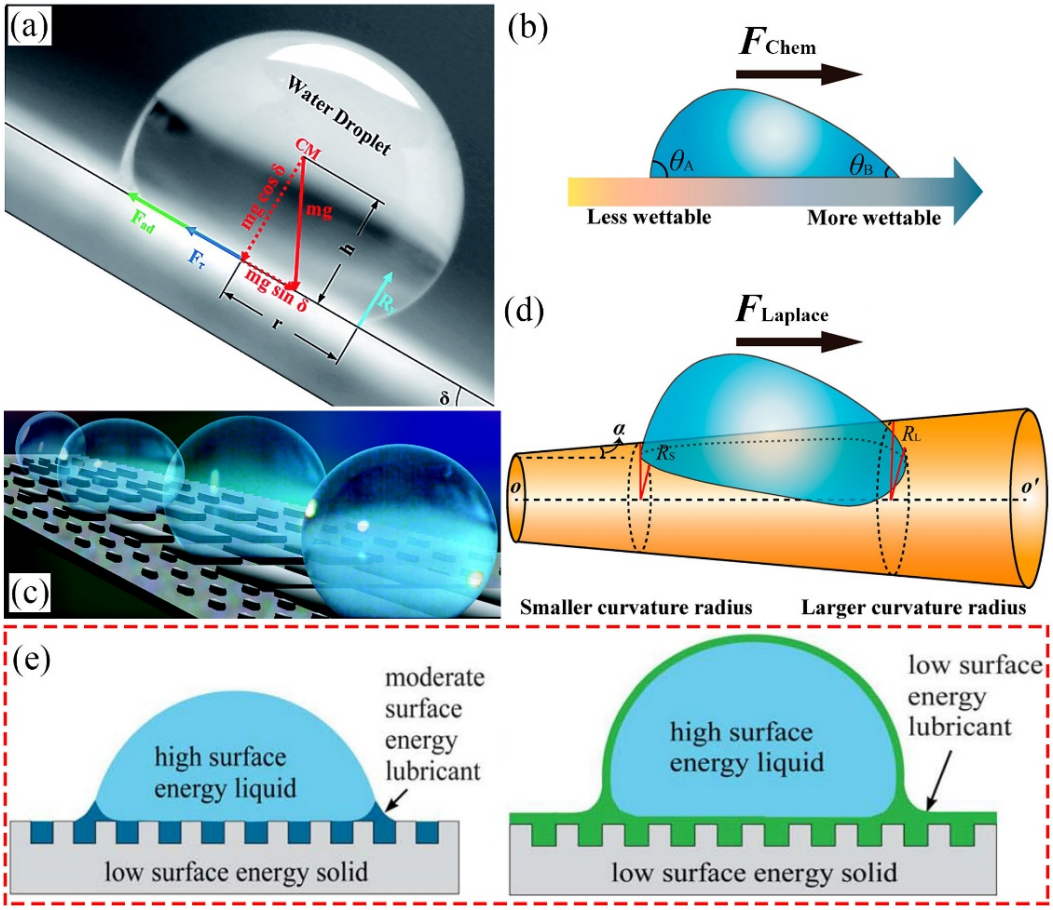


**Fig. 2. The mechanisms of droplet directional transport on bioinspired surfaces and structures. (a) the forces of a droplet sitting on the surface with an inclined angle[90]. Copyright 2017 Royal Society of Chemistry; (b) driving force arising from the surface wettability gradient induces the droplet transport toward more wettable region[85]. Copyright 2014 American Chemical Society; (c) motion of a droplet from low solid fraction to high solid fraction patterned wettability regions[78]. Copyright 2006 American Chemical Society; (d) the driving force generated by the Laplace pressure gradient propels the droplet toward the region with larger curvature radius[85]. Copyright 2006 American Chemical Society; (e) schematic diagram of droplets with and without cloaking oil film[91]. Copyright 2017 Royal Society of Chemistry.**

### 2.2 Fundamentals of wetting on SLIPSs

Next, aiming to decrease contact angle hysteresis, SLIPSs are proposed as per their capabilities of substituting the intimate interactions between the liquid and the solid surface with those of the liquid and an oil or lubricant offering virtually no pinning of the fluid. SLIPSs effectively decrease the difference between the advancing and receding contact angles, i.e., the contact angle hysteresis, and hence, smaller sized droplets are required for the gravity force to overcome that of hysteresis following the force balance presented in Equation 1. Nonetheless, Equation 1 seems to only consider the ternary system air-liquid-solid while in the presence of a lubricant two different triple contact lines: an oil-air-solid and an oil-liquid-solid one can be found. The contact angle hysteresis on the right hand side of the force balance presented in Equation 1 must be then modified to account for the effective interactions between the fluid droplet and the texture and the fluid droplet and the infused oil, as in the

work of Smith et al.[91] presented as Equation 4:

$$F_{\mathrm{g}} - F_{\mathrm{h\_SLIPS}} = \rho V g \sin\alpha - \pi D_{\mathrm{b}} \varphi [\gamma_{\mathrm{ol}} (\cos\theta_{\mathrm{r,os(l)}} - \cos\theta_{\mathrm{a,os(l)}}) + \gamma_{\mathrm{oa}} (\cos\theta_{\mathrm{r,os(a)}} - \cos\theta_{\mathrm{a,os(a)}})] \quad (4)$$

where $\varphi$ is the solid fraction, $\gamma_{\mathrm{ol}}$ and $\gamma_{\mathrm{oa}}$ are the oil-liquid and oil-air interfacial tensions and $\theta_{\mathrm{a,os}}$ and $\theta_{\mathrm{r,os}}$ are the advancing and receding contact angles of the oil-liquid-solid interface (l) and that of the oil-air-solid (a), respectively.

Another important consideration unique to such air-liquid-SLIPS systems is the occurrence or absence of lubricant encapsulation/cloaking the deposited or condensed droplets, as shown in **Fig. 2**(e), which in turn may influence nucleation, wetting, heat transfer and droplet growth, dynamics of coalescence, etc. Next we introduce the adopted criterion to predict the presence or absence of cloaking based on the oil-liquid spreading coefficient $S_{\mathrm{ol}}$ included as Equation 5[91]:

$$S_{ol} = \gamma - \gamma_{ol} - \gamma_{oa} \quad (5)$$

By making use of the different interfacial surface tensions in Equation 5, a positive spreading coefficient $S_{\mathrm{ol}} > 1$ and encapsulation/cloaking of the droplet may occur in the presence of low surface tension lubricants, while a negative coefficient $S_{\mathrm{ol}} < 1$ and absence of cloaking should ensue in the presence of moderate and high surface energy lubricants. Further, in the presence of cloaking, a critical thickness of the cloaking film $\delta_{\mathrm{o}}$ has been proposed as in Equation 6[52, 92, 93]:

$$\delta_{\mathrm{o}} = \sqrt[3]{\frac{\mathrm{A_H R}}{12\pi\gamma}} \quad (6)$$

where $\mathrm{A_H}$ is the Hamaker constant equals ~ $10^{-18}$ J and $R$ is the radius of curvature of the cloaked droplet. For a millimeter sized droplet, the lubricant cloaking film thicknesses reported are in the order of hundred nanometers[52, 92, 94], and it has been reported to affect the steady state evaporation rate of micrometer droplets[95].

From the above theoretical and fundamental backgrounds it is then clear that imposing a wettability gradient either chemical or structural or conical-like structure coupled with a slippery lubricant infused background presents advantages in terms of reduced adhesion and controlled droplet motion.

### 2.3 Basic fundamentals of droplet condensation and transport on natural special organisms

Condensation and droplet transport are ubiquitous phenomenon in the natural environment surrounding us, which plays a decisive role in the survival of natural organisms such as Namib desert beetles[96], cactus spines[86, 97] and spider silks[98]. Condensed droplets formed on the bumps of the beetles shed rapidly from the surface due to the driving force arising from the coupled interaction between the droplet coalescence and capillary force of asymmetric bumps[38, 99]. Continuous droplet

transport has been realized on the natural cactus spines due to the Laplace driving force generated from the conical geometry of the spines, which is exploited for enhanced water harvesting and condensation[86]. In addition to the continuous transport of condensed droplet on cactus spines, natural spider silks were found to be capable of transporting droplets toward the spindle-knots due to the existing of synergistic cooperation of the driving forces arising from the surface wettability gradient between the difference nanofibrils' arrangement of spindle-knots and joints and from the Laplace pressure gradient of the conical geometry of spider silks[85, 98]. Controlling and enhancing vapor condensation and droplet transport are fundamental and play a crucial role on water harvesting, air conditioning, thermal management and transportation[100]. To this end, designing and fabricating SLIPSs coupled with gradient structures inspired from the millennia of evolution from biological entities, represent an attractive alternative and huge potential for enabling droplets to grow rapidly and to be transported towards the region of interest, i.e., shedding from the surface, in a quick and efficient manner with the consequent enhancements beneficial to many industrial and everyday life applications. In the next section, state-of-the-art works of fabricating SLIPSs and bioinspired gradient structures are reviewed.

## 3. Fabrications of bioinspired SLIPSs and gradient structured surfaces

### 3.1 Fabrication of bioinspired SLIPSs

The Nepenthes pitcher plant is considered as one of the best insect hunter in the natural plant world due to its slippery peristome surface as reported in the seminal work of Bohn and Federele[46]. Almost a decade later, the concept of SLIPSs was then proposed by Wong et al.[45] and further realized by infusing a lubricant or oil that remains locked in place within the hierarchical micro/nanostructures of a SHS. Excellent durability, small sliding angles and low contact angle hysteresis conferring extremely low adhesion were some of the initial enhanced capabilities reported on these novel SLIPSs[45, 101]. In addition, in recent years, SLIPSs have been found to display superior stability and self-healing performance, as well as repelling low surface tension liquids including oils, blood and hydrocarbons[102, 103].

In industrial applications, high thermal conductivity metals, such as copper are desired for the manufacturing of thermal management devices, namely thermosyphons, loop heat pipes, heat exchangers etc. Therefore, the scientific and engineering communities have developed a wide range of fabrication procedures for the manufacturing of SLIPSs on metal substrates. The fabrication SLIPSs is typically divided into three steps: first, micro-, nano- or hierarchal micro-/nanostructures are created; second, the hydrophobization of the surface via the deposition of a conformal hydrophobic low surface energy coating over the structures is then adopted; last, the lubricant is infused within the fluorinated structures, conferring the slippery properties to the surface[45, 104]. We note here, that in occasions, some of the fabrication steps may differ as per a different approach adopted. Details on the fabrication of different SLIPSs based on various metal and no metal substrates in the absence of a wettability gradient are described next within this subsection and summarized in Table 1.

Inspired from nature aiming to create low adhesion, robust, and self-healing surfaces Wong et al.[45] proposed the first engineered SLIPSs fabricated via molding method of epoxy resins further rendered hydrophobic by heptadecafluoro-1,1,2,2-tetrahydrodecyltrichlorosilane, and finally infused in Krytox oil (Krytox 100 and 103). Togasawa et al., created boehmite nanostructures on aluminum substrates after immersion in boiling or hot water for 10 min and further functionalized by silicon oil (100 cSt) grafting at 300 ℃ for 5 min. Finally, the same silicon oil was impregnated into the nanostructures to create the SLIPS. On these SLIPSs, the contact angle, sliding angle and contact angle hysteresis of the SLIPS were 96°, 3° and 2°, respectively, demonstrating the excellent low adhesion properties of SLIPSs[105]. SLIPSs manufactured from stainless steel and carbon steel were fabricated by Wang et al.[106]. The micro/nanostructures were formed through either immersing stainless steel or carbon steel

into ferric chloride acid at 40 ℃ for 1 h. The surfaces were further functionalized with 1*H*, 1*H*, 2*H*, 2*H*-perfluorodecyltriethoxysilane (FAS-17) self-assembled monolayer (SAM) via immersing it into silane solution (FAS-17-ethanol), where the silane molecules self-assemble to form a monolayer covalently attached to the structured surface. A perfluorinated oil was then impregnated into the surfaces to form the SLIPSs. Perfluorinated oil has more affinity to low surface tension silane locking the oil in between the micro/nanostructures[107]. These SLIPSs fabricated from stainless steel exhibited excellent sliding and thermal-healing properties. Copper has also been extensively employed to fabricate SLIPSs. Guo and Tang[108], Lee et al.[109] and Zhu et al.[110] fabricated nanostructured copper substrates through immersing the copper plate into an alkaline solution consisting of potassium persulfate and potassium hydroxide at 70 ℃ for 1 h, as shown in step A of **Fig. 3**(a). Then the surface was chemical functionalized after immersing the structure substrate into modified solution of n-octadecyl mercaptan at 70 ℃ for 1 h, as in step B of **Fig. 3**(a). Finally, droplets of Krytox GPL 100 were dispensed on the modified surface resulting in SLIPS with a homogeneous lubricant layer, as in step C of **Fig. 3**(a). Schematics of the fabrication process followed by Guo and Tang can be found in **Fig. 3**(a). From scanning electron microscopy (SEM) images in **Fig. 3**(b) the blade-like nanostructures were uniformly distributed on the copper surface. After impregnation, these SLIPSs provided the contact angle hysteresis as low as 5°.

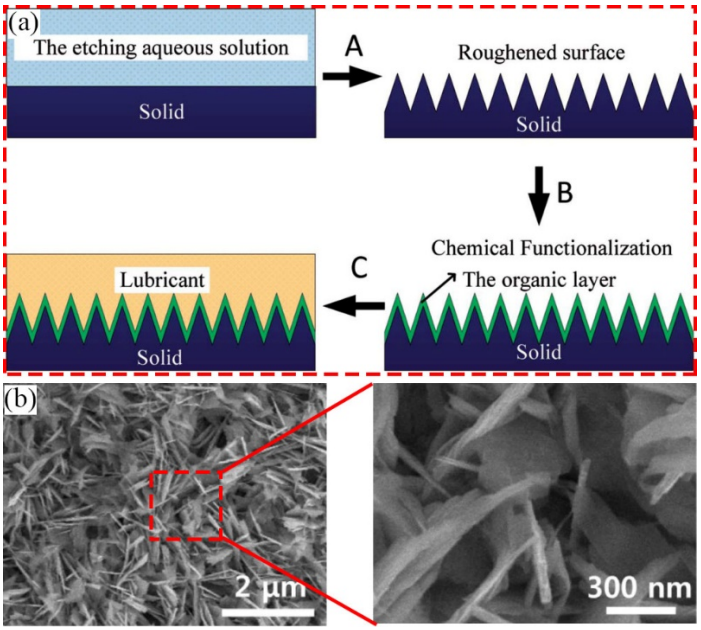


**Fig. 3. Fabrication of SLIPS on copper substrate. (a) manufacturing procedures of fabricating SLIPS. Step A, chemical etching treatment; step B, chemical modification; step C, lubricant impregnation; (b) SEM images of nanostructures formed on copper substrate[108]. Copyright 2018 Royal Society of Chemistry**

While most of the manufacturing processes were carried out for flat samples, Seo et al.[111] and Preston et al.[31, 112] realized SLIPS on a copper tube. Copper tube was immersed into a hot mixed alkaline

solution composed of sodium chlorite, sodium hydroxide and sodium phosphate tribasic dodecahydrate to render the knife-like nanostructures formed on the copper tube. The copper tube was further modified with trichloro(1*H*, 1*H*, 2*H*, 2*H*-perfluorooctyl)silane (TFTS) and infused with Krytox GPL 101. The heat transfer performance of the fabricated SLIPS tube was also studied and an enhancement was reported because of its excellent droplet shedding performance. SLIPSs made of silicon wafers with contact angle hysteresis as low as 1° were prepared by Solomon et al.[113]. Micro/nanostructures were created on silicon wafers via laser ablation process by and then coated with octadecyltrichlorosilance (OTS); finally the SLIPS was obtained after impregnation with silicon oil. Other researchers have also made use of silicon wafers for the fabrication of SLIPSs[42, 91, 114]. Microposts were prepared via photolithography and deep reaction ion etching (DRIE), while further etching in a plasma of $O_2$ and $SF_6$ was adopted to obtain the nanostructures. After the creation of the micro- and/or nano-structures, the surface was cleaned in a Piranha solution and then modified with OTS, rendering the silicon surface hydrophobic so as to allow the lubricant to be impregnated into the structures.

All reported SLIPSs fabricated through infusing the modified structured surface with lubricant, independently of the nature of the material underneath the coating, showed excellent non-adhesion properties such as: as small sliding angle, negligible contact angle hysteresis, self-healing, good durability, and so on. These merits indicate that the unique functionalities and enhanced capabilities of SLIPSs have the potential to enhance applications where low adhesion and enhance mobility of the liquid is paramount[115, 116]. However, the divergences about the particular characteristics and capabilities between different SLIPSs also exist, so a recapitulation on the current state-of-the-art SLIPSs is of much need. The particular characteristics of droplet-surface interactions on bioinspired SLIPS, wettability gradient and multi-gradient cooperation surfaces are then introduced in Section 4, bioinspired surfaces for condensation applications are summarized in Section 5, while the guidelines and perspective for further and future investigations are provided in in Section 6.

**Table 1. Summary of surface fabrication procedure in the absence of wettability gradients**

| References | Materials | Fabrication procedures | Surface/structures | Gradients | Description |
|---|---|---|---|---|---|
| Wong et al.[45] | Epoxy resin/Teflon | Replica molding method | Epoxy nanostructures/ Teflon nanofibers | ------ | Epoxy-resin nanostructured surfaces via replica molding, hydrophobized & infused with Krytox 101 or103 |
| Togasawa et al.[103] | Aluminum | Hydrothermal method | Boehmite nanostructures | ------ | Nanostructures were formed after immersion in boiling water then grafted with 100 cSt silicon oil and further infused with the same silicon oil |
| Wang et al.[106] | Stainless steel and carbon steel | Chemical etching | Micro/ nanostructures | ------ | Nanostructures were formed after immersion in ferric chloride acid solution followed by self-assembled monolayer coating and perfluorinated oil impregnation |
| Guo and Tang[108], Lee et al.[109] and Zhu et al.[110] | Copper plate | Chemical oxidation in alkaline solution (potassium persulfate and potassium hydroxide) | Nanostructures | ------ | Nanostructures were unctionalized with n-octadecyl mercaptan and further infused with Krytox GPL 100 as the lubricant |
| Seo et al.[111] and Preston et al.[31, 112] | Copper tube | Chemical oxidation in alkaline solution (sodium chlorite, sodium hydroxide and sodium phosphate tribasic dodecahydrate) | Nanostructures | ------ | Knife-like nanostructures were formed after immersion in an alkaline solution, TFTS was then used to functionalized the surface and Krytox GPL101 as the lubricant |
| Solomon et al.[113] | Silicon wafer | Laser ablation process | Micro/ nanostructures | ------ | Micro/nanostructures were then coated by OTS hydrophobic coating and silicon oil impregnation |
| Anand et al.[42], Smith et al.[91] and Dai et al.[114] | Silicon wafer | Photolithography and deep reaction ion etching in $O_2$ and $SF_6$ plasma | Microposts | ------ | Microposts were then cleaned in a Piranha solution and functionalized with OTS before impregnation with silicon or Krytox oil |

### 3.2 Fabrication of bioinspired gradient structures

Shedding of micrometer and millimeter sized droplets from the surface without external energy input or forces applied is critical to microfluidics and to condensation applications, amongst others. However, the effective and efficient manipulation of such small sized droplets remains a great challenge as hysteresis forces opposing to the droplet motion become increasingly important with the decrease of the droplet size/diameter[117]. Aiming to overcome this challenge, researchers have recently focused on exploiting different droplet transport and manipulation strategies inspired by natural plants and insects[48, 118, 119] such as: cactus spines[120], the Namib desert beetle[38, 121], spider silk[122] and so on, which enhances droplet mobility via surface wettability gradient and/or Laplace pressure gradients as the driving force[123-125]. Hence, it is crucial to finely design and fabricate unique surface structures that empower wettability gradients and Laplace pressure gradients to precisely control the droplet motion. Below we summaries recent strategies proposed by different researchers and groups aiming to create effective surface structures exploiting wettability gradients and Laplace pressure induced motion, which are further summarized in Table 2.

#### 3.2.1 Structures with surface wettability gradient

Droplet transport can be realized via chemical and/or structural wettability gradients, on which typically the droplet moves spontaneously towards the more wettable region. Copper wires introducing a structural wettability gradient were prepared by Xing et al.[126] through gradient anodic oxidation method as shown in **Fig. 4**(a-I). The copper wire was anodically oxidized with sodium hydrate electrolyte solution, and the oxidation extent at different positions of the copper wire could be controlled by varying the electric current and the oxidation time. The morphologies of the anodically oxidized surface shown in SEM in **Fig. 4**(a-II) exhibited grater size and density of the structures near the electrode (bottom in **Fig. 4**(a-I)) and smoother far away from the electrode (top in **Fig. 4**(a-I)). In addition, a chemical gradient was also imposed on the copper wire from top to bottom as Cu and $Cu^{+}$ were gradually further oxidized to form $Cu^{2+}$ where $Cu^{2+}$ finish typically exhibits more hydrophilicity[127]. The cooperation and synergy between rough structures and chemical composition gradient modified further the surface wettability providing a wide range of contact angles from 70° to ca. 5° as shown in **Fig. 4**(a-IV).

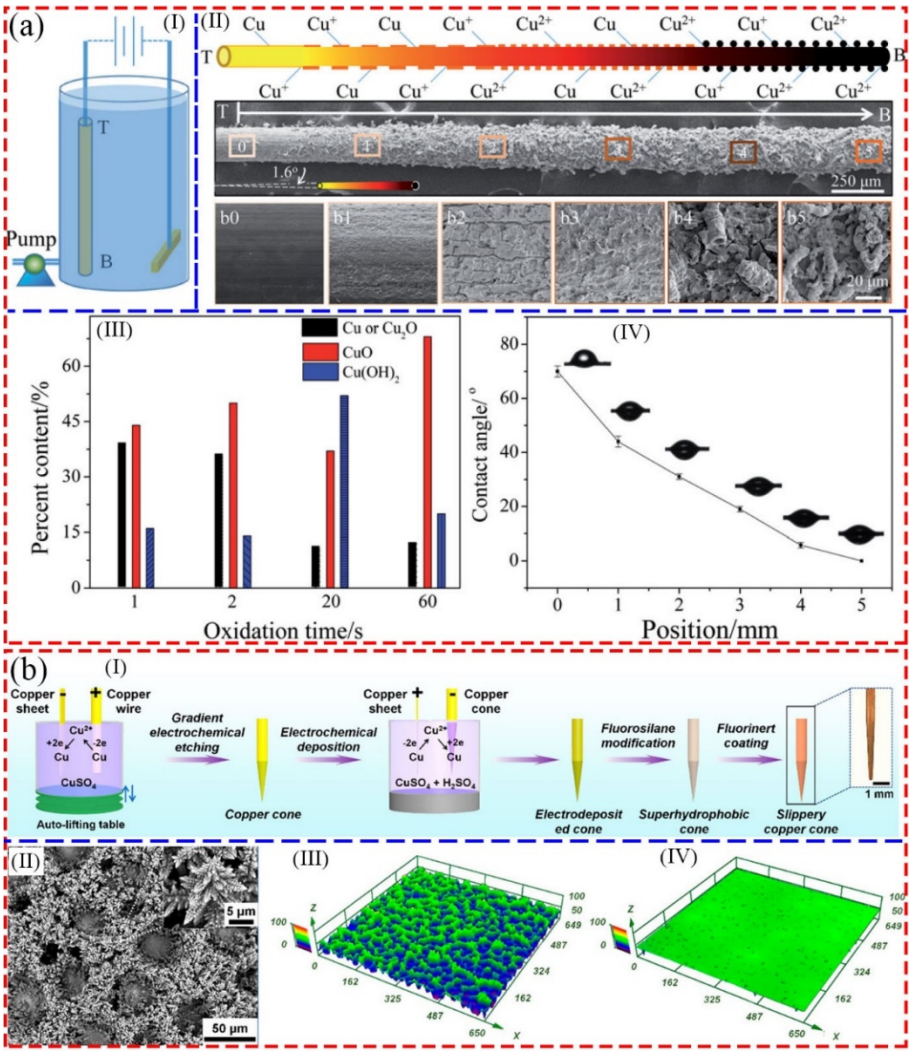


**Fig. 4. Schematic illustration of fabrication procedures of wettability gradient on copper wire and slippery conical copper spines with relevant characterizations. (a-I) setup for gradient anodic oxidation; (a-II) microstructure formation and SEM images of copper surface; (a-III) chemical composition of copper surface at different anodic oxidation time; (a-IV) contact angle variation versus position[126]. Copyright 2017 Royal Society of Chemistry. (b-I) The procedures of fabricating slippery copper spines; (b-II) SEM image of electrodeposited conical copper spines; (b-III) and (b-IV) were the confocal laser scanning microscope images of electrodeposited conical copper spines before and after impregnation of lubricant respectively[128]. Copyright 2019 American Chemical Society.**

Surface wettability gradient was also realized both on a graphite plate and a gradient disc by Feng et al.[129, 130] through a similar anodic oxidation method. On the graphite plate surface, the contact angles along the direction of the imposed mainly chemical wettability gradient changed gradually from 115° to 34°, i.e., a wettability gradient of 3.38°/mm. On the graphite disc plate, a radial chemical wettability gradient is created with the wettable direction from center to periphery. The wettability patterned gradient surface was prepared by Ghosh et al.[131] and Wu et al.[132] through developing a different patterned wettability surface fabrication by spin-coating a mixture solution consisting of trimethoxyoctadecylsilane (TMOS), titanium dioxide and ethanol onto a glass slide and further drying

in an oven at 100 ℃ for 1 h to form the SHS. Polyethylene terephthalate (PET) photomask with black strips was then applied onto the SHS, and then the ultraviolet (UV) light exposure was conducted on the SHS covered with the PET photomask for 30 min. Areas exposed to the UV light turn into superhydrophilic patterns. Chemically patterned wettability gradient copper plates were obtained by Xing et al.[133] through electrochemical technique. Here, the copper substrate was covered with a porous mask and then immersed into the electrolyte solution. Only the surface area exposed to the electrolyte solution was oxidized during the anodic oxidation process. The surface wettability gradient is then obtained as a consequence of the different current density and oxidation time gradient by emptying the electrolyte solution. This provided contact angles along the length direction ranging from 113.2° to 36.4° with a surface wettability gradient of 3.07°/mm.

### 3.2.2 Conical structures with Laplace pressure gradient

A different approach of inducing the manipulation and motion of a droplet is that inspired by the efficient droplet collection of cactus spines, where a Laplace pressure gradient generated by the surface curvature, such as a conical surface, which plays a major active role in droplet transport[88, 134, 135]. Conical copper spines were proposed by Ju et al.[89] through applying gradient electrochemical etching method. As a consequence of the different immersion depth/time, conical copper spines with apex angles ranging from 9° to 15° were achieved. Copper wires were further utilized to produce slippery copper spines by Xu et al.[136] and Xiao et al.[128] through electrochemical etching, electrochemical deposition, fluorosilane modification and fluorine infusion as shown in **Fig. 4**(b-I). After electrochemical etching, electrochemical deposition was conducted to reduce and deposit the copper ions on the conical surface forming micrometer pores and well-ordered dendritic branches as shown in **Fig. 4**(b-II) and (b-III). Electrodeposited conical copper spines were modified with TFTS and then FC-3283 lubricant was infused into the structures to form slippery copper spines. The roughness of the slippery copper spine was greatly reduced, see corresponding confocal laser scanning microscopy in **Fig. 4**(b-IV). More recently, hydrophobic and superhydrophilic conical copper spines fabricated via electrochemical etching method and surface modification were proposed by Yu et al.[137]. Copper spines with conical morphologies were formed after electrochemical etching and immersion into the alkaline solution including sodium hydroxide and ammonium persulfate to fabricate the superhydrophilic conical copper spine; while the hydrophobic conical copper spines were prepared after further modification with 11-mercapto-1-undecanol.

Cactus spine-like magnetic arrays were prepared using polydimethylsiloxane (PDMS) prepolymer

and cobalt magnetic particles through mechanical punching and template dissolving methods[138]. The ordered conical holes were poked on the polyvinyl chloride (PVC) polymer sheet with needles, which was used as template. The cobalt magnetic particles were dispersed into the holes, and then the PDMS prepolymer covered the template. Finally, the cactus spine-like magnetic arrays were obtained after the PVC template dissolved into the tetrahydrofuran solution. A different process using magnetic particles to fabricate micropillar arrays with liquid repellent properties were prepared via magnetic particle-assisted molding process by Huang et al.[139]. The Laplace pressure difference induced by the conical micropillars is beneficial for the droplet transport from the tip to the base of the spine-like micropillars. In addition, a membrane integrating conical spines with micro/nanostructures was prepared by Zhou et al.[140]. On one hand, aluminum wires were vertically immersed into a silver chloride electrolyte solution, and then placed in a different solution consisting of magnesium sulfate and ammonia water to form the superhydrophilic conical spines. On the other hand, a PET membrane was further functionalized to form hydrophilic grooves for collecting water while the other side was coated with a hydrophobic silane. The patterned wettability PET membrane was then impaled by the superhydrophilic conical spines (and hydrophilic needles) for the fabrication of this unique functionalized membrane. A needle array surface inspired by the hierarchical structure and unique wettability of the beetle morphology was fabricated by Wen et al.[141]. Carboxybetaine needles were exposed under UV light to form hydroxyl groups on the surface, while a sheet used as background was coated with a hydrophobic coating. Subsequently, the hydrophobic sheet was impaled by the hydrophilic needles, and finally the combination of hydrophobic sheet and hydrophilic structures significantly enhanced its fog harvesting capabilities.

### 3.2.3 Combination of special structures

Since water droplet transport plays a crucial role for enhancing condensation heat transfer performance, it is necessary to fabricate unique structures for facilitating and accelerating droplet transport. Mirror polished aluminum plates were used to fabricate alternating wettability patterned surfaces for DWC by Ghosh et al.[142]. A polymer layer covering the top side of the aluminum plates was cut using $CO_2$ laser and then peeled off. The aluminum plate was subsequently immersed into hydrochloric acid and boiling water to form superhydrophilic nanostructures on the unmasked region, while the remaining protective polymer layer was peeled off to expose the mirror polished aluminum surface, which exhibited hydrophilic wettability. Schematics of the obtained superhydrophilic and hydrophilic patterned wettability aluminum plate is shown in **Fig. 5**(a).

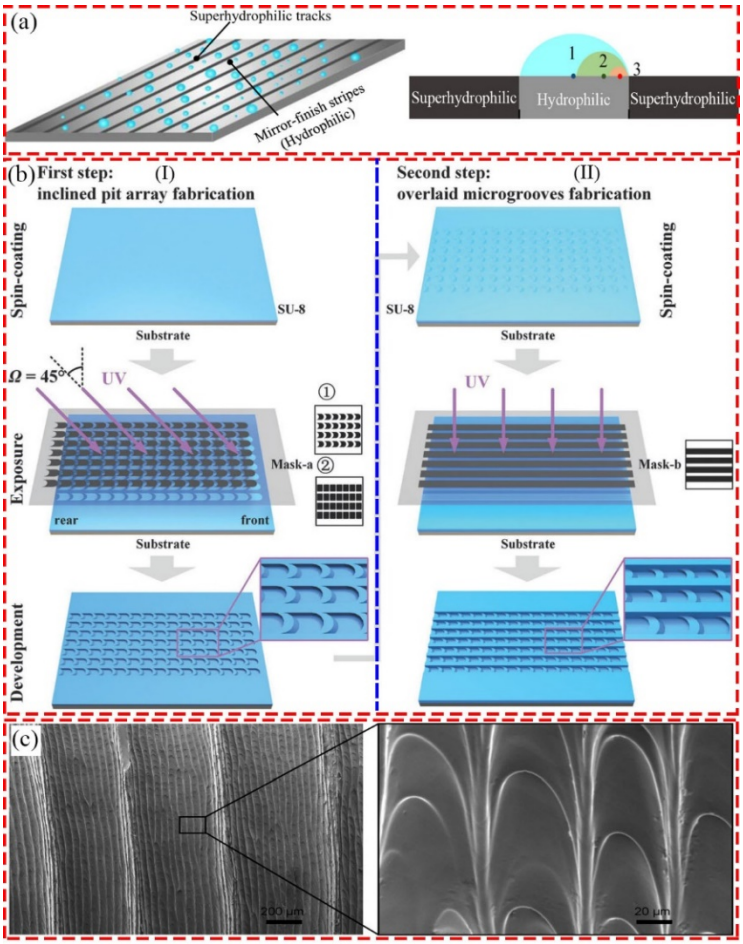


**Fig. 5. Procedures of fabricating alternative superhydrophilic and hydrophilic patterned surfaces and inclined pitted groove structures. (a) fabrication alternative superhydrophilic and hydrophilic patterned surface[142]. Copyright 2014 American Chemical Society; (b-I) the first step is inclined pit array fabrication of pitted groove structures; (b-II) the second step is overlaid microgrooves fabrication[143]; Copyright 2017 Wiley-VCH; (c) SME images of artificial peristome based on Nepenthes pitcher plants, and the artificial peristome had microgrooves and duck-billed cavities[144]. Copyright 2016 Nature Research.**

Unique arc-shaped structures with open sharp edges and microgrooves were developed by Chen et al.[143] through two steps of UV lithography as shown in **Fig. 5**(b-I) and (b-II). First, the glass substrate was spin coated with a SU-8 photoresist, the masks with arc and square patterns were placed covering the photoresist and morphologies with arc and squared pit arrays were obtained after UV lithography as shown in **Fig. 5**(b-I). The second step involved the use of mask with straight stripes placed on top of the SU-8 photoresist, which was spin coated again on the pit array, and then UV lithography was conducted perpendicularly to the mask as shown in **Fig. 5**(b-II). Finally, the arc and squared pitted grooves were obtained. On other hand, inspired by the excellent droplet transport capabilities of peristome surface of Nepenthes pitcher plants[145, 146], artificial peristomes were fabricated by Chen et al.[144] through replica molding method, where the PDMS prepolymer was applied over the peristome surface to form a negative replica and then $CF_4$ plasma was conducted on the negative replica to generate an anti-sticky layer. Finally, to obtain the positive replica resembling the surface structure of

the artificial peristome, further replication using the same PDMS prepolymer was applied onto the negative replica, left it to cure and demolded. Peristome replicas had hierarchical microgrooves with one large microgroove containing approximately ten small parallel microgrooves which had duck-billed cavities as shown in **Fig. 5**(c). The replica was treated by oxygen plasma to make it superhydrophilic, which could enhance the water transport capabilities. More recently, the peristome of the Nepenthes alata was further replicated via low frequency elliptical vibration cutting providing samples with worse structural resolution[147].

### 3.2.4 Structures with multi-gradient cooperation

Small-sized droplet becomes more and more stationary as adhesion forces increases when decreasing the droplet size. Therefore, structures with multi-gradient cooperation play a crucial role for overcoming hysteresis forces. Inspired by the superior droplet transport capabilities of the spider silk, artificial fibers were proposed by Zheng et al.[98], Tian et al.[148] and Xue et al.[149], which exhibited unique droplet collection and transport capabilities. In their work, uniform nylon fiber was immersed into a poly (methyl methacrylate) (PMMA) solution containing an appropriate concentration of *N*,*N*-dimethyl formamide (DMF), and then the nylon fiber was quickly extracted from the polymer solution. The polymer solution film on the fiber broke up and simultaneously accumulated to form a series of small droplets due to the Rayleigh instability[150], and finally the artificial spider silk with spindle-knots and joints was obtained after the droplets dried. The complete steps followed for the fabrication of artificial spider silk with spindle-knots are provided as schematics in **Fig. 6**.

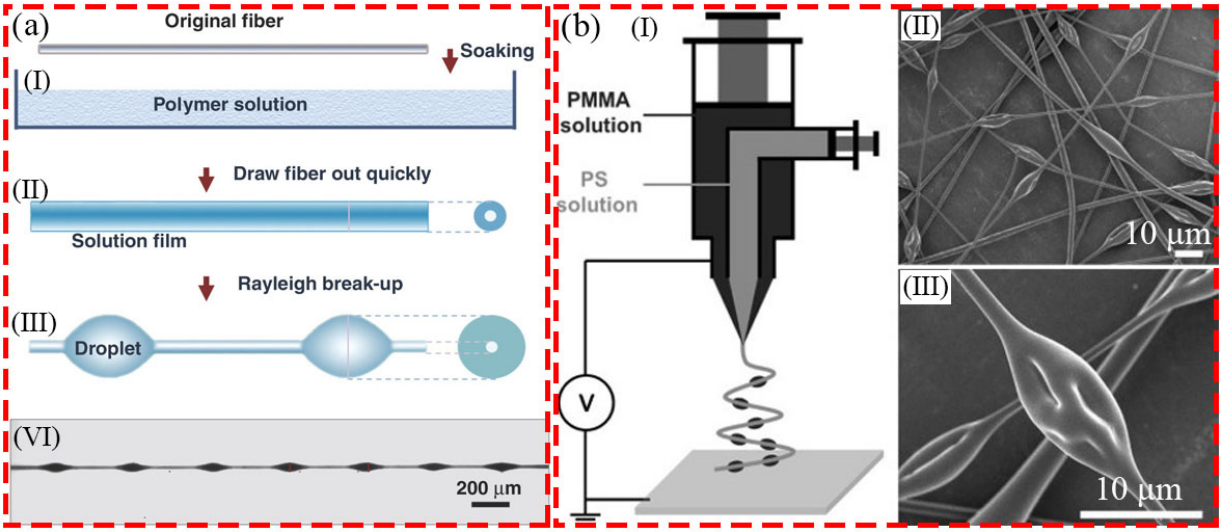


**Fig. 6. Procedures of fabricating artificial spider silk. (a-I) the nylon fiber was immersed into the PMMA solution in DMF; (a-II) thin polymer film coated on the fiber; (a-III) polymer film broke up into a series of droplets; (a-VI) the artificial fiber with spindle-knots was prepared[148]. Copyright 2011 Wiley-VCH. (b-I) coaxial electrospinning setup; (b-II) and (b-III) SEM images of artificial fibber with spindle-knots[151]. Copyright 2012 Wiley-VCH.**

On other hand, electrospun spindle-knots microfibers were prepared by Dong et al.[151]. In their work, polystyrene (PS) solution and poly(methyl methacrylate) (PMMA) solution flow rates were precisely controlled during electrospinning as shown in **Fig. 6**(b-I). The PS solution flowed out to form the microfiber while the PMMA solution to form created the spindle-knots as shown in **Fig. 6**(b-II) and (b-III). Artificial fibers similar to spider silk were prepared by Thakur et al.[152] through electrospinning method, where polyvinylidene fluoride (PVDF) and poly(*N*-isopropylacrylamide) (PNIPAM) solution were used as fiber and spindle-knots solutions. Thereafter, the fiber with spindle-knots was dried in an oven at 150 ℃ for 8 h to promote the cross-linking between the PVDF fiber and PNIPAM spindle-knots. Further, a three dimensional (3D) fiber network with nanocone structures was fabricated by Li et al.[153], where plasma etching was conducted on nylon fiber network, and then immersed into a hydrogen peroxide solution. The pretreated fiber network was thereafter submerged into a colloidal solution and then dried at 65 ℃. Afterwards, the hydrothermal reaction of the fibril network was conducted in a solution consisting of zinc nitrate hexahydrate and hexamethyleneteramine at 95 ℃ for 4 h. Finally, the nanocone-decorated three dimensional fiber network was obtained after the rinsing with plenty of deionized water.

Inspired by the merits of cactus spines and Sarracenia trichomes pitcher plant, a novel configuration was proposed based on the principles derived from the high efficient fog harvesting of cactus spines and the rapid water and preys transport of the Sarracenia trichomes[97], as shown in **Fig. 7**(a). The novel configuration comprised a spine with barbs and hierarchical channels (SBHCs). The different size channels of the SBHCs were firstly carved on the copper sheet via direct laser structuring (Fig. 7(b)) while oriented microbarbs were cut by laser scanning (**Fig. 7**(c)). The SBHC was then immersed into a hot mixed alkaline solution to render the lamellas-like nanostructures formed on the SBHC, which resulted in the water contact angle dropping from 42˚ to 0˚, as shown in **Fig. 7**(d). The spine and microbarbs of SBHCs were wedge shaped with an apex angle of 6˚ and 11˚, respectively. The superhydrophilic hierarchical microchannels which were constructed by the high and low ribs could form a liquid film during condensation to achieve rapid water transport due to the integrated driving force arising from surface wettability and wicking action, and from Laplace pressure gradient of the hierarchical microchannels. More recently, a bioinspired superwettable microspine chip was prepared by Chen et al.[154]. A candle soot layer was prepared on a glass slide substrate, and the silica shell was subsequently deposited on the candle soot layer through chemical vapor deposition. The nanosilica glass slide substrate was treated with oxygen plasma, and then immersed into a modified solution composed of OTS to render it superhydrophobic. The UV-irradiation was conducted on the

superhydrophobic substrate through a photomask to form superhydrophilic spine-like micropatterns. Finally, the superwettable microspine chips with superhydrophilic asymmetrical geometric shapes were constructed on the superhydrophobic background, where the capability of rapid droplet transport can be realized due to the directional force arising from the Laplace pressure gradient of the asymmetrical geometric microspine coupled to the superhydrophilicity of the microspine. A wax-infused cactus kirigami with anisotropic shape was also fabricated by Bai et al.[155]. The filter paper was cut into a kirigami spine using a $CO_2$ laser device, and then it was immersed into the melting paraffin to form a cactus kirigami, which can realize the capture of fog droplets and periodic refreshing of collecting interface through droplet transport.

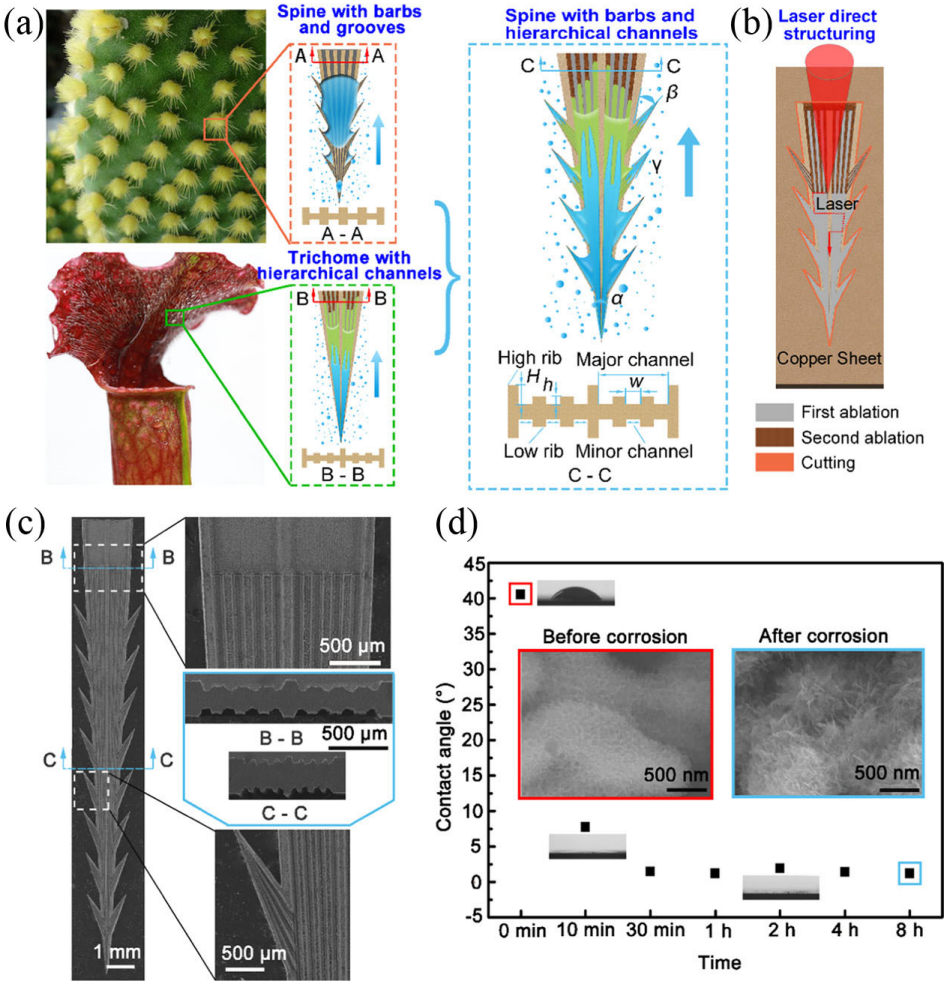


**Fig. 7. A novel configuration composed of microbarbs and hierarchical microchannels for condensate ultrafast transport. (a) The spine with barbs and hierarchical channels (SBHC) integrated the merits of cactus spines and Sarracenia trichomes; (b) the fabrication process of SBHC using laser direct structuring method; (c) SEM images of the SBHC; (d) the surface morphologies and contact angles of SBHC before and after chemical treatment[97]. Copyright 2020 American Chemical Society.**

### 3.3 Fabrication of SLIPS comprising bioinspired wettability gradients

Inspired by the remarkable droplet collection capabilities of the Namib desert beetle, an aluminum sheet was used to fabricate SLIPS with bumpy structures by Park et al.[99]. The bumpy surface was

prepared by pressing the aluminum sheet between printed polymer molds, and then immersed into boiling water to form boehmite nanostructures. The nanostructure fabrication process adopted by Park et al. was similar to SLIPS fabrication in the absence of micro-bumps[105]. Finally, SLIPSs with various bumpy structures were obtained after structural and chemical surface modification and further impregnation with carnation mineral oil. The spontaneous and remarkable shedding performance of these surfaces comprising controlled micro- and/or millimeter sized bumps when compared to the control sample was highlighted, which in turn should offer excellent heat transfer performance. Thereafter, a V-shaped grooved SLIPS was designed by Kajiya et al.[156], where $TiO_2$ nanoparticle paste was coated on a silicon substrate and then imprinted with a PDMS mold which consisted of micro-prism pattern. Subsequently the patterned $TiO_2$ paste was sintered at 500 ℃ to prepare a reliable micro-prism pattern on the silicon substrate, and finally the V-shaped grooved SLIPS was achieved after the modification with trichlorosilane and impregnation with silicone oil.

The excellent water transport capabilities of the leaf vein bio-inspired Lin et al.[157], Liang et al.[158] and Liu et al.[159] to create a patterned surface with hierarchical wedge-shaped superhydrophilic tracks on a hydrophobic background. The photoresist was coated on a PET substrate and then developed by immersing it into the RD-6 developer after exposure to UV light through a photomask. Subsequently a copper layer was sputtered on the surface with the assistance of magnetron sputtering system. The copper patterned tracks on the PET surface were obtained after dissolving the photoresist by immersion in acetone solution. Finally, the patterned surface with superhydrophilic tracks on hydrophobic background was prepared after immersing it into the alkaline solution composed of sodium hydroxide and ammonium persulfate.

An asymmetric slippery surface with shape-gradient morphology was fabricated by Zhang et al.[61] through $CO_2$-laser cutting of PMMA, hydrophobic modification via $SiO_2$ NPs and impregnation with FC-3283 lubricant.. The driving force arising from the shape-gradient structure of the slippery PMMA sheet is beneficial for transport of droplet and gas bubble in aqueous environment. An anisotropic SLIPS with periodic microgrooves was also prepared by Lv et al.[160] through one-step femtosecond laser scanning on PDMS further coated with a layer of silicone oil via spin coating. A SLIPS with multiscale grooved structures was fabricated by Jiao et al.[161]. The multiscale grooves on aluminum substrate were achieved using femtosecond laser direct writing technology further functionalized by the silane hydrophobic agent (Glaco) to make it superhydrophobic and impregnated with FC-3283, silicone oil and Krytox 101 lubricants. Further, a windmill integrated PDMS anisotropic grooved surface (AGS) was produced by Wang et al.[162] able to harvest water in complex windy environments.

In their work, nylon was used as the construction material to prepare the template which had microscale wedge-shaped grooves, while a PDMS anisotropic grooved surface was fabricated after spinning the PDMS prepolymer on the template. The superhydrophobic AGS was produced by immersing in hydrophobic fumed silica, and then immersed into hydroxy-terminated PDMS solution to produce a hydrophilic lubricant-infused slippery (HLIS) AGS.

The surface physicochemical properties coupled with structural gradients has been found to play a crucial role for droplet manipulation, transport and control with the consequent enhancement on condensation phase-change amongst others. Aiming to improve droplet mobility and dropwise condensation self-removal, this review focuses on the synergistic effects of the low adhesion of bioinspired SLIPS coupled to structural surfaces comprising surface wettability gradients either chemical or structural or both. The wide range of fabrication procedures for surface and/or structures introduced above have been clearly summarized and are listed within Table 1 and Table 2. The next section, focuses on state-of-the-art works on a more applied nature of SLIPSs and bioinspired gradient structures specific to condensation heat transfer applications. Emphasis is paid to introduce the fabrication and characterization of the surfaces, i.e., the surface physicochemical properties and structural gradients, and to report the enhancements in droplet mobility and/or to condensation performance.

**Table 2. Summary of wettability gradient and SLIPS surface fabrication procedure**

| References | Materials | Fabrication procedures | Surface/structures | Gradients | Description |
|---|---|---|---|---|---|
| Xing et al.[126] | Copper wires | Gradient anodic oxidation method | Rough structures | Structural and chemical gradients | Wettability gradient could be controlled from 35°/mm to 4°/mm |
| Feng et al.[129] | Graphite plate | Anodic oxidation method | Rough structures | Chemical wettability gradient | Wettability gradient of 3.38°/mm |
| Ghosh et al.[131] and Wu et al.[132] | Glass substrate | Spin-coating method | Patterned surface | Wettability-patterned gradient | Wettability changes from hydrophobic to hydrophilic |
| Xing et al.[133] | Copper plates | Electrochemical technique | Patterned structures | Wettability-patterned gradient | Surface wettability gradient of 3.07°/mm |
| Ju et al.[89] | Copper spines | Gradient electrochemical etching method | Conical spines | Conical Laplace pressure gradient | The conical structure facilitates droplet transport |
| Xu et al.[136] and Xiao et al.[128] | Copper wires | Electrochemical etching and deposition, surface modification | Micrometer pores and well-ordered dendritic branches formed on conical surface | Conical Laplace pressure gradient | Slippery copper spines were formed after infusing lubricant |
| Yu et al.[137] | Copper spines | Electrochemical etching method | Conical morphologies were formed on a copper spine | Conical Laplace pressure gradient | Hydrophobic/superhydrophilic conical copper spines |
| Peng et al.[138] | PDMS and cobalt magnetic particles | Mechanical punching and template dissolving methods | Cactus spine-like magnetic arrays | Conical Laplace pressure gradient | The magnetic responses of the cactus-inspired array under an external magnetic |
| Huang et al.[139] | PDMS and carbonyl iron microparticles | Magnetic particle-assisted molding process | Micropillar arrays | Conical Laplace pressure gradient | The slippery micropillar arrays were formed after infusing fluorinated oil |
| Zhou et al.[140] | Aluminum wires and PET membrane | Integrative electrochemical corrosion and hydrothermal method | The rough micro/nanostructures formed on a conical spine | Wettability and Laplace pressure gradients | The combination of superhydrophilic spine and the PET membrane with opposite wettability on its two sides. |
| Wen et al.[141] | Nickel needle & hydrophobic sheet | UV plasma | Needle arrays | Hydrophilic needles impaling the hydrophobic sheet | The hydrophilic needles impaled into the hydrophobic sheet |
| Ghosh et al.[142] | Aluminum plates | Etching and hydrothermal method | Alternative wettability patterned surfaces | Patterned surfaces | The patterned surface combined hydrophilic mirror polished stripe and superhydrophilic stripe |

| References | Materials | Fabrication procedures | Surface/structures | Gradients | Description |
|---|---|---|---|---|---|
| Chen et al.[143] | SU-8 photoresist | Spin-coating and UV lithography | Unique arc-shaped with open sharp edges and microgrooved structures | Arc and squared pit arrayed surface | The SU-8 photoresist coated on glass slide and UV lithography was conducted to the mask to form arc-shaped stripes |
| Chen et al.[144] | PDMS polymer | Replica molding method | Large microgroove with 10 small parallel grooves which had duck-billed cavities | Patterned gradient | Oxygen plasma to make it superhydrophilic and enhancing water transport capabilities |
| Zheng et al.[98], Tian et al.[148] & Xue et al.[149] | Nylon fiber | Rayleigh instability method | The hump geometry was formed on nylon fibers | The multi-gradient synergy was formed on the spindle-knots and joints | The nylon fiber was quickly extracted from the polymer solution to form a series of hump geometry. |
| Dong et al.[151] | PS and PMMA | Electrospinning method | Spindle-knots microfibers | The multi-gradient synergy was formed on the spindle-knots and joints | The PMMA solution adhered to the surface of PS microfiber to form the spindle-knots |
| Thakur et al.[152] | PVDF and PNIPAM | Electrospinning method | The PNIPAM spindle-knots formed on PVDF fibers | The multi-gradient synergy was formed on the spindle-knots and joints | The artificial fiber with spindle-knots was formed after drying in oven |
| Li et al.[153] | Nylon fiber network | Plasma etching and hydrothermal reaction | The nanocone structures was formed on a fiber network | The multi-gradient synergy was formed on the three dimensional fiber network | The nanocone-decorated three dimensional fiber network was obtained after the hydrothermal treatment |
| Wang et al.[97] | Copper sheet | Laser direct structuring and chemical oxidation | Hierarchical channels and microbarbs | Structural gradient | Hierarchical channels and microbarbs created by laser device and chemical oxidation |
| Park et al.[99] | Aluminum sheet | Mechanism and hydrothermal method | Bumpy structures with boehmite nanostructures | Laplace pressure gradients | The carnation mineral oil was infused into the bumpy structures to form slippery structures |
| Kajiya et al.[156] | Silicon substrate | Laser direct structuring and chemical oxidation | Micro-prism pattern | Structural gradient | V-shaped grooved SLIPS achieved after modification with trichlorosilane and silicone oil |
| Lin et al.[157] and Liu et al.[159] | PET substrate | Spin-coating and UV lithography | Hierarchical wedge-shaped track pattern | Structural gradient | Hierarchical wedge-shaped superhydrophilic tracks on hydrophobic background |
| Lv et al.[160] and Jiao et al.[161] | PDMS and aluminum | Femtosecond laser direct writing technology | Multiscale grooves | Structural gradient | Multiscale grooved SLIPS was obtained after impregnation lubricant |
| Wang et al.[162] | PDMS substrate | Template model method | Wedge-shaped grooved pattern | Structural gradient | Hydrophilic lubricant-infused slippery anisotropic grooved surface was prepared after immersion with lubricant |

## 4. Particular characteristics of condensation on SLIPSs and bioinspired gradient structures

### 4.1 Droplet condensation characteristics on SLIPSs

Condensation is a ubiquitous phase change heat transfer process of important relevance to many industrial and daily life applications. We remind the reader here on the different condensation behavior, dynamics, droplet size distribution, condensation patterns and/or droplet shedding dynamics ensuing on SLIPSs when compared to high energy metal surfaces, smooth low energy hydrophobic ones and structured low energy SHSs. FWC is the common condensation mechanism taking place on high energy metal surfaces, while DWC occurs on hydrophobic, SHS and SLIPS[9, 12, 20, 163]. Briefly, SLIPSs provide virtually no pinning and the shedding of smaller sized droplets in the submillimeter range when compared to millimeter sized droplets on smooth hydrophobic surfaces[91, 94]. In addition, SLIPSs overcome shortcomings such as the high adhesion Wenzel state, or enhanced droplet pinning on structured SHSs occurring as a consequence of high subcooling conditions amongst others[27, 30, 164]. Below we summarize recent methodologies and advances on SLIPSs aiming to promote droplet mobility and transport during condensation phase-change.

#### 4.1.1 Condensation on uniformly structured SLIPSs

Dropwise condensation patterns on SLIPSs depends on whether the spreading coefficient of lubricant is positive or negative and eventually plays a crucial role in droplet condensation, growth, coalescence and transport. See section 2.2 for more details on the fundamentals of droplet wetting on SLIPSs and on the spreading coefficient. Anand et al. investigated the influence of lubricant type on water droplet condensation through Environmental Scanning Electron Microscopy (ESEM)[42]. As introduced in Section 2.2, low surface energy lubricants such as Krytox oil yield a positive spreading coefficient with the consequent occurrence of cloaking; while in the presence a high surface energy such as ionic liquids, a negative spreading coefficient and absence of cloaking is expected. The experimental results revealed that the condensed droplet patterns on both Krytox impregnated SLIPS and ionic liquid impregnated SLIPS were substantially different. It can be seen from **Fig. 8**(a) and (c) that the droplet nucleation, growth and coalescence dynamics were significantly inhibited on Krytox impregnated SLIPS compared to ionic liquid impregnated SLIPS, which was attributed mainly to the lubricant film cloaking the droplet as expected from the positive spreading coefficient of Krytox oil, which is represented in **Fig. 8**(b). Further quantification on the surface coverage fraction of condensed droplets on ionic liquid impregnated SLIPS represented in **Fig. 8**(h) demonstrated the higher condensation dynamics when compared to Krytox oil impregnated SLIPS. Of interest is the droplet

nucleation density reported in **Fig. 8**(i), which is at least one order of magnitude greater at earlier condensation times for ionic liquid impregnated SLIPS and then decreases due to dynamic coalescence, while the droplet nucleation density on Krytox oil impregnated SLIPS increases weakly. This work additionally report on the mobility of droplets on infused one-tier microposts and infused two-tier microposts. On one hand, in the absence of a nano-tier roughness as in **Fig. 8**(e), droplets are likely to be pinned to the microposts of SLIPS with the consequent suppressed mobility. On the other hand, the nanostructures decorating the microposts of SLIPS could significantly enhance the droplet mobility by reducing the contact surface fraction of droplet to the microposts' tops[91] as shown in **Fig. 8**(f). The high mobility of submillimeter droplets shedding and sweeping from the SLIPS is shown in **Fig. 8**(g), which assists on maintaining a small droplet area fraction, opposed to SHSs were the droplet area fraction increases and droplets as big as 3.5 millimeters were required for condensate shedding to ensue.

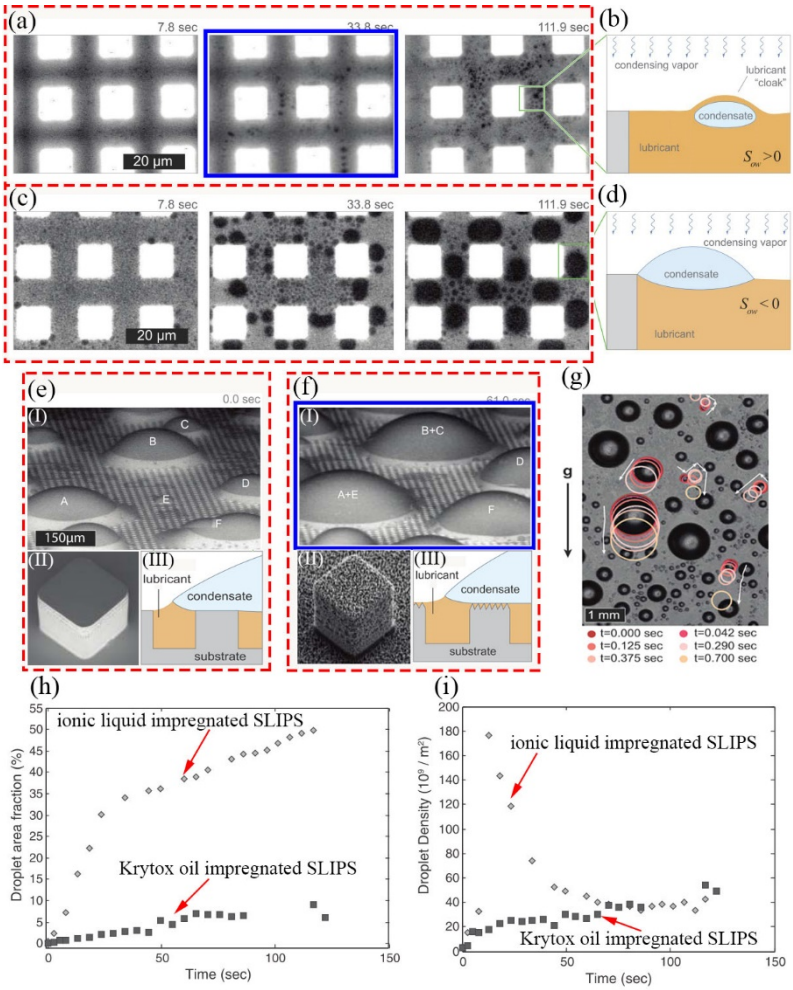


**Fig. 8. The influence of lubricant nature on droplet condensation: droplet cloaking versus non-cloaking. (a) ESEM sequence images of droplet condensation on SLIPS impregnated with Krytox oil which has positive spreading coefficient; (b) schematic illustration of the cloaking oil film over the condensed droplet; (c) ESEM sequence images of droplet condensation on SLIPS impregnated with ionic liquid which has negative spreading coefficient; (d) schematic illustration of non-cloaked droplet on SLIPS impregnated with ionic liquid; (e-I) ESEM of droplet**

**condensation on ionic liquid impregnated SLIPS with smooth microposts; (e-II) SEM of single smooth microposts; (e-III) schematic of droplet on SLIPS with smooth microposts; (f-I) ESEM droplet condensation on ionic liquid impregnated SLIPS with hierarchical posts; (f-II) SEM single microposts with nanostructures; (f-III) schematic of droplet on SLIPS with nanostructured microposts; (g) condensation snapshot of microposts with nanostructures impregnated with ionic liquid depicting the dynamic droplet position and motion. Quantification of the (h) surface area fraction covered by the condensed droplets versus time and (i) droplet nucleation density versus time on SLIPSs with Krytox oil and ionic liquid[42]. Copyright 2012 American Chemical Society.**

Depending on the nature of the lubricant, different droplet morphologies were achieved on the very same nanostructured and functionalized textured surface as studied by Dai et al.[114]. On a hydroxyl-terminated PDMS lubricant infused nanotextured surface, droplets adopted contact angles of approximately 76°, henceforth referred to as hydrophilic SLIPSs, while on those infused with Krytox 101 contact angles of 121° were reported, henceforth referred to as hydrophobic SLIPS. The vapor condensation on hydrophobic and hydrophilic SLIPSs was studied by where the droplets with contact angles of 121.5° and 76.2° were formed on hydrophobic and hydrophilic SLIPSs, respectively, which is shown in **Fig. 9**(a) and (b). When looking into the vapor condensation on hydrophobic SLIPSs when compared to hydrophilic SLIPS included in **Fig. 9**(a-II), (a-III) and (a-IV) and **Fig. 9**(b-II), (b-III) and (b-IV), respectively, important differences on the droplet number density and on the coalescence dynamics are highlighted such as the low-density nucleation and slower dynamics of coalescence in the case of hydrophobic SLIPSs when compared to hydrophilic ones. On hydrophilic SLIPSs, up to 268% higher nucleation density was reported when compared to hydrophobic SLIPSs, which is quantified in **Fig. 9**(c) and evidenced from the snapshots in **Fig. 9**(a) and **Fig. 9**(b) when comparing areas of snapshots before and after a droplet coalescence event occurs. Further, the larger contact area and lower droplet thickness facilitating heat conduction through the droplet induced a quicker droplet growth via direct condensation[165], which coupled to the greater nucleation density yielded a 388% greater coalescence rate as reported in **Fig. 9**(d). More importantly, owed to the greater droplet growth rates envisaged via direct condensation and coalescence on hydrophilic SLIPSs, condensing droplets up to 194% greater number of shedding events when compared to hydrophobic SLIPSs as in **Fig. 9**(e) were reported.

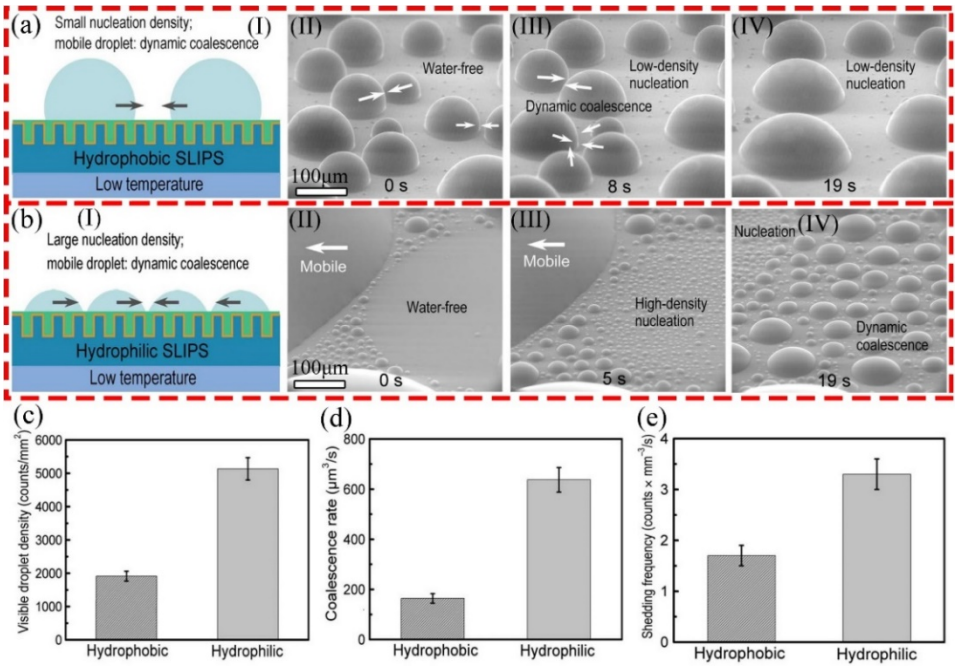


**Fig. 9. Effect of the lubricant nature on condensation performance: hydrophilic versus hydrophobic SLIPSs. (a-I) Schematic illustration of dynamic coalescence on hydrophobic SLIPS. (a-II), (a-III) and (a-IV) ESEM of condensed droplets on hydrophobic SLIPS paying special attention to the dynamic coalescence process. (b-I) Schematic illustration of dynamic coalescence on hydrophilic SLIPS. (b-II), (b-III) and (b-IV) ESEM of condensed droplets on hydrophilic SLIPS where the high density of nucleation sites on the surface are highlighted. Quantification of the (c) droplet density, (d) dynamic coalescence rate (e) and show shedding frequency on hydrophilic and hydrophobic SLIPSs[114]. Copyright 2018 American Association for the Advancement of Science.**

Guo and Tang[108] made use of Trimethoxysilane and Kryotx GPL100 as the lubricants for the hydrophilic and for the hydrophobic SLIPSs, respectively, and addressed the dynamics of condensation. Results reveal that small droplets are uniformly distributed on both the hydrophobic and hydrophilic SLIPSs at the initial stage, as shown in panels $a_1$ and $a_6$ in **Fig. 10**(a-I) and (a-II), respectively. Neighboring droplets then coalesce to form bigger droplets shedding from the surface, once contact angle hysteresis is overcome, sweeping small-sized droplets on its path, as shown in **Fig. 10**(a-I) and (a-II). In their work, the droplet density and frequency of droplet departure were found to be greater in the case of hydrophilic SLIPSs when compared to hydrophobic ones, which is consistent with the work of Dai et al.[114]. The departure diameters of droplets on hydrophilic SLIPS were found smaller than those on hydrophobic SLIPS, as shown in panels $a_2$ and $a_7$ in **Fig. 10**(a-I) and (a-II), respectively, indicating that hydrophilic SLIPSs are more effective in prompting the removal of small sized droplets compared to hydrophobic SLIPS. The wetting ridge was also found to play a critical role on both contact angle hysteresis and on droplet coalescence. **Fig. 10**(b) shows a wetting ridge/meniscus surrounding the droplet[166, 167] where the thickness of the meniscus region gradually increases with the

decrease of the distance from the droplet[91, 168-171]. The formation of the oil wetting ridge induces a lubricant thickness gradient incurring in oil-rich regions near the meniscus while oil-poor regions and in occasions oil depletion develop far from the droplet. Further, the presence of a wetting ridge and/or cloaking may suppress coalescence of two droplets owed to the presence of the thin film squeezed in between the droplets and the meniscus as they merge as in **Fig. 10**(c-II), opposed to the occurrence of coalescence as seen in **Fig. 10**(c-I)[92]. In addition, the dynamics of coalescence are also influenced by the wetting ridge and cloaking as it can be appreciated in **Fig. 10**(d), where the time required for droplets coalescence increased with the increase of oil viscosity because of higher oil viscosity hinders the breakage of the oil film and the contact between liquid droplets. More recently, Ge et al., reported on the formation of small satellite condensing droplets on lubricant-cloaked droplets without coalescing/merging with the main droplet, which hindered the heat transfer as a consequence of the additional heat transfer resistance imposed in between the ambient and the main condensing droplet[172].

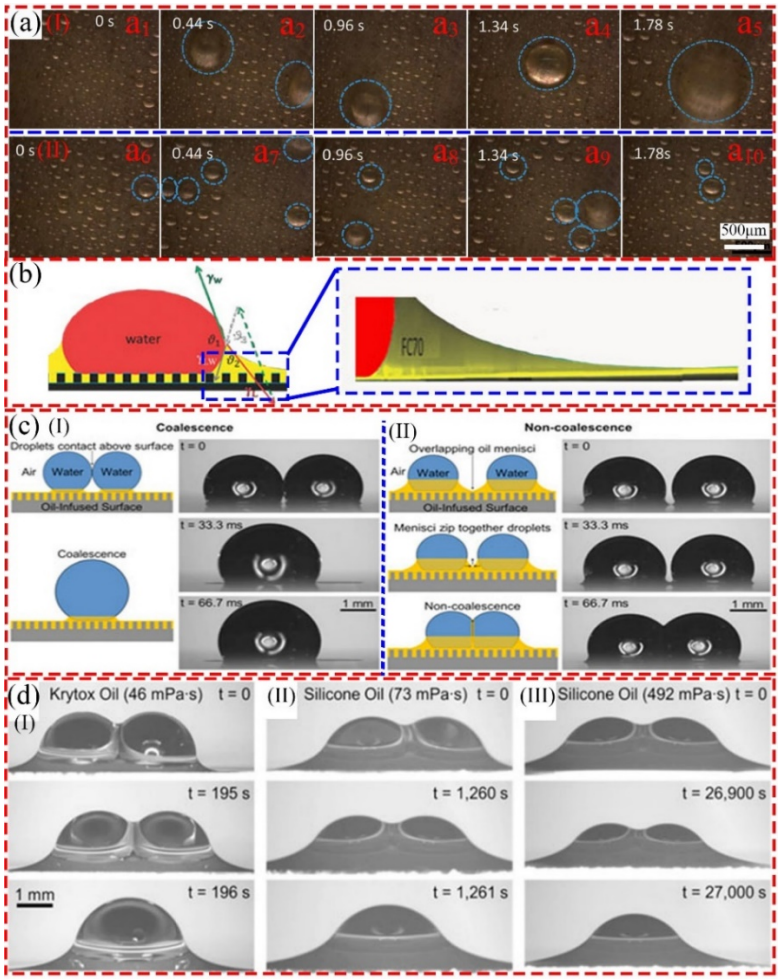


**Fig. 10. The influence of lubricant nature on droplet coalescence: hydrophilic versus hydrophobic SLIPSs. (a-I) Sequence images of condensed droplet on hydrophobic SLIPS; and (a-II) sequence images of condensed droplet on hydrophilic SLIPS[108]. Copyright 2018 Royal Society of Chemistry; (b) sketch of lubricant wetting ridge[169]. Copyright 2015 Royal Society of Chemistry. (c-I) Droplets coalescence due to the droplets colliding at liquid-air interfaces; and**

**(c-II) the lubricant film between droplets suppressed the coalescence of droplets[92]. (d) Time required for droplets to coalescence[92]. Copyright 2014 United States National Academy of Sciences.**

More recently, Sun and Weisensee[53] provided a thorough study on the dynamics of droplet nucleation and growth on SLIPS and the occurrence of self-propulsion of microdroplets within the wetting oil ridge. Results revealed the larger microdroplet nucleation rate density in the oil-poor region, as shown in dashed red rectangle in **Fig. 11**(a), as a consequence of the reduced thermal conduction resistance imposed by the thinner oil film and the lower oil-air interfacial temperature preferential for nucleation[173, 174], which has also been demonstrated in the recent work of Sun et al.[175]. Then droplets remained stationary growing through direct condensation at the nucleation sites and once they reached certain size the droplets suddenly coalesced with neighboring ones, as shown in **Fig. 11**(a). Droplets exhibited excellent mobility in the oil-rich region while droplet mobility was hindered in oil-poor regions. On one hand, in the oil-rich regions droplets gradually moved/self-propelled within the wetting ridge towards the big central droplet, and eventually they come to a halt accumulating around the big central droplet, as shown in **Fig. 11**(b). The side view images in **Fig. 11**(c) revealed that droplets move towards the big central droplet without coalescing as introduced above in the work of Boreyko et al.[92]. Capillary attraction caused by the lubricant meniscus is the driving force proposed for the self-propulsion of the droplets moving towards the big central droplet[176]. On the other hand, droplets in the oil-poor region away from the big central droplet displayed rather negligible movement because of the small curvature of the meniscus resulting in very small capillary attraction. Droplets in the oil-intermediate region accelerate towards the big central droplet reaching a maximum velocity at a certain distance from the big central droplet, and thereafter the droplets decelerate and finally stop near the big droplet without immediate coalescence, as shown in **Fig. 11**(c) and **Fig. 11**(e). The accelerated motion of droplet is mainly caused by the increase of capillary attraction due to the increasing curvature of the meniscus as the distance from the big central droplet decreases, which is represented in **Fig. 11**(d). It can be seen from **Fig. 11**(f) that the maximum velocity of the droplets decreases with the increase of lubricant viscosity, which revealed that high lubricant viscosity inhibit the droplet movement, in addition to preventing droplet coalescence[92].

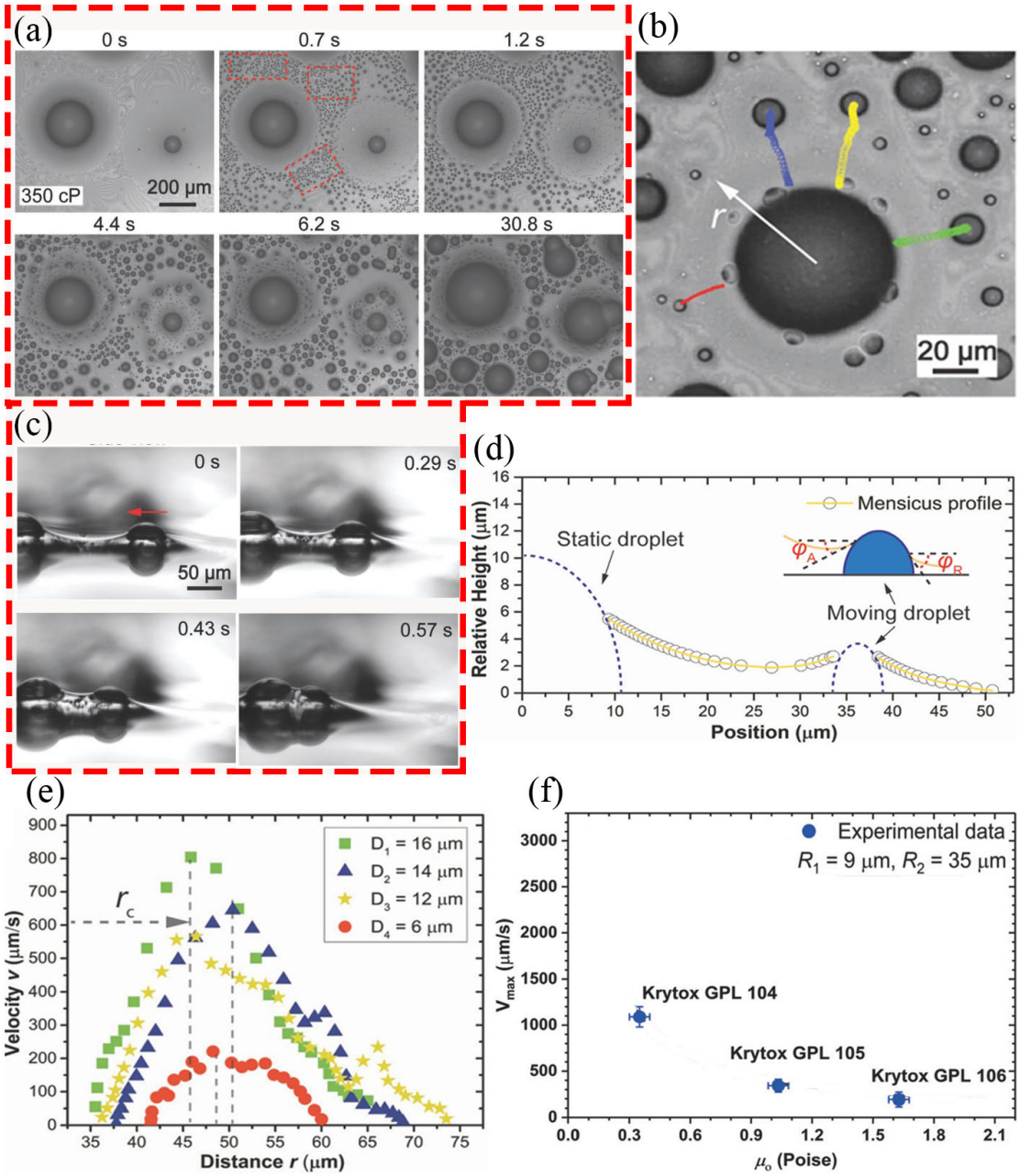


**Fig. 11. Droplet self-propulsion motion. (a) Sequence images of droplet condensation on SLIPS via optical microscopy; (b) microdroplets trajectory moving towards the bigger/main droplet; (c) typical droplet self-propulsion captured from side view; (d) schematic of capillary induced movement for the condensed droplet in the meniscus region of a bigger droplet including actual quantification of the meniscus profile; (e) relationship between the velocity of moving droplets, their size and the distance from the main droplet; (f) influence of lubricant viscosity on maximum velocity[53]. Copyright 2019 Royal Society of Chemistry.**

More recently, the spontaneous thermocapillary motion of condensed droplets on heterogeneous SLIPSs was investigated by Zhu et al.[110], where droplet condensation preferentially occurred at the PTFE clusters of the heterogeneous SLIPSs and induced a nonuniform temperature distribution. The condensed droplets moved directionally towards the cold region due to the thermocapillary force generated from the interfacial tension gradient between the oil film and the condensed droplet. The spontaneous motion occurring from the thermocapillary migration reported, was able to drive

millimeter droplets against gravity on the heterogeneous SLIPSs and to significantly increase the condensation rate up to two times when compare to homogeneous SLIPS. Note that the adhesion of the droplet or condensate to the SLIPS can also be controlled in the presence of a lubricant with phase-change attributes near the desired working temperature. Raza et al., demonstrated the different adhesion states of a droplet and the different droplet size distributions during condensation for a superhydrophobic surface impregnated with paraffin, which has a melting temperature between 52 °C and 60 °C. Above 60 °C the paraffin is in the liquid phase and the slippery state characteristic of SLIPS was achieved with shedding of small sized droplets, whereas at lower temperatures, the solid phase and mush phase of the paraffin ensues with the enhance adhesion[177].

### 4.1.2 Condensation on millimeter scale patterned SLIPS

Inspired by the excellent droplet condensation capabilities of the bumpy geometry of Namib desert beetles, DWC on aluminum slippery asymmetric bumps was investigated by Park et al.[99]. In their work the surface curvature played a major role for droplet condensation. The study of droplet growth on millimetric spherical cap-shaped bumps demonstrated the greater growth via direct condensation and coalescence on the apex of a bump when compared to nearby flat regions, i.e., when comparing the yellow dotted circles represented in **Fig. 12**(a-II) and (a-III). Condensing droplets on SLIPSs comprising asymmetric bumps grow much faster compared to droplets on flat SLIPS. As a consequence of the quicker droplet growth on slippery asymmetric bumps, condensing droplets are able to reach the critical departure diameter and to shed from the surface with the assistance of gravity faster than on flat smooth SLIPS. Note that, when looking into **Fig. 12**(b) for the same condensation time the presence of available regions for droplet nucleation and growth on asymmetric bumps SLIPSs evidences the occurrence of droplet shedding opposed to flat SLIPS. The normalized condensation heat flux, namely the ratio of condensation heat flux on SLIPSs decorated with millimeter sized convex bumps to that on flat SLIPS, increased with the increase of surface curvature as estimated in **Fig. 12**(c), which revealed that surface curvature promotes condensation. The above was further supported and demonstrated in the work of Yao et al. on SLIPSs decorated with hydrophobic bumps and dimples[178].

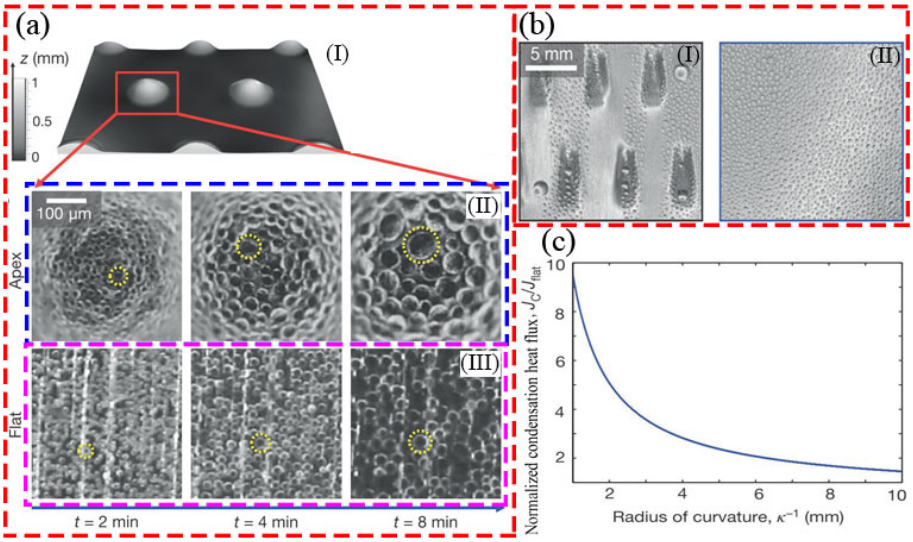


**Fig. 12. Droplet condensation on slippery asymmetric bumps. (a-I) Profilometer image of millimeter-sized spherical-cap-shaped bumps; (a-II) and (a-III) sequence images of droplets growth on the apex of convex bumps and on the flat region of SLIPS, respectively. (b-I) Condensation and shedding of droplets on convex bumps and (b-II) condensation in the absence of shedding on flat SLIPS for the same condensation times. (c) Relationship between condensation heat flux on the apex of spherical bumps to that on a flat surface function of the radius of curvature[99]. Copyright 2016 Nature Research.**

Kajiya et al.[156] investigated the condensation behavior on V-shaped grooved SLIPSs. In their work, unique cylindrical chains of droplets were found as a consequence of droplet coalescence. The sizes of the coalesced droplets were in the same order of magnitude as the width of the grooves. Once reached the groove size condensing droplets tend to grow in the direction of the grooves as shown in **Fig. 13**(a-I), (a-II) and **Fig. 13**(b). While droplets nucleating and growing at neighboring grooves do not coalesce with each other, as the valley wall acts as a barrier for coalescence of droplets with sizes in the same order of magnitude as that of the valleys, which is shown in **Fig. 13**(a-III). Then, as the cylindrical chains of droplets in the neighboring valleys of the prism/groove grow bigger with sizes above that of the grooves' width, droplet chains merge with each other forming a big droplet displaying spherical cap shape as illustrated in **Fig. 13**(c-I) and (c-II). The cylindrical chains of droplets in the valleys of prism exhibited high mobility due to low hysteresis force between droplets and lubricant[164, 179, 180]. Re-nucleation was favored in the refreshed valleys of the prism after the sweeping of the cylindrical chains of droplets, as shown in **Fig. 13**(d), which could significantly improve the condensation heat transfer performance. More recently Li et al.[181] investigated the directional transport of condensing droplets on SLIPSs decorated with diverging channels where droplets initially nucleate and grow on the channel wall and are then swiped into the channels by coalescence. Droplets are confined in the diverging channels, imposing a difference of curvature between front and rear ends

of the droplet enabling the droplet motion along the channel direction. Directional droplet removal on hydrophilic parallel SLIPS was also studied by Dai et al.[114], where experimental results revealed that the slippery parallel grooves were favorable for droplet coalescence and were efficient for rapid droplet removal because the parallel structures with slippery interface significantly reduce the droplet hysteresis force. The condensation rate on SLIPSs decorated with parallel grooves was 23.9% higher than that on hydrophilic flat SLIPS demonstrating that the hydrophilic parallel SLIPS are beneficial for promoting condensation and heat transfer.

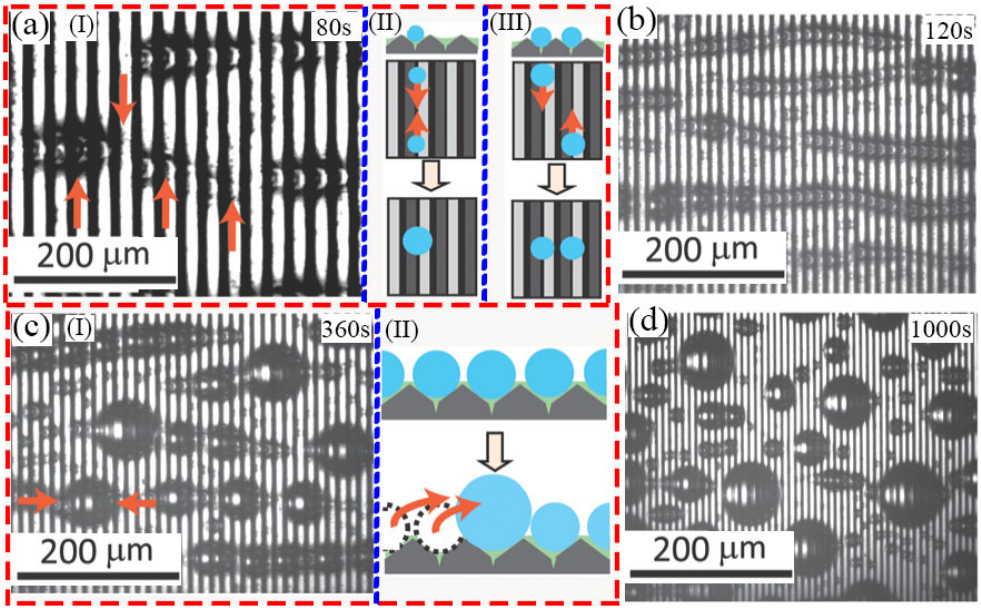


**Fig. 13. Sequence images of condensed droplets on prism-patterned/grooved SLIPSs. (a-I) Condensing droplets grow along the grooves direction; (a-II) schematic of droplets coalescence at the same valley of the prism; (a-III) schematic of droplets that did not coalesce at neighboring valleys of the prisms; (b) the cylindric chains of droplets were formed; (c-I), (c-II) and (d) droplets coalesced over neighboring valleys of the prisms[156]. Copyright 2016 Royal Society of Chemistry.**

The continuous droplet nucleation, growth and coalesce with rapid shedding, in the presence of millimeter and submillimeter scale patterns on SLIPS when compared to homogeneous SLIPS[99, 114, 182] can in turn enhanced droplet transport and the heat transfer performance. Patterned SLIPSs may facilitate the coalescence of small-sized droplets accelerating droplet growth and eventually droplet shedding owed to the imposed structural and/or chemical surface gradients, which plays a crucial role for inducing microscale droplet transport and collection eventually accelerating condensation. In the next sub-sections we pay close attention to microscale droplet directional transport on bioinspired gradient structured surfaces.

### 4.2. Directional droplet transport during condensation on bioinspired gradient structures

Although, as introduced above, SLIPSs can promote the random motion of condensed droplets, in the absence of gravity and/or external forces applied, droplets cannot effectively and rapidly shed from the surface. To counteract such shortcomings, unidirectional droplet movement has been proposed, which plays an important role in microfluidics, thermal management and condensation applications. The passive transport of condensed micrometer-sized droplets via chemical or structural wetting patterns (i.e., without external forces applied such as electrowetting[183, 184], mechanical vibration[185] and/or mechanical brushes[186] that may breakdown and/or introduce other applicability drawbacks) is desirable for continuous and efficient microfluidics and DWC heat transfer[54, 122, 151, 187]. To date, the controllable manipulation of small sized droplets, i.e., micro-droplets, remains a great challenge as hysteresis forces opposing to the droplet motion become increasingly important with the decrease of the droplet size[117]. Inspired by the efficient transport regulation of microscale droplet by natural plants and insects[98, 99, 120, 135], researchers have focused on exploiting different strategies to enhance droplet mobility via surface chemical and/or structural wettability gradients and/or Laplace pressure gradients as the driving force[54, 123, 188]. Below recent strategies proposed by different researchers and groups aiming to create effective surfaces and/or structures exploiting wettability gradients and Laplace pressure for facilitating droplet shedding and hence accelerating re-nucleation are summarized.

#### 4.2.1 Droplet transport controlled by surface wettability gradient

In this subsection recent advances and progress on droplet transport governed by surfaces comprising a chemical or a structural wettability gradient are introduced and summarized. The transport of droplets and fog harvesting ability of a copper wire comprising a surface wettability gradient were investigated by Xing et al.[126]. Results revealed that droplets moved from the less wettable region to a more wettable region along the wettability gradient of the copper wire, as shown in **Fig. 14**(a), (b) and (c). The distance traveled by the droplets increased when increasing the wettability gradient with a maximum displacement at a surface wettability gradient of 14°/mm as represented in **Fig. 14**(d), which is owed to the increasing wetting force of the surface wettability gradient. As the surface wettability gradient is further increased, hysteresis forces become more prominent and the droplet moving distance decreases. On the pristine copper wire droplets grew via direct condensation while on the wettability gradient copper wire drops grew via direct condensation and coalescence as they sweep the wire as illustrated in **Fig. 14**(e) and **Fig. 14**(f) respectively. The droplets growth rate on the wettability gradient copper wire is greater than on the pristine copper wire

as shown in **Fig. 14**(g), which demonstrates that the copper wire with a wettability gradient inducing the unidirectional motion of the droplet transport displayed more efficient water collection capabilities.

The droplet transport on wettability patterned surfaces was studied by Ghosh et al.[131]. In their work droplets were confined in wedge-shaped superhydrophilic stripes patterned on a superhydrophobic background. The liquid droplet propagated along the transverse direction and was confined in the wedge-shaped superhydrophilic stripe as shown in **Fig. 15**(a). The droplet front spread towards the wider end of the stripes reducing the liquid transport resistance[189] followed by the liquid bulge. From **Fig. 15**(b) it can be appreciated that the diameter of the elliptical droplet is much larger than the width of the wedge-shaped superhydrophilic stripes while the droplet base radius is constrained at the superhydrophobic-superhydrophilic boundary of the stripes. The propagation of the liquid droplet towards the wider wedge of the superhydrophilic stripe is a consequence of the driving force imposed by the difference in curvature being larger at the rear of the droplet than that at the front of the droplet[190]. The influence of surface wettability gradient and structural confinement on droplet transport was numerically investigated by Chowdhury et al.[191]. A nondimensional wettability gradient stripe of width ($w^*$) on a superhydrophobic background stripe was considered where the nondimensional stripe width was defined as the ratio of the width of the wettability gradient stripe to the initial droplet diameter. The numerical results revealed that the droplet reached its maximum transport velocity when the nondimensional stripe width was equal to 0.8, and the droplet transport velocity was significantly reduced if the nondimensional stripe width was below 0.8. In addition, the droplet transport velocity on a superhydrophilic stripe on a superhydrophobic background was larger than the superhydrophilic-hydrophilic and the superhydrophilic-hydrophobic counter parts as expected.

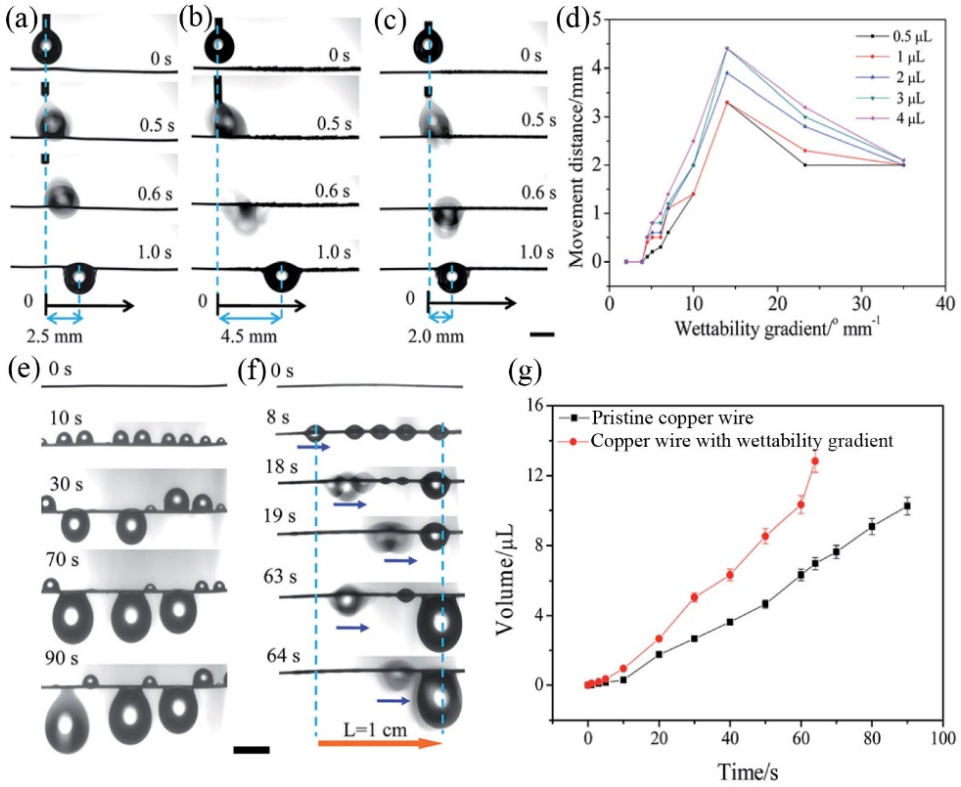


**Fig. 14. The droplet movement behaviors on copper wire with different surface wettability gradient. (a) Surface wettability gradient of 10 °/mm; (b) Surface wettability gradient of 14 °/mm; (c) Surface wettability gradient of 35 °/mm; (d) Movement distance of droplets varying in volume on copper wires with different surface wettability gradients; (e) & (f) Droplet growth behavior on pristine and surface wettability gradient copper wires, respectively; (g) Droplets collection abilities on pristine and surface wettability gradient copper wires[126]. Copyright 2017 Royal Society of Chemistry.**

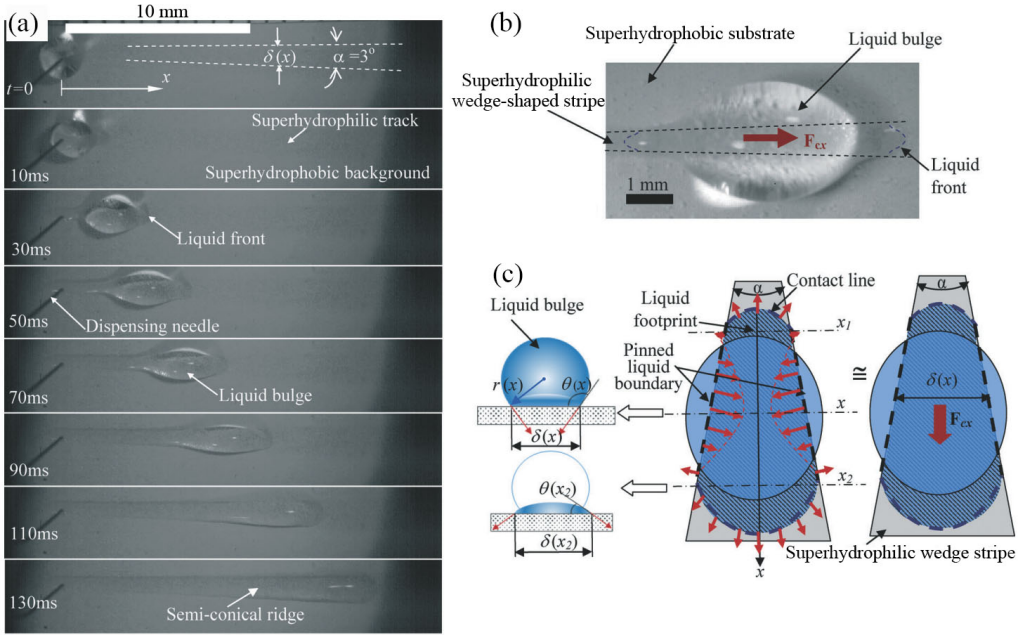


**Fig. 15. Droplet dynamics on wedge-shaped superhydrophilic stripe. (a) Sequence images of droplet transport on the wedge-shaped superhydrophilic stripe; (b) Elliptic morphology of droplet on the wedged-shaped superhydrophilic stripe; (c) Schematics of the forces and net driving force responsible for the droplet transport on the superhydrophilic stripe[131]. Copyright 2014 Royal Society of Chemistry.**

In the same line of research, Liu et al.[157] investigated the directional droplet collection and transport on wedge-shaped surface wettability gradient stripes. The wedge-shaped superhydrophilic stripes consisted of copper hydroxide nanowires (contact angle of 3°) were evenly separated by hydrophobic PET (polyethylene terephthalate) (contact angle of 94°) as shown in **Fig. 16**(a-I). The high wetting contrast caused the condensed micrometer-sized droplets to move towards the superhydrophilic stripes[192-195]. A water film was formed on the superhydrophilic stripes, and simultaneously a large number of micrometer-sized droplets were formed on the hydrophobic PET interval regions after the onset of condensation, as illustrated in **Fig. 16**(a-II). As condensation ensues, micrometer-sized droplets denoted by the red circle on the hydrophobic PET stripes are immediately swept into the film covering the superhydrophilic copper hydroxide nanowires (represented in **Fig. 16**(b-II)) once the droplet grew big enough to touch the water film[62, 196, 197]. Then new area is available for the continuous droplet nucleation and growth on the hydrophobic stripes, as shown in **Fig. 16**(c). On the no patterned extremes of the surfaces, neighboring droplets coalesced to form big stationary droplets, as shown in **Fig. 16**(d). In contrast, droplets formed on the patterned region coalesce and then were transported to the wider regions of the superhydrophilic stripes seemingly to the work of Ghosh et al.[142], as shown in **Fig. 16**(d), which significantly enhances the droplet collection and the transport efficiency towards the more wetting region. In order to further investigate the factors influencing both the coalescing time and droplet coalescence speed, the nondimensional parameter $\omega$ was proposed as the ratio droplet diameter to width of the superhydrophilic stripe, namely $\omega=D_d/W_t$. The coalescing time increased with the increase of $\omega$, whereas the coalescing speed increased gradually and then decreased subsequently, as shown in **Fig. 16**(e). The coalescing speed decreased to zero when the droplet diameter was much larger than the width of superhydrophilic stripe implying that big droplets easily kept stationary on the narrow superhydrophilic stripes in region III, as shown in **Fig. 16**(d), which revealed that small $\omega$ was necessary for maintaining highly efficient droplet collection and transport.

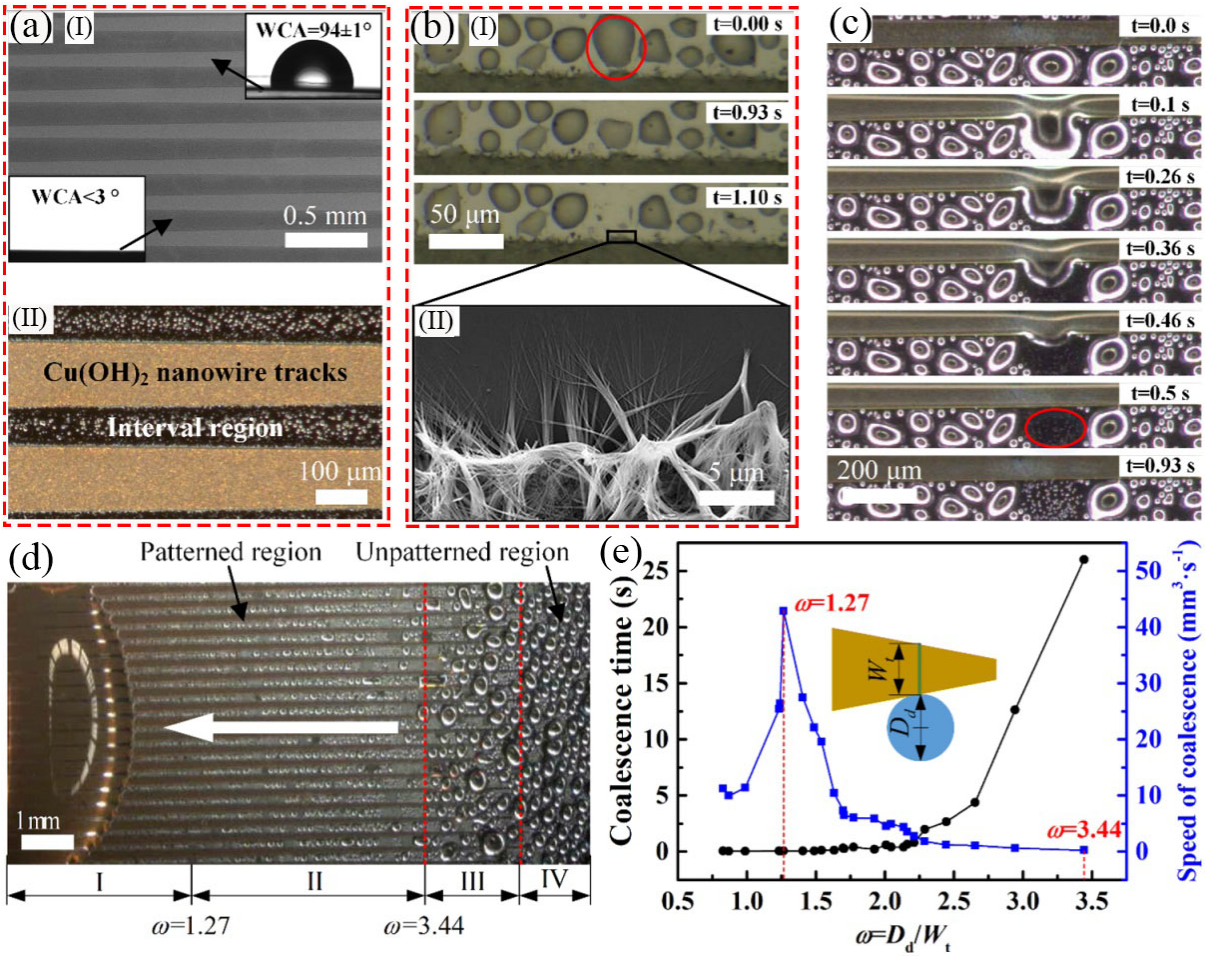


**Fig. 16. The condensed droplets dynamics on wedge-shaped stripes with wettability gradient. (a-I) SEM of wedge-shaped pattern, the inset top right and bottom left images were water contact angles of bare PET and copper hydroxide stripes, respectively; (a-II) Onset of condensation on the wedge-shaped pattern; (b-I) Condensed microscale droplet swept into the superhydrophilic copper hydroxide nanowires; (b-II) SEM image of copper hydroxide nanowires at the stripe boundary; (c) Condensed droplets swept into the wedge-shaped superhydrophilic stripe; (d) Droplets collection and transport on the wedge-shaped superhydrophilic stripes; (e) Coalescence time and speed versus ratio of droplet diameter to width of stripe[157]. Copyright 2018 American Chemical Society**

More recently, droplets collection and transport on a bioinspired venation network with high contrasting wettability were investigated by Liu et al[159], where asymmetric superhydrophilic channels were surrounded by a superhydrophobic background, respectively. The droplets on superhydrophobic region were sucked into the aequilate superhydrophilic channels feeding the main droplet or water reservoir as shown in **Fig. 17**(a). Owed to the asymmetry of the superhydrophilic channels droplets were also transported along the channels and then to the water reservoir via the microscale and millimeter scale channels as illustrated in **Fig. 17**(b) and (c), respectively. Both the microscale and millimeter scale channels were capable of transporting the collected water towards the water reservoir, as illustrated in **Fig. 17**(d). The water film present on the dendrite superhydrophilic pattern is able to transport the condensate (droplets nucleating and growing on the superhydrophobic regions) towards

the reservoir as illustrated in **Fig. 17**(e). It can be seen from **Fig. 17**(f) that micrometer-sized droplets on the superhydrophobic regions coalesced and were instantly sucked into the film covering the superhydrophilic tracks. The height of the cross-section of the collected water within the channels increased after a droplet sweeping event, and finally the height reduced to minimize surface energy as the water was transported to the water reservoir as represented in **Fig. 17**(g). This is in agreement with the transport of the liquid bulge reported in the work of Ghosh et al.[142]. The excellent droplet transport and collection capabilities of the dendrite aequilate superhydrophilic-superhydrophobic patterned surface combining microchannels and minichannels with variant width was here demonstrated.

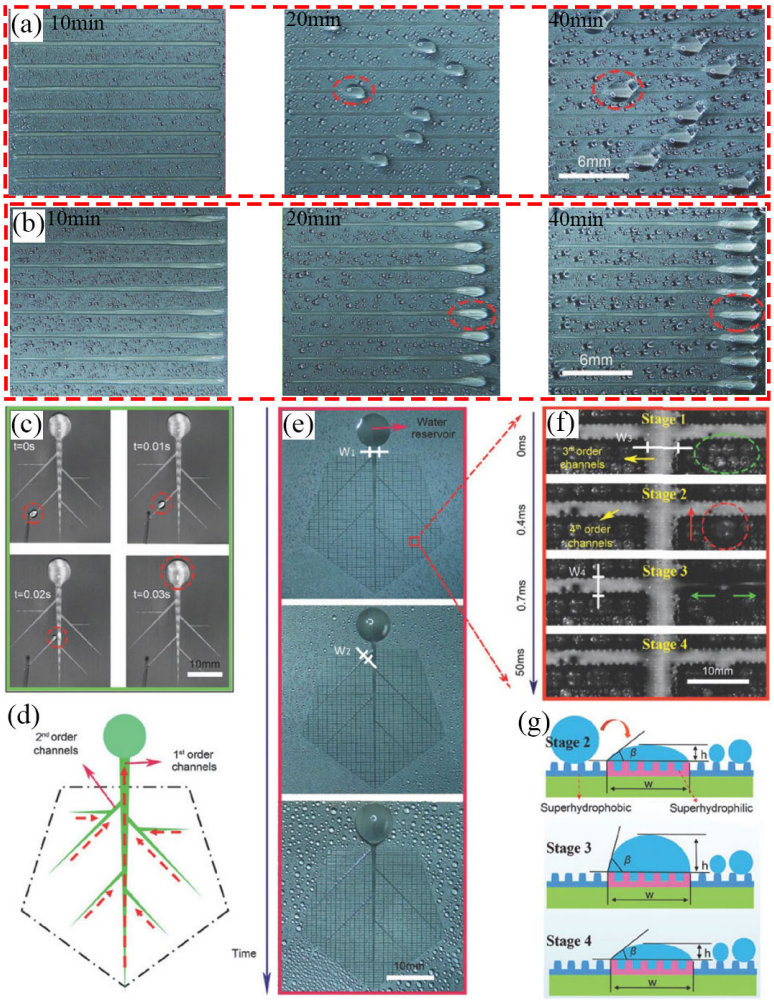


**Fig. 17. Droplet dynamic behaviors on dendrite aequilate superhydrophilic patterned surfaces. (a) Sequence images of droplets collection on aequilate superhydrophilic channels on a superhydrophobic background; (b) Sequence of droplets transport on asymmetric superhydrophilic channels on a superhydrophobic background; (c) Droplet transported through the asymmetric channel network; (d) Schematic illustration of droplet transport directions in the channel network; (e) Time-lapse images of droplets collection on the wettability network; (f) Droplets being swept into the superhydrophilic channels where red and green solid arrows denote the movement direction of a droplet on superhydrophobic region and the droplet transport direction in the superhydrophilic channel respectively; (g) Schematic illustration of tiny droplets being swept into the superhydrophilic channel[159]. Copyright 2021 American Chemical Society.**

### 4.2.2 Droplet collection and transport controlled by Laplace pressure gradient

In this subsection we review strategies on droplet transport induced by differences in Laplace pressure generated within the droplets as a consequence of the conical shape of the proposed structures. The Laplace force generated by the pressure gradient of the curvature surface can drive and guide the condensed droplets transport to region of interest[198]. Inspired by the excellent droplet transport capabilities of the cactus spine, Ju et al.[89] investigated the water collection on conical copper spines during condensation. The droplet collection processes on hydrophilic, hydrophobic and gradient wettability conical copper spines with apex angles of 12° are illustrated in **Fig. 18**(a-I). On one hand, the droplet growth rate on the hydrophilic conical copper spine was much slower than that on hydrophobic ones, while on the other hand the droplet transport velocity on the hydrophilic conical copper spine was greater than that on hydrophobic one as shown in **Fig. 18**(a-II). The conical copper spine with gradient wettability had a growth rate and transport velocity in between those reported on hydrophilic and hydrophobic copper spines. Experimental results showed that both the droplet growth rate and transport velocity on three kinds of conical copper spines increased with the increase of apex angle as represented in **Fig. 18**(a-II). It is worth noting the integrated merits of the conical copper spine with wettability gradient having droplet growth rates and transport velocities above the hydrophobic and the hydrophilic conical wires, respectively, eventually inducing more efficient and continuous droplet transport. The droplet transport on hexagonally arranged conical spine arrays was studied by Ju et al.[188]. Droplets randomly nucleated on the conical spine and then they grew through direct condensation pinned at their initial nucleation sites. It can be seen from **Fig. 18**(b) that the droplets were transported towards the base of the conical spine once the droplet was large enough so that gravity forces overcome the hysteresis force. Thereafter a new nucleation and growth frequency began on the conical spine refreshed area. In their work, droplets grew mainly by direct condensation but also by coalescence with neighboring ones. Droplet coalescence was more favorable for driving droplet transport towards the base of the conical spine. This was due to the sudden increase in droplet mass and hence in gravity force pulling the droplet downwards as well as by the release on the excess kinetic energy from upon a coalescence event ensues, which helped to overcome the hysteresis forces responsible for the pinning of the droplets. The efficient water droplet collection on artificial cactus spines with hierarchical grooved structures was investigated by Bai et al.[199]. Condensing droplets initially nucleated and grew at the tip of the artificial spine and then coalesced to form big droplets. Once the droplet reached certain size, the transport of the droplet from the tip to the base of the artificial

spine ensued independently of the direction of gravity as shown in **Fig. 18**(c-I). The droplets grew initially via direct condensation and through coalescence during the transport processes. The transport velocity of droplet on artificial spine with nanogrooved structures was much larger than that on a smooth spine surface as additional Laplace driving force arising at the nanogrooves. The numerous nanogrooved structures on the artificial spine surface could also generate capillary forces. In their work the cooperation of Laplace and capillary forces endowed the artificial spine with excellent droplet collection and transport capabilities, as shown in **Fig. 18**(c-II).

The droplet behavior on spines integrating functional multi-structure were studied by Ju et al.[86]. The spines consisted of three parts with different structural features, namely the tip containing oriented barbs, the middle containing gradient grooves and the base containing belt-structured trichomes. It can be seen from the panel $d_1$ in **Fig. 18**(d-I) that the microscale droplet was formed on the tip of the oriented barb, and then it was transported towards the base of the barb and coalesced with neighboring droplets already present at the spine hosting the barbs creating bigger droplets during the condensation. Micrometer-sized droplets moved from the tip to the base of the barb driven by the difference of Laplace force between the front and the rear of the droplets. Thereafter new droplets re-nucleate on the refreshed tip of the barb commencing a new droplet condensation cycle. Droplets from the oriented barbs were collected together to form bigger droplet on the spine and then bigger droplets were transported from the tip to the base of the spine due to the combination of Laplace force capillary action induced by the asymmetrical structures of the oriented barbs, as shown in panel $d_2$ in **Fig. 18**(d-I). Upon reaching the base of the spine, droplets were rapidly collected by the trichomes structures present at the base of the spine and trichomes due to the strong capillary force generated by the spine and trichomes, as shown in panel $d_3$ in **Fig. 18**(d-I). The rapid droplet transport from the tips of the barbs towards the base of the spine accelerated the condensation eventually improving the condensation performance. The spine also contained microgrooves with increasing width when moving from the tip towards the base, as shown in **Fig. 18**(d-II), incurring additional Laplace force eventually accelerating droplet transport. The water droplet collection on a conical spine decorated with an array of branched conical wired structures was investigated by Heng et al.[120], which is shown in **Fig. 18**(e-I). It can be seen from **Fig. 18**(e-II) that small sized droplets first nucleated at the tip of the branched wires owed to the largest curvature at the tips when compared to the other parts of the branched wires[99, 178]. Thereafter several droplets gradually formed along the longitudinal direction of the branched wire via direct condensation and coalescence with other droplets. Droplets at the tips were transported towards their root along the branched wire due to the Laplace force generated by the

conical shape of the branched wires. Additionally a precursor water film was formed along the branched wire during the droplet transport process, which was beneficial for the rapid water transport[200]. Droplets on the branched wires then merged to form bigger droplets at their root. Finally, the big droplets located on the roots of the branched wires were transported to the base of the conical spine, which revealed that the Laplace force generated by the conical-shaped structures played a significant role in the droplet self-propel transport. Xu et al.[136] investigated the water droplet collection capabilities and droplet unidirectional transport on gradient conical copper wire comprising periodic roughness-gradient regions along the longitudinal direction. The surface wettability gradient was accomplished by the periodic surface roughness[81, 201-204]. Micrometer-sized droplets were randomly formed on the conical copper wire and transported from the less wettable region to the more wettable region, namely from low to high roughness. Finally, micrometer-sized droplets were collected at the more wettable region forming a big droplet as shown in panel $f_2$ in **Fig. 18**(f). Schematics representing the Laplace force arising from the conical geometry of the copper wire responsible for overcoming the hysteresis force is shown in panel $f_4$ in **Fig. 18**(f). On one hand, the surface wettability gradient was beneficial for the coalescence of micrometer-sized droplets into a bigger droplet, while on the other hand the Laplace force could transport the bigger droplet from the tip to the base of the conical spine[198]. Although the surface wettability gradient and Laplace pressure gradient played different parts in droplet dynamic behaviors, their synergistic effect was responsible for the enhanced droplet transport and shedding from the spine surface.

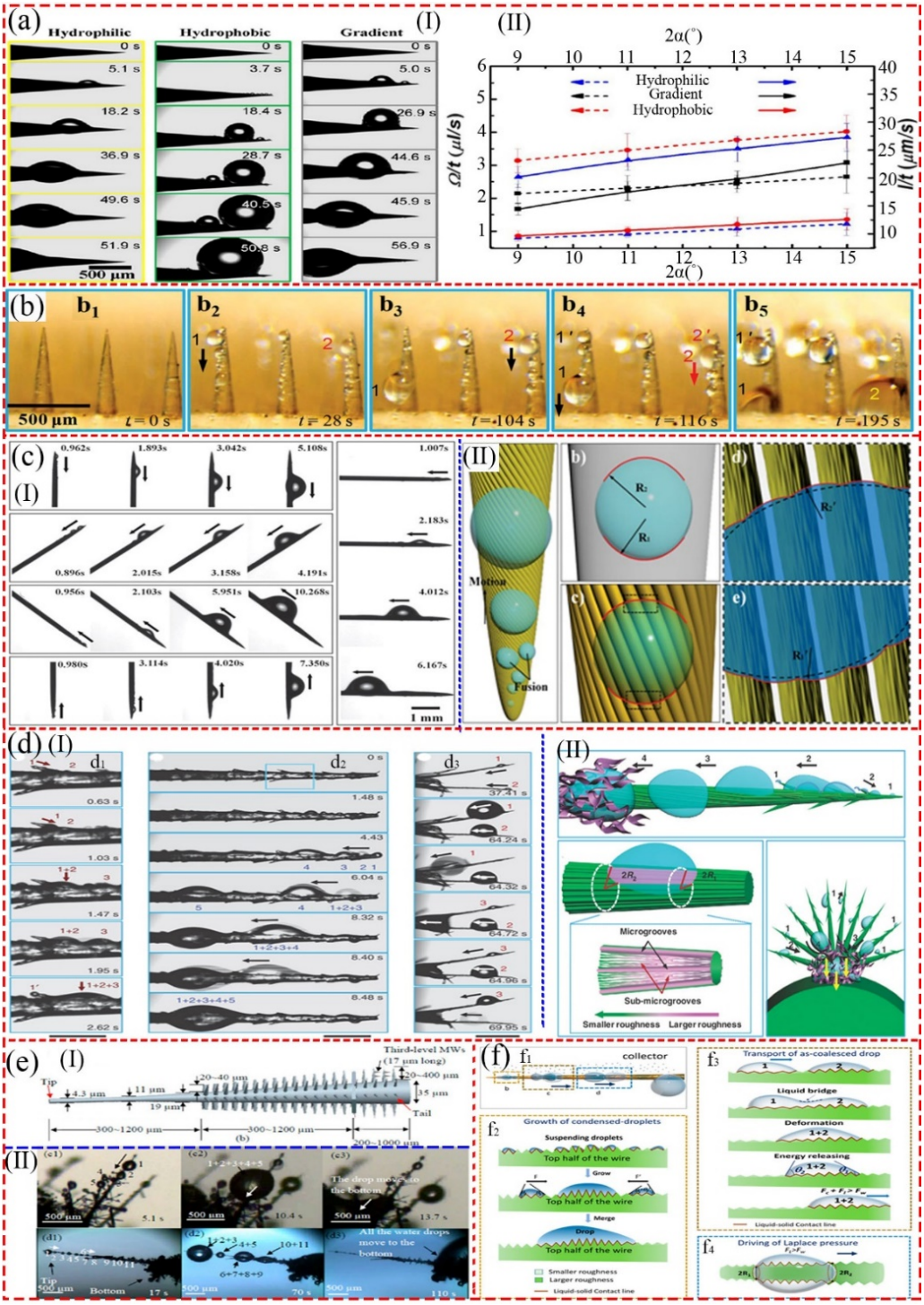


**Fig. 18. Droplet condensation, collection and transport on conical spines. (a-I) Droplet collection on conical spines with different wettability; (a-II) statistical analysis of droplet collection on conical spines with different wettability[89]. Copyright 2013 Wiley-VCH; (b) water droplet collection behavior of hexagonally arranged conical spines array[188]. Copyright 2014 Wiley-VCH; (c-I) microscopic observation of droplet movement on the artificial cactus spine; (c-II) movement mechanism of droplet on the artificial cactus spine[199]. Copyright 2015 Wiley-VCH; (d-I) continuous droplet collection and transport on horizontal spine and two neighboring spines with trichomes; (d-II) droplet collection mechanism of conical spine with multi-level grooves[86]. Copyright 2013 Nature Research. (e-I) synthesized conical spine with branched conical wire structures; (e-II) droplet collection and transport on synthesized spine with branched wire structures[120]. Copyright 2014 American Chemical Society; (f) condensed droplet growth transport arising from driving force of rough spines[136]. Copyright 2016 American Chemical Society**

### 4.2.3 Droplet transport controlled by multi-gradient cooperation

In this subsection we introduce advance functional surfaces combining chemical or structural wettability gradients with conical shapes inducing Laplace forces, i.e., multi-gradient cooperation, inducing controlled droplet transport. Directional droplet collection and transport on spider silk were investigated by Zheng et al.[98], where the spider silk was composed of the periodic spindle-knots and joints, as shown in **Fig. 19**(a-I). The spindle-knots had highly random nanofibrils which exhibited rough surface morphologies, while the joints showed smooth surface morphologies. The surface wettability gradient was generated due to the surface rough features of the periodic spindle-knots and joints, and the wetting force would drive droplet moving towards more wettable region, as shown in **Fig. 19**(a-II). The Laplace pressure gradient was generated due to the difference in curvature between spindle-knots and joints, and the multi-gradient cooperative force integrating the surface wettability gradient and Laplace pressure gradient driven droplet transporting from joints to spindle-knots, as shown in **Fig. 19**(a-II). The droplets were randomly condensed on the spindle-knots and joints and then grew in situ through direct condensation, as shown in panel $a_1$ in **Fig. 19**(a-III). Droplets on the joints would gradually transport towards the nearest spindle-knots, and then several droplets were suddenly coalesced into a big droplet at the spindle-knot, as shown in panels $a_2$ and $a_3$ in **Fig. 19**(a-III), which revealed that multi-gradient cooperative force arising from the periodic spindle-knots and joints of the spider silk played a crucial role for the directional droplet transport during the highly efficient condensation process. Size-triggered droplet target transport on gradient-step spindle-knot fibers was studied by Xue et al.[149], where the gradient-step spindle-knot fibers had unidirectional, middle and two-side symmetric spindle-knots to control directional droplet target transport. Droplets were firstly condensed on the unidirectional gradient fiber composed of five spindle-knots increase in size, and then the droplets successively coalesced into big droplet and transported towards the biggest spindle-knot, as shown in panel $b_1$ in **Fig. 19**(b-I). The unbalance gradient force arising from the curvature differences between the spindle-knots propelled the droplets to transport from the small spindle-knot to the big ones, and the capillary adhesion force was simultaneously increased with the size increase of spindle-knot, as illustrated in panel $b_2$ in **Fig. 19**(b-I). The multi-gradient cooperative force arising from the Laplace pressure gradient and capillary adhesion force would accelerate the droplet transport, as shown in panel $b_3$ in **Fig. 19**(b-I). For the gradient-step fiber with middle symmetric gradient spindle-knot, the droplets 1, 2 and 3 coalesced into big droplet (1+2+3) at the middle of the gradient-step spindle-knot fiber, and the droplets 4 and 5 simultaneously merged into big droplet (4+5) at the

middle right side, and finally two big droplets would further coalesce into the biggest droplet at the middle of the gradient-step spindle-knot fiber, as shown in panel $b_4$ in **Fig. 19**(b-II). Condensed droplets transported towards the big spindle-knot at the middle of the gradient-step spindle-knot fiber due to the larger multi-gradient cooperative force, as shown in panel $b_6$ in **Fig. 19**(b-II). For the droplets transport on the gradient-step fiber with two-side symmetric gradient spindle-knot, the droplets would transport towards the large spindle-knot at each end of gradient-step spindle-knot fiber, as shown in panels $b_5$ and $b_7$ in **Fig. 19**(b-II), which indicated that the size of the spindle-knot would effectively control the droplet target transport for droplet collection. Water harvesting on bioinspired nanocone-decorated three-dimensional fiber network (N3D) was also investigated by Li et al.[153], where the crossing fiber of the N3D was decorated with hydrophilic zinc oxide nanocones. Condensed droplets were randomly formed on the crossing fiber of the N3D at the early stage, and then the small droplets would rapidly transport to the crossing location along the crossing fiber, and finally the big droplet detached from the crossing location once the droplet gravity overcame the hysteresis force, as shown in **Fig. 19**(c-I). The crossing fiber of the N3D was wetted by a thin liquid film due to hydrophilic zinc oxide nanocones, and the liquid film could be used as a precursor which was beneficial for the droplet transport. The first droplet dropping off from the fiber took 340 s, while the droplet in the second cycle took only 226 s, as shown in **Fig. 19**(c-I), which revealed that the liquid precursor on the hydrophilic crossing fiber reduced the droplet transport resistance and promoted droplet to move towards the crossing location[189, 200]. The rapid increase in droplet volume would accelerate the droplet detached from the crossing location, as shown in **Fig. 19**(c-II). The N3D had a large number of fiber branches and significantly promoted liquid collection performance.

The water droplet condensation, collection and transport on the integrative system comprising micro/nanostructured conical spines (MNCS) horizontally fixed on the vertical Janus membrane (JM) with a superhydrophobic inside and a hydrophilic outside were investigated by Zhou et al.[140]. Droplets easily formed on the tip of the conical spine compared with other regions of the conical spine. The Laplace force arising from the Laplace pressure gradient of the conical spine driven the droplet transported from the tip to the base of the conical spine once the Laplace force overcame the hysteresis force, as shown in panel $d_1$ in **Fig. 19**(d). The moving droplets would coalescence with other droplets to form bigger ones then converting the excess surface energy into kinetic energy[205-208]. The Laplace force and energy release force of droplet coalescence could be effectively integrated to generate a cooperative force for efficient droplet transport, as shown in panel $d_2$ in **Fig. 19**(d), which was beneficial for the continuous long distance transport of coalesced droplet. The wetting force was

generated by difference between superhydrophobic side and hydrophilic side of JM once the coalesced droplet reached the superhydrophobic side of the JM, and the coalesced droplet suffered strong wettability gradient force arising from the cooperation of hydrostatic pressure and hydrophobic force[209, 210], as shown in panel $d_3$ in **Fig. 19**(d). Although the hydrophobic force partially impeded the penetration of coalesced droplet through the JM, the hydrostatic force propelled the coalesced droplet to pass though the aperture of JM because the hydrostatic force was much larger compared with the hydrophobic force[209]. The as-penetrated droplets would collect together and then detached from the hydrophilic surface of JM once the coalesced droplet penetrated through the superhydrophobic side to reach the hydrophilic side of JM, which was beneficial for the highly efficient droplet collection and transport. The directional droplet transport on porous membrane with conical nanoneedles was investigated by Wang et al.[211], where the pierced nanowire porous membrane composed of the piercing hydrophilic conical nanoneedles and asymmetric wettable porous membranes. It can be seen from the panels $e_1$ and $e_3$ in **Fig. 19**(e) that the droplet was immediately absorbed and transported to the backside of porous membrane once the droplet contacted the punctured surface. However, the droplet did not transport on the region of porous membrane in absence of hydrophilic conical needles, as shown in panels $e_1$ and $e_4$ in **Fig. 19**(e). It can be seen from the panels $e_5$ and $e_6$ in Fig. 19(e) that the cooperative force arising from the hydrophilic conical needle driven the droplet to move from the tip to the base of the hydrophilic conical needle, and then the droplet rapidly wetted the hydrophilic conical needle, as shown in panel $e_7$ in **Fig. 19**(e). Inspired by the outstanding droplet collection capabilities on the alternate hydrophobic/hydrophilic micropatterns of desert beetle and the asymmetric microgeometry of cactus spines, Hu et al.[204] studied the droplet collection processes on the hybrid membrane with anisotropic wettability and asymmetric topology, where the hybrid membrane consisted of hydrophilic nanoneedle mesh and hydrophobic nanofiber network layer, as illustrated in **Fig. 19**(f-I). The condensed droplets were randomly formed on the hydrophobic poly nanofibers and hydrophilic nanoneedles, and the droplets were rapidly absorbed into the mesh due to the capillary force of the hydrophilic nanoneedles once the droplets contacted the hydrophilic nanoneedles. However, the neighboring condensed droplets on the hydrophobic poly nanofibers would continuously coalesce to form big droplets, and finally the big droplets would be absorbed and transported from the tip to the base of the hydrophilic nanoneedles, as shown in panels $f_1$ ～ $f_4$ in **Fig. 19**(f-II). The Laplace force at high curvature region was much larger than that at low curvature region, so that the Laplace force driven the droplets to transport towards the base of the hydrophilic nanoneedle, as shown in panels $f_5$ and $f_6$ in **Fig. 19**(f-II). The droplets are absorbed by the hydrophilic mesh and

then continuously excreted from the hybrid membrane showing excellent droplet collection capabilities.

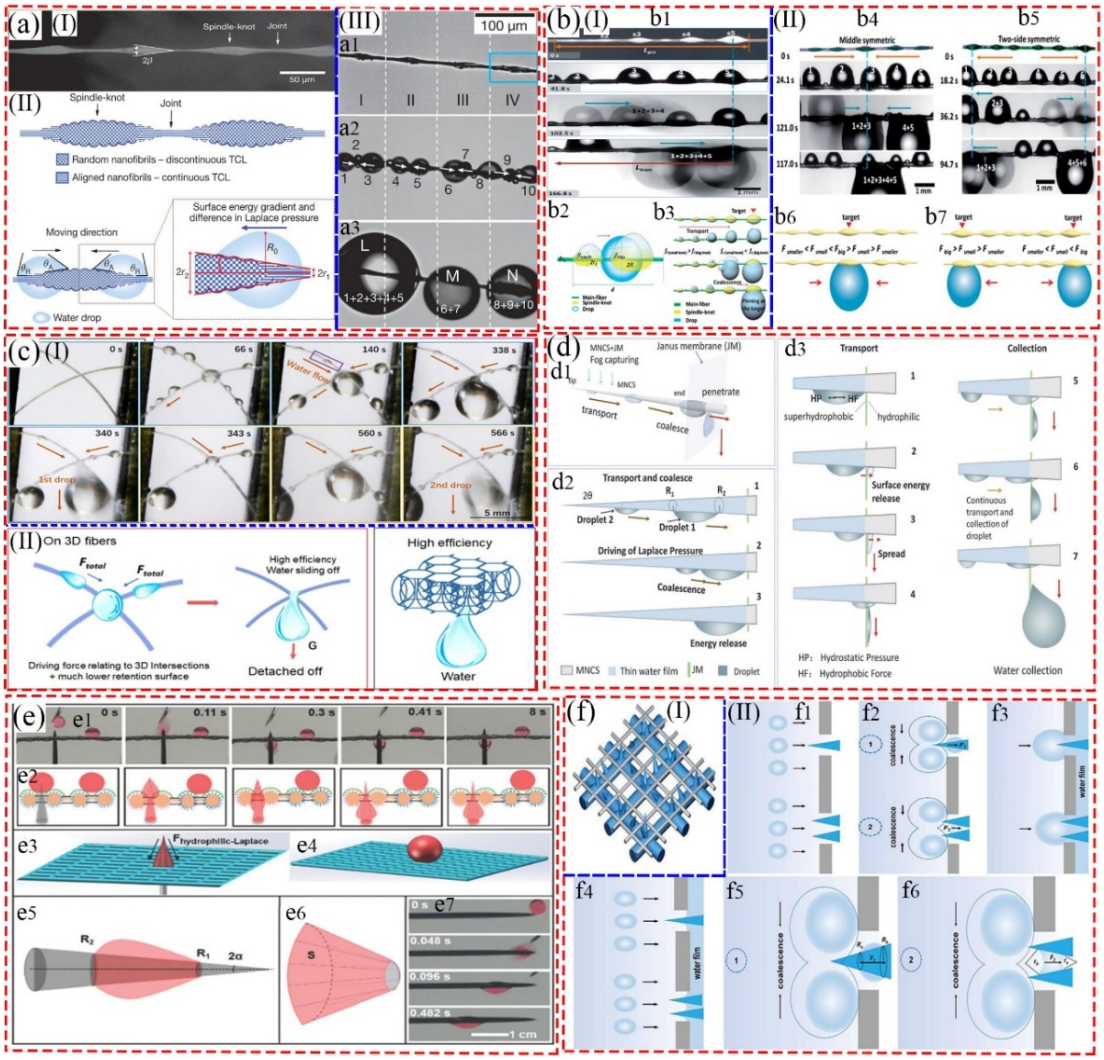


**Fig. 19. (a-I) The periodic spindle-knots linking with slender joints of spider silk; (a-II) Mechanism illustration of directional droplet collection on spider silk; (a-III) ESEM images of directional droplet collection on spider silk[98]. Copyright 2010 Nature Research; (b-I) Droplet coalescence and target transport on gradient step spindle-knot fibers; (b-II) Droplet transport and collection on gradient step spindle-knot fibers with middle symmetric and two-side symmetric gradient spindle-knots[149]. Copyright 2014 Royal Society of Chemistry; (c-I) Water droplet collection on the location of two crossing fibers of bioinspired nanocone-decorated three-dimensional fiber network (N3D); (c-II) Schematic of droplet collection and transport mechanism of N3D[153]. Copyright 2019 American Chemical Society; (d) Droplet coalescence, collection and transport on the micro/nanostructured conical spine and Janus membrane integrative system (MNCS+JM)[140]. Small 2018 Copyright; (e) Droplet dynamical behaviors on porous membrane with conical nanoneedles[211]. Copyright 2018 Royal Society of Chemistry; (f-I) The wettable hybrid membrane with nanoneedles; (f-II) The droplets growth, coalescence, transport and collection on hybrid membrane[204]. Copyright 2019 Royal Society of Chemistry.**

From the content and discussion presented within the above sections and quantitative summary of the droplet dynamics and control presented in Table 3, multi-gradient cooperation surfaces combining

chemical or structural wettability gradients with conical shapes inducing Laplace forces facilitate microscale droplet collection and directional transport, which is beneficial for accelerating droplet departure or sweeping. Droplet migration velocities in the order of millimeters/second have been reported for droplets on *flat* functionalized surfaces in the presence of Laplace pressure and wettability gradients[99] while velocities in the order of hundreds of millimeters/second have been observed on conical wires[136], i.e., in the presence of both wettability, structural and Laplace pressure gradients. The highest of the velocities reported in Table 3 is for the hemiwicking front during liquid transport in the work of Ghosh et al.[131] in the presence of a Laplace pressure gradient, though the rear of the droplet is not able to depin. In the case of complete droplet transport and in occasions in the presence of further microdroplet sweeping, this causes the enhancement of new refreshed areas in available for the next condensation cycle. The enhanced droplet self-removal empowering rapid shedding frequency multi-gradient cooperation surfaces has the potential to promote and enhance high condensation heat transfer performance when compared to the other surface categories, i.e., the wettability gradient surface, the Laplace gradient surface and the traditional homogeneous working surfaces.

**Table 3. Summary of droplet quantification dynamics on various surfaces with wettability and/or Laplace gradients.**

| References | Type of surface and/or structures | Droplet size/growth rate | Velocity/distance/frequency of migrating/shedding droplets | Rate of collection | Descriptions of the principle |
|---|---|---|---|---|---|
| Anand et al.[42] | Nanotextured SLIPS | Droplet diameter ranges from 100 μm to 1 mm | Velocity ~ 1 mm/s | ------ | Droplets float on the SLIPS and exhibit high mobility |
| Guo and Tang[108] | Microstructured hydrophilic and hydrophobic SLIPSs | Departure diameter ~220 μm hydrophilic SLIPS & ~326 μm hydrophobic SLIPS | Hydrophilic SLIPS is more effective in prompting droplet shedding. Values not reported. | ------ | Hydrophilicity favors droplet condensation owed to the lower heat transfer resistance |
| Wong et al.[45] | SLIPS | Droplet diameter > 2 mm | Droplet velocity is ~1.1 mm/s | ------ | Lubricant height gradient induces droplet self-propulsion |
| Zhu et al.[110] | SLIPS | Departure diameter ~ 1.72 mm | Droplet velocity is ~ 0.08 mm/s | ------ | Thermocapillary gradient drives droplet motion |
| Park et al.[99] and Yao et al.[178] | SLIPS with asymmetric bumps | 6.4 times greater droplet growth in the presence of asymmetric bumps | Asymmetric bumps accelerate droplets coalescence, sweeping and departure | > 30 ml/m$^2$ on symmetric bumps vs. < 5 ml/m$^2$ on flat | Capillary force, i.e., gradient force, drives droplet motion and accelerate coalescence |
| Kajiya et al.[156] | V-shape grooved SLIPS | ------ | Grooves accelerate droplets sweeping and departure | ------ | Shape gradient drives droplet movement |
| Dai et al.[114] | Hydrophilic and hydrophobic SLIPSs with microgrooves | ------ | Droplet shedding 3.3 vs 1.7 counts/mm$^3$/s hydrophilic vs. hydrophobic SLIPS | Fog harvesting ~351.2 mg/cm$^2$/h vs ~205.3 mg/cm$^2$/h | Directional microgrooves reduce pinning force and hydrophilic SLIPS facilitate condensation |
| Li et al.[181] | SLIPS with diverging channels | Droplet growth rate ~ 2 μm/s vs 0.2 μm/s on uninfused surfaces | Droplet migration distance > 400 μm within 10 s | ------ | Capillary force caused by diverging channel drives droplet motion |
| Xing et al.[126] | Multi-scale & multi-gradient copper wires | ------ | Droplet transportation distance is around 10mm | ------ | Chemical and structural wettability gradient enhances droplet transport |
| Ghosh et al.[131] | Wettability-patterned gradient surface | ------ | Liquid hemiwicking front velocity > 400 mm/s | Fluid transport rate ~ 350 μL/s | Wettability gradient drives liquid transport |
| Wu et al.[132] | Wettability-patterned gradients surface | ------ | Liquid migration distance is around 7.32 mm | ------ | Self-driven fluid transport is induced by the wettability gradient |

| References | Type of surface and/or structures | Droplet size/growth rate | Velocity/distance/frequency of migrating/shedding droplets | Rate of collection | Descriptions of the principle |
|---|---|---|---|---|---|
| Lin et al.[157] | Hierarchical wedge-shaped track patterns | ------ | ------ | Water collection ~ 467.3 mg/cm$^2$/h | Hierarchical wedge-shaped superhydrophilic tracks on hydrophobic background |
| Liu et al.[159] | Ultra-contrasting wettability venation network patterns | ------ | ------ | Water collection ~910.6 g/m$^2$/h | Venation wettability network induces self-driven transport and enhances water collection efficient |
| Ghosh et al.[142] | Wettability patterned surface | ------ | Liquid migration distance is ~ 2 mm | Volume flow rate is around 134 μL/s | Wettability patterns induce liquid transport and enhance condensation |
| Ju et al.[89] | Copper spines with gradient wettability | Droplet growth rate is 2.08 μL/s | Water transport velocity is around 20.05 μm/s | ------ | Combination of Laplace pressure and wettability gradient |
| Bai et al.[199] | Spine with hierarchical groove structures | ------ | Droplet transport velocity is around 360 μm/s | ------ | Laplace pressure gradient drives droplet directional transport |
| Ju et al.[86] | Multi-functional integrated spines | ------ | ------ | ------ | Laplace pressure, wettability gradient and multi-functionality integration |
| Xu et al.[136] | Heterogeneous conical wires | ------ | Droplet velocity is 116.7 mm/s | Fog collection rate is 0.36 mg/s | Combination of Laplace pressure and wettability gradient guarantees |
| Zheng et al.[98] | Multi-gradient synergy fibers | Micro-sized droplet | ------ | ------ | Laplace pressure and wettability gradient from joints to spindle-knots |
| Xue et al.[149] | Gradient-step fibers | Micro-sized droplet | Droplet velocity depends on its diameter, i.e., $V$=34.52$d^{-0.35}$ | Water collection ~509.4 μL/h | Laplace pressure and wettability gradient |
| Li et al.[153] | Multi-gradient 3D fiber network | Droplet growth rate is around 0.27 mm$^3$/s | ------ | Fog harvesting ~ 865.1 kg/m$^2$/day | Multi-gradient 3D nanocone-decorated fiber network |
| Zhou et al.[140] | Integrative Janus membrane and conical spine | ------ | Droplet migration ~ 21 mm | Water collection rate ~ 4.67 g/h | Wettability and Laplace pressure gradients |
| Wang et al.[211] | Porous membrane conical nanoneedles | ------ | The droplet velocity ~2.5 cm/s | ------ | Laplace pressure gradient and wettability gradient |

## 5. Heat transfer applications and condensate collection of bioinspired surfaces

Enhancing the condensation performance has a significant direct impact on phase-change heat transfer closely relevant to a wide range of energy-related applications. As conveyed in the Introduction Section, the realization of controllable droplet manipulation and transport during condensation phase-change plays a crucial role to achieve high efficient DWC heat transfer performance. Below we summarize the relevant investigations with focus on enhancing condensation heat transfer.

### 5.1 Condensation heat transfer performance on SLIPSs in absence of wettability gradients

The influence of droplet size distribution on heat transfer performance was investigated by Weisensee et al.[29] through experimental and numerical methods. Water droplets with critical nucleation radius ranging from 10 nm to 100 nm were randomly formed on SLIPSs. Droplets grew through direct condensation until its radius approached 10 μm, and then the droplets coalesced with neighboring droplets to form bigger ones. Finally, water droplets shed down the surface once the gravitational force of droplet overcame the hysteresis force (see Section 2.2 for more details on the forces acting on a droplet sitting on an inclined SLIPS) sweeping small-sized droplets on its path. Then droplets immediately re-nucleated on the refreshed area, as shown in shown in **Fig. 20**(a). The droplet overall thermal resistance comprising the interfacial thermal resistance at the droplet interface, conduction thermal resistance through the droplet and the thermal resistance of the surface played a crucial on the heat transfer performance during the condensation, as shown in **Fig. 20**(b). The conduction thermal resistance of droplet played a dominant role once the droplet radius was larger than 10 μm[29, 212]. Theoretical results showed that the individual droplet heat transfer flux increased with the increase of the droplet radius while the number density of the droplet nucleation decreased with the increase of the droplet radius, as a consequence of the increased droplet base area as illustrated in **Fig. 20**(c). The droplet number density versus droplet radius agreeing with the earlier correlation proposed by Rose and Glicksman[213] for hydrophobic surfaces was further demonstrated for SLIPSs in this work, which is presented in **Fig. 20**(d). More recently, Maeda et al. studied the effect of presence and absence of micro-structures on the droplet size distribution and on the heat transfer performance during condensation phase-change on SLIPSs[94]. In their work, they found that although the droplet size distribution shifts towards smaller sized droplets contributing to enhanced heat transfer performance in the presence of micro-structures, the additional heat transfer resistance imposed by the micro-structures and the oil in the order of tens of micro-meters contributed to the lower theoretical heat transfer coefficients reported. A fine balance between enhancing droplet shedding and the heat transfer resistance imposed by any additional structure was highlighted here. In a similar line of work, Ho et al.,

addressed the droplet size distribution and developed a heat transfer resistance based model for low surface tension fluids on SLIPS[214]. On a more applied framework, the role of infused lubricant on a SLIPSs condenser coupled with a superhydrophilic evaporator in enhancing thermosyphon heat transfer performance was studied by Zhang et al.[52]. The presence of a superhydrophilic evaporator was paramount on maintaining and excellent boiling and evaporation heat transfer performance as a consequence of the minimal contamination from the SLIPS condenser via the shedding of condensing droplet cloaked by the oil. The SLIPS condenser exhibited more than two-fold increase in condensation heat transfer coefficient due to the frequent droplet shedding and sweeping facilitating and enhancing the condensation cycles. The overall heat transfer performance of the thermosyphon with a SLIPS condenser coupled to a superhydrophilic evaporator was enhanced by about 28.9% when compared to a thermosiphon consisting of both pristine evaporator and condenser. The temperature distribution and heat transfer performance of the vertically placed gravitational thermosyphon with SLIPS condenser and superhydrophilic evaporator at various filling ratios were further investigated by Lv et al.[215]. The results showed that the axial temperatures of the SLIPS condenser of the thermosyphon exhibited decreasing tendency from bottom to top of the SLIPS condenser, which revealed that the condensation heat transfer performance at the bottom of the SLIPS condenser was much better than that at the top due to the re-nucleation acceleration at the bottom of the SLIPS condenser from the frequent sweeping of the condensed droplets. During the phase change process from vapor to water, a great amount of latent heat was released to the bottom of the SLIPS condenser, hence the temperature at the bottom of SLIPS condenser was larger than that at the top. The condensation heat transfer coefficient was improved due to the acceleration of droplet shedding from the SLIPS condenser while the overall thermosiphon heat transfer performance was also enhanced due to the reduction of the overall thermal resistance of the thermosiphon in the condenser's side.

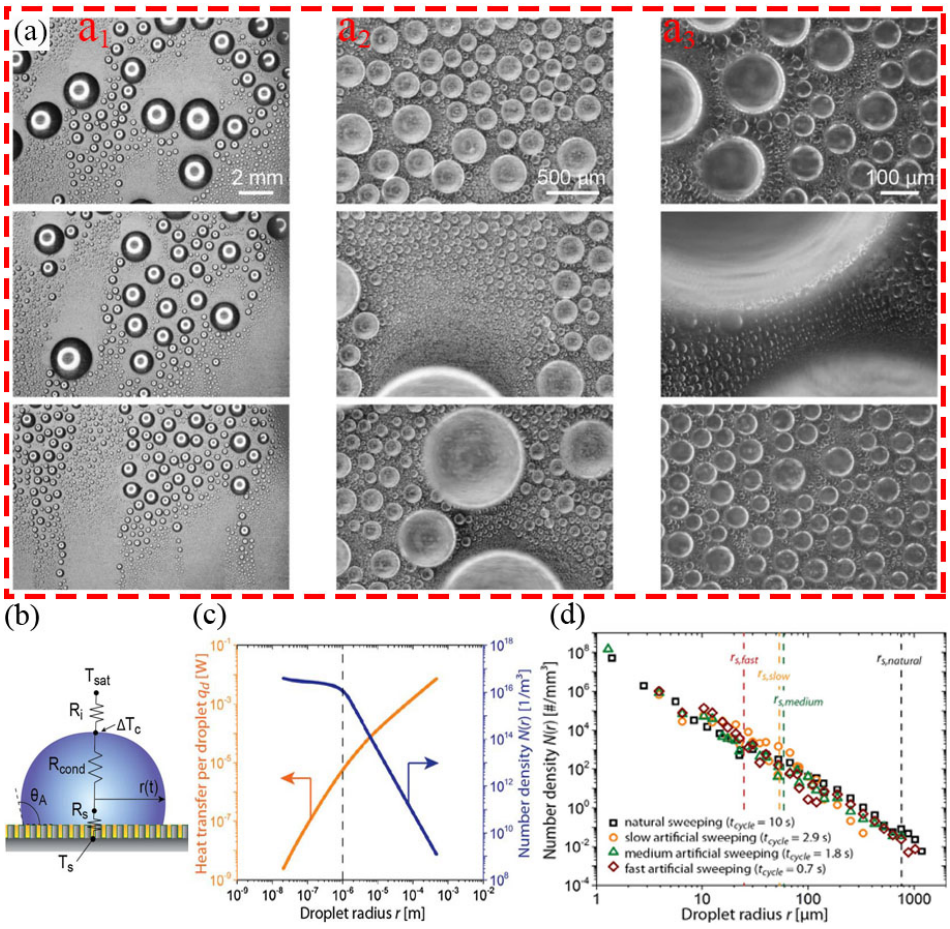


**Fig. 20. Droplet condensation and nucleation number density on SLIPS. (a) droplet condensation on SLIPS; (b) schematic of individual droplet thermal resistance; (c) numerical single droplet heat transfer flux and nucleation number density on SLIPS; (d) experimental measured nucleation number density[29]. Copyright 2017 Elsevier.**

Sirohia and Dai[182] theoretically investigated the heat transfer and the heat transfer coefficient of hydrophilic SLIPSs. Theoretical results showed that the condensation heat transfer coefficient increased with the decrease of contact angle as a consequence of the decreased droplet thickness, i.e., decreased the droplet heat transfer resistance, when compared to hydrophobic SLIPSs. Moreover the smaller contact angle hysteresis reported on roughened SLIPSs when compared to smooth SLIPSs could significantly enhance the droplet shedding ability and the condensation heat transfer coefficient. The condensation heat transfer coefficient of flat SLIPSs was 172.5 kW/(m$^2$K), which was 286.0% higher than that of flat hydrophobic surface and 174.0% larger than that of SHS, as illustrated in **Fig. 21**(a). The condensation heat transfer coefficient of SLIPS with rough structures was 191.3% larger than that of flat SLIPS because the roughness accelerated the droplet removal from the SLIPS[42]. The heat transfer performance on hydrophilic SLIPS was additionally investigated by Guo and Tang[108], where the merits of both efficient nucleation and rapid droplet departure of hydrophilic SLIPSs were integrated. The droplet nucleation energy barrier on

hydrophilic SLIPS was much lower than those on hydrophobic surfaces, SHSs and hydrophobic SLIPSs. **Fig. 21**(b) shows that the condensation heat transfer coefficient on pristine copper surface was the lowest compared to the other surfaces due to the large thermal resistance of the flooded liquid film when compared to DWC ensuing on all other four surfaces. The condensation heat transfer coefficients of SHS, hydrophobic surface, hydrophobic SLIPS and hydrophilic SLIPS increased respectively, regardless of the subcooling degree, as shown in **Fig. 21**(b). The condensation heat transfer coefficient on hydrophilic SLIPS was improved by 2.2%-18.9% when compared to hydrophobic SLIPS for subcooling conditions ranging from 24 K to 2 K, respectively. Differences on the condensation heat transfer coefficient when comparing hydrophobic and hydrophilic SLIPSs increased with the decrease of subcooling degree because droplet nucleation on hydrophobic SLIPSs was inhibited more obviously under small subcooling degree when compared to hydrophilic SLIPSs. The condensation heat transfer performance on SLIPS tubes was investigated by Xiao et al.[27], where the SLIPS was prepared by infusing the Krytox oil into the TFTS coated nanostructured surface. Droplets with large departure diameter inhibited condensation heat transfer performance because the droplet cannot be quickly removed from the surface, as shown in panel $c_1$ in **Fig. 21**(c). On hydrophobic SLIPSs though the theoretical heat transfer coefficient was found to decrease with the increase of contact angle due to the large thermal resistance imposed by the thickness of the droplet, as illustrated in panel $c_2$ in **Fig. 21**(c), and due to the reduced droplet nucleation density as shown in panel $c_3$ in **Fig. 21**(c). All three surfaces hydrophobic, SHS and SLIPS investigated showed an increased condensation heat transfer coefficient with the increase of vapor pressure at low subcooling degree because large amount of molecules available for condensation[138] as illustrated in **Fig. 21**(d). It also can be seen from **Fig. 21**(d) that the condensation heat transfer coefficients of SHS, hydrophobic surface and SLIPS increased sequentially, regardless of vapor pressure, because the droplet departure diameters on both hydrophobic surfaces and SHSs were larger than that on SLIPSs.

The influence of non-condensable gases on heat transfer performance of SLIPSs was studied by Preston et al.[31]. Experimental results showed that the condensation heat flux of pristine copper surface, hydrophobic surface and SLIPS increased respectively in the absence of non-condensable gases regardless of the subcooling degree. Their work demonstrated the better heat transfer performance of SLIPS compared to the hydrophobic and pristine surfaces by 30% and 400% respectively as shown in **Fig. 21**(e). However, the condensation heat flux of SLIPS was dramatically reduced in the presence of the non-condensable gases as small as 50 Pa, as illustrated in **Fig. 21**(e). This additionally demonstrated the paramount role non-condensable gasses preventing the transport of water vapor molecules towards the condensate, which

significantly inhibits the condensation heat transfer. The condensation heat transfer enhancement on SLIPS tubes was investigated by Tsuchiya et al.[216]. Results showed that stable DWC could be maintained on the SLIPS tube during the condensation process, and the condensation heat transfer coefficient of SLIPS tube was 175% higher compared to the pristine tube. The condensation heat transfer coefficient of the SLIPS tube with low viscosity lubricant was higher than that of SLIPS tube with high viscosity lubricant because of the faster droplet shedding ability of in the presence of a low viscosity lubricant.

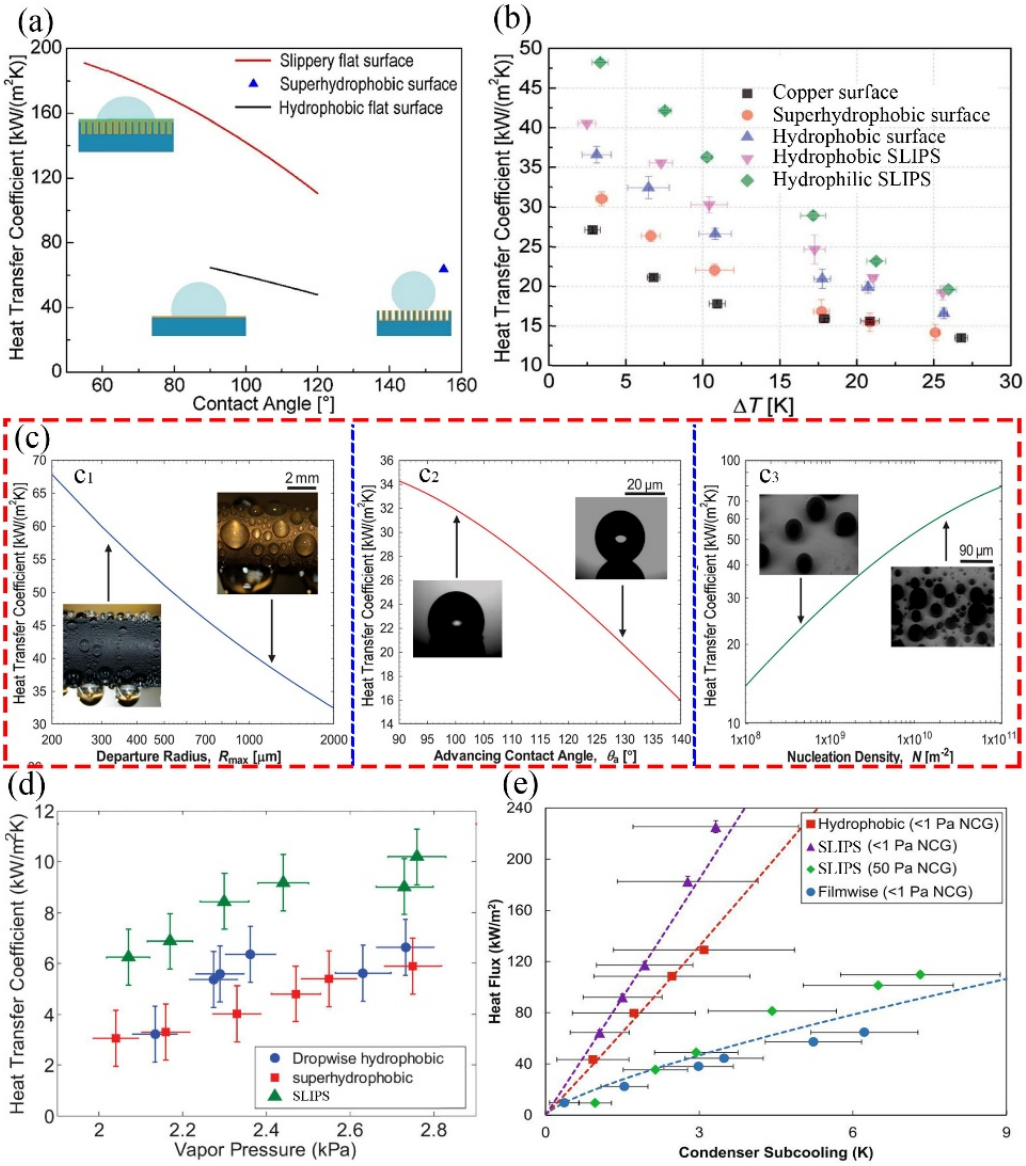


**Fig. 21. Condensation heat transfer coefficients on various surfaces. (a) Theoretical heat transfer coefficients on flat SLIPS, SHS and hydrophobic flat surface[182]. Copyright 2019 Elsevier; (b) condensation heat transfer performances on copper surface, SHS, hydrophobic surface, hydrophobic SLIPS and hydrophilic SLIPS[108]. Copyright 2018 Royal Society of Chemistry; (c) the influences of departure radius, advancing contact angle and nucleation density on condensation heat transfer coefficient; (d) comparison of condensation heat transfer coefficients on hydrophobic surface, TFTS coated SHS and oil impregnated composite surface[27]. Copyright 2013 Nature Research; (e) the relationship between condensation heat flux and subcooling degree, the experimental results denoted as points, the model predictions presented as dashed lines, the NCG denoted the non-condensable gas[31]. Copyright 2018 Nature Research.**

The first continuous DWC of low surface tension fluids such as ethanol and hexane on nanostructured SLIPS tubes was demonstrated by Sett et al.[30]. The logarithmic mean vapor to liquid temperature difference, namely $\Delta T_{LMTD}$, increased with the increase of condensation heat flux for both ethanol and hexane with greater $\Delta T_{LMTD}$ reported at a constant heat flux on the hydrophobic tube due to the flooded film acting as the dominant thermal resistance as shown in **Fig. 22**(a-I). The condensation heat transfer coefficients of the hydrophobic tube were then much lower than those of three SLIPS tubes varying in the infused lubricant for both ethanol and hexane and gradually increased with the increase of vapor pressure as illustrated in **Fig. 22**(a-II). The thickness of the liquid film and hence the thermal resistance grew as the vapor pressure increased and inhibited the condensation heat transfer performance. The condensation of both ethanol and hexane on three SLIPS tubes exhibited DWC behavior. The heat transfer coefficient enhancement of three SLIPS tubes showed similar trend for ethanol and hexane condensation and became more obvious with the increase in vapor pressure as shown in **Fig. 22**(a-II). However, the heat transfer coefficient discrepancies of hexane condensation on three SLIPS tubes were larger than those of ethanol condensation as it can be seen in **Fig. 22**(a-II). The advancing contact angles for ethanol and hexane on three SLIPSs were 62.4°−71.1° and 37.4°−45.7°, respectively, which revealed that the heat transfer coefficient discrepancy depended on the advancing contact angle[27], i.e., the small range in advancing contact angle of ethanol meant a narrow range of heat transfer coefficient, and the large variance in advancing contact angle of hexane meant a large heat transfer coefficient discrepancy. The heat transfer coefficients of ethanol condensation on three SLIPS tubes were smaller than those of hexane condensation, and the averaged DWC heat transfer coefficients for ethanol and hexane on three SLIPS tubes were 6.2 kW/(m$^2$K) and 9.4 kW/(m$^2$K), respectively, which was attributed to the larger advancing contact angle of ethanol compared to hexane on all three SLIPSs. The small contact angle meant large contact area between condensed hexane and SLIPS tube and lower droplet thickness thereby reducing the thermal resistance through the droplet and enhancing heat transfer performance[27].

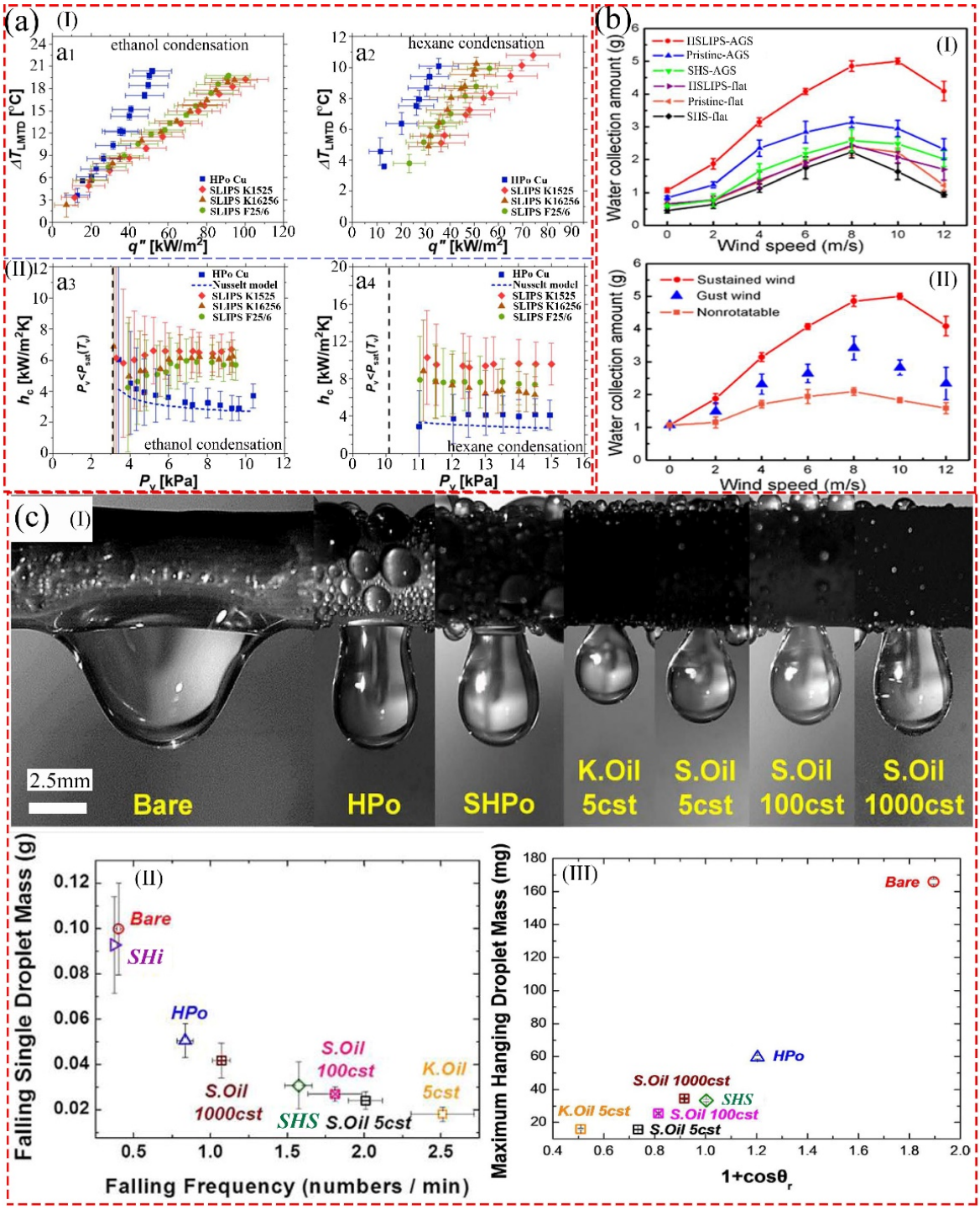


**Fig. 22. Condensation heat transfer characteristics and droplet collection on various surfaces. (a-I) the relationship between logarithmic mean water to vapor temperature difference ($\Delta T_{LMTD}$) and overall heat flux; (a-II) experimental and theoretical condensation heat transfer coefficient ($h_c$) as a function of saturated vapor pressure ($P_v$)[30]. Copyright 2019 American Chemical Society (b-I) comparison of the water collection performance of the HSLIPS-AGS windmill with the increasing of wind speed over 5 min, the pristine-AGS, SHS-AGS, HSLIPS-flat, pristine flat and SHS-flat windmills acted as references; (b-II) water collection performance of the HSLIPS-AGS windmill under a sustained wind and gust wind for 5 min, the nonrotatable HSLIPS-AGS windmill was used as a reference for comparison[162]. Copyright 2019 American Chemical Society; (c-I) the sequence images of hanging droplet dripping process on various tubes; (c-II) the average mass and frequency of the single falling droplet during the condensation process; (c-III) the measured maximum hanging droplet mass as a function of 1+cos$\theta_r$[111]. Copyright 2016 Nature Research.**

### 5.2 Condensate collection on functional structured SLIPS in presence of wettability gradients

Condensate directional transport and efficient collection can obviously accelerate the droplet departure from the surface and improve the droplet sweeping frequency, which can significantly enhance the condensation heat transfer performance. The droplet condensation performance of windmill in complex windy environments was studied by Wang et al.[162], where the blade surface of the windmill integrated the ridge-like wall with a shape gradient and modification layer. The droplets randomly nucleated on the anisotropic grooved surface, and then the droplets on the top of the ridges grew faster than those in the valleys of the grooved surface due to the curvature surface of the ridge[99, 217]. The Laplace force arising from the shape gradient of the ridge driven the droplets continuously sliding into the valleys, and finally the big droplets shed from the blade surface of the windmill. When the wind speed was below 10 m/s, the droplet collection amount increased with the increase of wind speed, and then it declined once the wind speed exceeded 10 m/s, as shown in **Fig. 22**(b-I). The droplet collection efficient reduced due to the severe loss of water droplets through windmill at high wind speed. The droplet collection efficiency on hydrophilic SLIPS anisotropic grooved surface (HSLIPS-AGS) was much better than those on the other five kinds of surfaces, as illustrated in **Fig. 22**(b-I), which revealed that the combination of the SLIPS and the grooved surface accelerated the removal of condensed droplets. It can be seen from the **Fig. 22**(b-II) that the droplet collection efficiency of the HSLIPS-AGS windmill under the sustained wind was higher than that under the gust of wind, and the droplet collection efficiency of the non-rotatable windmill was the lowest in the three cases. The results revealed that the HSLIPS-AGS windmill exhibited better droplet collection capability in the complex windy environments compared with the other windmill. The droplet removal efficient on the SLIPS tube was investigated by Seo et al.[111], where the SLIPS tubes were prepared by infusing the silicone oils with various viscosity into the superhydrophobic tubes. The condensed droplets were transported from the top and side to the bottom of the tube to form a hanging big droplet underneath the tube. Finally, the hanging big droplet dropped from the tube once its gravitational force exceeded the capillary adhesion force, as shown in **Fig. 22**(c-I). The dynamic dripping process of the hanging big droplet was much slower compared to the droplet transport process, which meant that the hanging big droplet dripping from the bottom of the tube govern the droplet removal efficiency of the tube and further affected the condensation heat transfer performance. The force balance between the gravitational force and capillary adhesion force of hanging big droplet could be simply expressed as $\rho gV \sim \pi D_c \gamma(1+cos\theta_r)$, where $\rho$, $g$ and $V$ were water density, gravitational constant and hanging droplet volume, respectively, and $D_c$, $\gamma$ and $\theta_r$ were

contact diameter, surface tension of water and receding contact angle, respectively. It can be seen from **Fig. 22**(c-I) that the hanging droplet of SLIPS tube with low viscosity lubricant was smaller than those of SLIPS tubes with high viscosity lubricant, which revealed that droplet removal efficiency of the SLIPS tube with low viscosity lubricant was much better compared with other tubes. The shedding frequency of the handing droplets removal from the SLIPS tubes was improved as the increasing of lubricant viscosity, and meanwhile the single falling droplet mass decreased with the increase of shedding frequency, as shown in **Fig. 22**(c-II). The maximum mass of the hanging droplet on the SLIPS tubes with the lubricant viscosity of 5 cSt, namely 5 cSt Krytox oil and 5 cSt silicone oil, was much smaller than those on other SLIPS tubes due to the largest receding contact angle, as illustrated **Fig. 22**(c-III), which revealed that the SLIPS tubes with the lubricant viscosity of 5 cSt exhibited the best droplet removal efficiency and condensation heat transfer performance.

The DWC is realized on the SLIPSs in practical applications, where the SLIPS facilitates the droplet easily departure from the surface and accelerates the re-nucleation and growth of droplets. The physicochemical properties of SLIPS play a crucial role for the droplet nucleation process, i.e., the droplets are easily nucleated on the hydrophilic surface which has low nucleation energy barrier, and the structural gradient of the surface facilitates microscale droplet gather together and directional transport, and finally the condensation heat transfer performance is significantly enhanced, which is beneficial for the thermal management in practical applications. Nonetheless, the mobility and stability of the oil phase as well as that of the coating and/or the structures poses a real challenge to their implementation in real industrial applications, which will be introduced and discussed in the next subsection. Nonetheless, the mobility and stability of the oil phase as well as that of the coating and/or the structures poses a real challenge to their implementation in real industrial applications, which will be introduced and discussed in the next subsection.

### 5.3 Mechanical and chemical stability and durability of SLIPS and wettability gradient SLIPS

The intimate binary interactions between the solid surface, the oil and the condensate play a paramount role on one of the main drawbacks of SLIPS related to the stability of the lubricant impregnated within the porous structures, which tends to deplete from the surface due to gravity and/or carried out by the condensate either via cloaking or condensate-oil miscibility. In the particular case of SLIPS, the low adhesion properties of these surfaces can be compromised by the low affinity of the oil to the structured surface, which can eventually cause the oil depletion from the surface and loss of slippery properties with the consequent undesired enhanced droplet/liquid adhesion. In this case, the length scale of the surface

structures interlocking the oil in between them play a crucial role. The extent of the hierarchical length scale on the stability of the lubricant was addressed to some extent by Kim et al. where a hierarchical micro-/nano-structured SLIPS was compared to a one-tier nano-structured SLIPS[218]. It was found that the one-tier nano-structured SLIPS exhibited better stability when compared to micro-/nano-structured SLIPS. This was attributed to the preferential depletion of the oil from the micro-structure tips leaving the top of the structures exposed to the liquid with the consequent enhanced adhesion. On a more applied note, Wong et al. further demonstrated the importance of interspacing between structures[219]. In their work, analogous findings to those reported by Kim et al. were envisaged where the depletion of the lubricant occurs for micro-SLIPS with interspacing greater than the size of the dendrites during frosting. While on the other hand constraining the interspacing between nano-structures and the oil locked within the structures to 30 nm or below (in the absence of micro-features) provided negligible lubricant depletion during condensation and freezing. Though these works do not address the effect of nano-structure interspacing explicitly, they point out to the need of having close structure interspacing for the long term stability of the lubricant within the structures.

In addition to the importance of surface structure locking the lubricant by capillary action; lubricant volatility, thermal stability, as well as liquid-lubricant and/or lubricant-coating/surface compatibility and affinity to low-surface energy hydrophobic materials are of paramount importance as well. To this end, the works of Preston et al. and Sett et al. on the design of lubricant infused surfaces and on the extent of lubricant miscibility and the interactions between low-surface tension fluids and a wide range of lubricants are of interest[112, 220, 221]. The former, the work of Preston et al., provides a very detailed predictive model for the system droplet-lubricant-SLIPS taking into account a geometric factor $R$ (defined as $R = (r-1)/(r-\varphi)$ where $r$ is the actual roughness of the solid surface and $\varphi$ the solid fraction) and the different binary surface tensions present in the system accounting for polar and non-polar binary interactions between all four phases[112]. The proposed design model was validated via experimental observations of the same authors and those of others. Further they demonstrated the feasibility of SLIPS on uncoated high-surface energy solids, which by-pass the requirement for low-surface energy coatings and the coating stability considerations. In addition to the work of Preston et al., the two works of Sett et al. with focus on the liquid-lubricant stability or miscibility also provide a very important framework on the pairs working fluids-lubricant that are viable for the final application[220],[221]. In their work both the extent of miscibility and cloaking were evaluated as both phenomena are undesired. On the one hand, the miscibility of the working fluid with the lubricant causes the change in physicochemical properties of the

lubricant modifying the lubricant-surface interactions and eventually the loose of affinity between them[220]. On the other hand, the occurrence of cloaking over the working fluid potentially leads towards oil depletion as shedding droplets will carry the oil away from the surface. In their latest work a model predicting the SLIPS lifetime function of the working fluid and SLIPS and the surface heat flux was introduced, which is of extreme usefulness for the final design of the real application[221]. In addition, the high viscosity and lubricant spreading coefficient less than zero are more beneficial for maintaining the lubricate oil locked within the structures during the condensation process[95, 172, 222]. A more recent review encompassing both the length scales as well as the multiscale spatial dimensionality from 0D to 3D is found in the work of Sheng et al.[223]. Different solid–liquid host–guest composites and solid-liquid interactions considering structures as the solid host matrix such as membranes, aerogels, fibers, etc. and infused lubricants such as Kryotx, silicon oil, phase change materials and liquid metals are reviewed and provided. For example they report on the good stability of composite textile (solid) filled with biocompatible phase-change material (liquid/solid).

In the case of advanced functional SLIPSs, surface stability and durability are not only related to the lubricant-surface affinity and to the viscosity and spreading coefficient of the lubricate oil, but also closely related to the mechanical strength of the microscale and/or nanoscale structures of the functional surfaces. In the case of both functional advanced surfaces, with and without oil impregnation, mechanical failure of the structures as well as that of the coating poses one of the biggest challenge there is hindering the successful implementation of these surfaces in real industrial applications. Although the lubricant oil has been reported to act as a protective layer with self-healing properties[45] towards corrosion[224], environmental abrasion[225] and/or malfunction of the protective coating, both the coating as well as the micro- and/or nano-structures can be highly damaged by mechanical abrasion and/or stresses. The damage or pilling off of the SLIPS multi-level structures, i.e., micro-, nano- and micro-/nano- structures, and/or of the multi-level gradients, and/or the coating anticipates the more affinity of solid surface to the condensate rather than to the oil and the expected loose of low adhesion with occurrence of large pinned condensing droplets. To this end, very few works focus on addressing the mechanical stability of advanced solid surfaces. A very promising approach towards ensuring the robustness and mechanical durability even after 100s of cycles is the use micro-hills[205] or inverted micro-pyramid cavities[226], which act as sacrificial features protecting the rest of the functional surface including the lower tiers of roughness, the coating and the lubricant impregnated within. Nonetheless, although in the work of Wang et al.[226] the robustness of their surface was demonstrated by the no apparent fracture of the electroplated nickel-PTFE surface even

after 300 cycles and no loss of hydrophobicity (as apparent contact angles were all in the superhydrophobic range) even after 1,000 cycles, the practicability of theses armored surfaces towards more applied phenomena such as condensation phase-change were not demonstrated[226]. A different approach aiming to improve the mechanical robustness of the surfaces is to lock the hydrophobic coating within a metallic framework, which can enhance the stability of the coating and that of the solid surface with the additional benefit of improving the overall heat transfer resistance when compared to bare coating of the same thickness[227, 228]. It is worth noting that in closed systems such as loop heat pipes or closed loop thermosiphons, the stability to mechanical abrasion is less of an issue; though the stability of the lubricant as well as the long term stability of the coating still need to be addressed and must be tailored so to ensure the low adhesion and slippery nature of the condenser with the consequent stable heat transfer performance over time. To this end, Zhang et al. and Lv et al. have demonstrated the continuous operation of a closed loop thermosiphon comprising a superhydrophilic evaporator and a SLIPS condenser for over 200 hours without degradation of its heat transfer performance[52, 215].

To sum up, the physical, physicochemical and chemical stability and durability of the impregnated lubricant, the coating and the surface structures are conducive to extending surface durability and maintaining efficient condensation performance for long periods of time as well as to improving the self-healing performance of the functional SLIPSs. High mechanical strength can prevent the structures from being damaged, which is more favorable for fixation of the lubricant oil and further improving the surface durability. At present, the physical interaction between the lubricant oil and the micro- and/or nano-structures and the mechanical strength of the surface structures are two key factors affecting the durability performance of SLIPSs. And there is much need for the systematic, comprehensive and in-depth investigations by researchers so to gradually solve these key problems setting the foundation for the wide application of functional surfaces.

# 6. Summary, Outlook and Future Perspective

## 6.1 Summary and Outlook

In this review, recent developments and advancements on wettability gradient surfaces, SLIPSs and wettability gradient SLIPSs with focus on droplet mobility and fluid transport enhancement have been systematically introduced, analyzed and discussed. The unique cooperation of wettability gradient and low adhesion SLIPSs represents an enormous potential for condensation heat transfer, microfluidcs and related droplet transport applications. This is supported and demonstrated by looking into the fundamental theory governing wetting on traditional surfaces and spontaneous droplet transport in the presence of a chemical and/or structural wettability gradients. The different binary interactions governing the droplet-surface interactions on traditional surfaces as well as on SLIPSs and on wettability gradient SLIPSs have been carefully introduced. The theory introduced demonstrates that for effective droplet transport both via wetting driving force or via Laplace pressure difference, the driving force needs to overcome hysteresis, which as presented throughout is minimized on SLIPSs.

Coupling the merits of low adhesion SLIPSs to wettability gradient structured surfaces promises on facilitating droplet re-nucleation, growth, coalescence and shedding periodically with enhanced droplet transport during condensation phase-change. Though from the fundamental and small-scale applied points of view the means for imposing a wettability gradient and/or Laplace pressure gradient on bioinspired functional SLIPSs are several and readily available, which have been also described in detail, the large scale fabrication and bulk manufacturing of multi-scale/gradient surfaces and SLIPS poses a technical and applied challenge. The fabrication process/es of homogeneous, structured, SLIPSs and bioinspired gradient structured SLIPSs have also been thoroughly reviewed and introduced. Clear differences are noted when looking into the fabrication of surfaces comprising either a chemical or a structural a wettability gradient or in the presence of a multi-gradient cooperation coupled with a SLIPS as a consequence of the additional step necessary to induce the needful gradient. The wide range of fabrication materials vary from traditional metals such as copper, aluminum, stainless steel, etc. followed by mechanical punching, laser processing or chemical etching being this latter more common as allows for the easy and scalable fabrication of high thermal conductivity materials of importance to thermal transport. In addition, other less conductive materials such as polymers (PDMS, PET, nylon fiber, etc.) have also been recently utilized following replica molding or plasma etching and are acquiring relevant importance as per their versatility and easiness on reproducing surface structures. Although, scalable manufacturing of multi-level micro-structures and micro-structural gradients can be easily realized on metal substrate by means of laser-texturing and

mechanical machining or punching, some of these approaches are not applicable to non-metallic substrates, which can show brittleness and fracture when applying mechanical stresses and/or high temperatures. When looking into nano-structuring chemical etching and thermal growth can be, to some extent, applied to large areas, followed by via dip coating or vapor deposition for the implementation of the coating at large scales. Nonetheless, to date, for the creation of both micro- and nano-structures a two-step approach with a third one for the coating application and the final impregnation of the coating is/are required. The need for a third tier of roughness may require an additional mechanical or chemical step, which creates additional complications for scalable manufacturing. This renders the scalability of metal surfaces more accessible than that of non-metallic substrates and/or the combination of a metal background with the deposition of non-metallic materials where their adhesion may be compromised. An example on this latter is electrospinning method is also gaining importance as per its ability to deposit and create fiber density gradients beneficial for droplet transport. Although the adhesion of the fiber to the main surface may be compromised while at the same time the thermal conductivity of such polymer materials or fibers are rather undesirable for heat transfer applications.

Condensation on uniformly structured SLIPSs introduced within the past decade has been of paramount importance on the advancement of the fundamental understanding of the intimate interactions in a system surface-lubricant-condensate-air. Both micro-, nano- and micro-/nano- structured SLIPSs, hydrophilic and hydrophobic SLIPSs, the type of lubricant as ionic liquid or oil, which may or may not cloak the droplets and/or suppress condensate coalescence have been thoroughly designed, fabricated and characterized recently. The better droplet mobility and heat transfer performance of SLIPSs when compared to traditional hydrophobic and/or SHSs have been demonstrated. To highlight is the higher droplet density, coalescence rate and shedding frequency of condensing droplets, which in turn shall provide greater heat transfer coefficients on hydrophilic SLIPSs when compared to hydrophobic SLIPSs. Further the condensate droplet self-propulsion confined within the meniscus near the surface-condensate-oil triple contact line may also be exploited to enhance the droplet growth via both direct condensation and droplet coalescence so to reach the critical shedding size sooner. Millimeter scale patterns have also proven to enhance the condensate flux with greater enhancements for bump patterns with smaller radius of curvature, while V-shaped grooved surfaces help to constrain the growth of the condensate in the direction of the grooves creating cylindrical droplet chains that shed from the surface after a coalescence event.

Constraining the droplet geometry or the condensate flux over certain surface regions is of interest and has demonstrated enhanced condensate shedding performance; nonetheless, these surfaces lack on the

control of the droplet transport. In order to achieve directional droplet transport, chemically or structured patterned surfaces where the wettability gradient imposed overcomes droplet adhesion have been recently implemented making use of wires, superhydrophilic-superhydrophobic wedges or stripes, superhydrophilic channels on superhydrophobic background, as well as conical spines and/or grooved structures and/or multi-gradient cooperation advance functional surfaces combining chemical or structural wettability gradients with conical shapes favoring Laplace pressure gradients forces, i.e., multi-gradient cooperation, inducing controlled droplet transport, etc. have been proposed. Of interest is the droplet dynamic behavior on dendrite aequilate superhydrophilic-superhydrophobic patterned surface where different axisymmetric channels guide the condensate to the regions of interest or reservoir. The use of conical spines introducing the additional Laplace pressure gradient between the front and rear edges of the droplets have also been implemented on a 2D wettability gradient SLIPSs with the consequent additional potential to enhance the surface collecting area and the amount of condensate by implementing them on a 2D configuration, i.e., multi-gradient cooperation. The occurrence of DWC and enhanced droplet mobility for a wide range of surface tension fluids on uniform SLIPSs has demonstrated to provide greater heat transfer coefficients, while the potential implementation of wettability gradients inducing additional directional droplet transport may in turn enhanced droplet shedding and heat transfer when compared to uniform SLIPSs.

To conclude, in this timely review we have summarized recent advances on both SLIPSs and wettability gradient surfaces narrowing down to the opportunities and challenges on the synergistic cooperation of wettability gradient surfaces and SLIPSs as promising candidates for heat transfer applications. SLIPS and/or bioinspired gradient structured SLIPS widely used in the vapor to liquid phase change related industrial processes, e.g., using SLIPS to accelerate the droplet removal from the condensing surface further enhancing condensation heat transfer performance, can be effectively promoted by using bioinspired gradient structured surface impregnated with a lubricant, i.e., gradient structured SLIPSs, so to facilitate directional transport and hence droplet collection. Although the vapor condensation on SLIPSs and/or bioinspired gradient structured SLIPSs has been widely investigated in recent years, it is obvious that the further investigations are still desired in both fundamental and application aspects. The use of SLIPSs coupled with bioinspired gradient structures is still in its infancy as per the handful of relevant works introduced here. Nonetheless, it is then clear that the combination and synergistic cooperation of chemical and structural gradients and low adhesion plays a positive and unique role for sustainable and efficient droplet transport, microfluidics as well as thermal and energy management with focus on condensation heat transfer performance enhancement.

## 6.2 Future Perspective

The field of SLIPS and wettability gradient surfaces is still in its infancy with the first SLIPSs being proposed a decade ago in 2011, with the first works coupling wettability gradient surfaces and SLIPS shortly after. Although the first effective motion of a droplet owed to a gradient of wettability dates almost 3 decades back, the exploitation of this phenomenon within every day and industrial applications is scarce. This is due to the complexity on creating long-term durable coatings or coatings that can withstand current manufacturing processes, a challenge which is shared with many other research groups, disciplines and industries from surface science, to biomedical, aeronautics, engineering and/or heat transfer. This is even a greater challenge when surfaces share an interface between the different deposited coatings as they are prone to delamination triggering eventual failure. So efforts from the different communities on addressing the long term stability of the coatings, in the order of decades, is of much need. To this end, mechanically texturing a gradient on a solid surface in the absence of a chemical coating, which can be achieved via laser processing, mechanical machining or mechanical punching, is another promising route for creating long-term surfaces. Although the introduction of more than one-tier of roughness may result problematic, challenging and costing. Special attention needs to be paid to the search for lubricant-solid compatible materials in which the intrinsic solid has not been coated and the intrinsic wettability of the solid has better affinity to the oil than the working fluid.

When looking into the additional contribution of wettability gradients to enhance droplet mobility and motion, the fastest droplet motion and the largest migration distances have been reported on conical wires comprising both chemical, structural and Laplace pressure gradient. Nonetheless, their applicability for condensation heat transfer is still debatable as per the small surface area of the wires and hence the low heat transfer removal. The introduction of Laplace pressure gradients via surface structure on a planar surface showing the greatest droplet bulge front velocities can also be of interest, though the bulge of liquid left behind on the rear of the migrating droplets do not offer the refreshed area for droplet re-nucleation and growth expected from high heat transfer condensation surfaces. Having a patterned wettability surface comprising a hydrophilic SLIPS region were droplets continuously nucleate, growth and detach coupled to a hydrophilic channel exploiting a Laplace pressure gradient were the condensing droplets from the hydrophobic region swept are quickly swept and transported away to the bulk condensate is a promising combination. Several advantages can be highlighted in this system such as the low thermal resistance of the condensing droplets on hydrophilic SLIPS coupled to the quicker they are able to reach and being swept

into the liquid film when compared to droplets on a hydrophobic or superhydrophobic surface, as well as exploiting the thermocapillary induced motion as a consequence of the different heat transfer undergoing within the different patterned wettability regions. This latter systems may couple both structural, chemical and Laplace pressure gradients with the further occurrence of a self-generated thermal gradient. In addition, the incorporation of spines may further increase the surface area of the surface, which may result of interest, though here there are additional fabrication steps and the mechanical stability may be compromised. The different mechanisms must be carefully scrutinized along with the difficulty and reliability of the manufacturing techniques and processes, about all during additive manufacturing or bulk manufacturing.

To conclude, further collaboration and synergistic cooperation between the different multidisciplinary and interdisciplinary areas where knowledge from material science, mechanical engineering, additive manufacturing and other engineering disciplines are required for the large scale production of the solid structured surface; chemistry, chemical engineering, physicalchemistry as well as material science are needed for the further implementation of surface nano-structures and/or stable and durable coatings; physics, fluid mechanics and fluid dynamics are of interest for the better fundamental understanding and further optimization and exploitation of the phenomena; as well as engineers at both academic and industrial levels so to ensure the applicability and long-term durability of the systems; must be ensured. Further a more homogeneous approach throughout both fundamental and applied studies adopting a common methodology to report the relevant findings so that these are easily and readily comparable is of much need. Last, despite the great deal of fundamental research in the topic carried out in the past 10 years, more efforts from the scientific community must be placed on the applied side including accurate and precise heat transfer measurements of such systems as well as the study of the long-term durability of the structures, the coatings and the lubricant impregnated depending on the system; as the lifetime of industrial condensers and real applications is expected to be > 10 years. In addition, a techno/economic as well as cost/benefit analysis and careful consideration to the best available technology (BAT) should be carried out.

## Acknowledgments

F. Y. Lv acknowledges the support from Natural Science Foundation of Shanghai under the contract No. 19ZR1401700 and the Talent Introduction Start-up Foundation for Shanghai Institute of Technology under the contract No. YJ2020-12. F. Zhao acknowledges the support from National Natural Science Foundation of China under the contract No. 51906159. X. Xiao acknowledges the support from Shanghai Pujiang Program under the contract No. 20PJ1400200 and the Fundamental Research Funds for the Central Universities of China under the contract No. 2232021D-11. D. Orejon additionally acknowledges the support from the International Institute for Carbon-Neutral Energy Research (WPI-I2CNER) sponsored by the Japanese Ministry of Education, Culture, Sports, Science, and Technology; The Royal Society Research Grant 2020 Round 2 with Grant No. RGS/R2/202041; and the European Space Agency (ESA) through the project Convection and Interfacial Mass Exchange (EVAPORATION) with ESA Contract Number 4000129506/20/NL/PG.

## Graphical Abstract

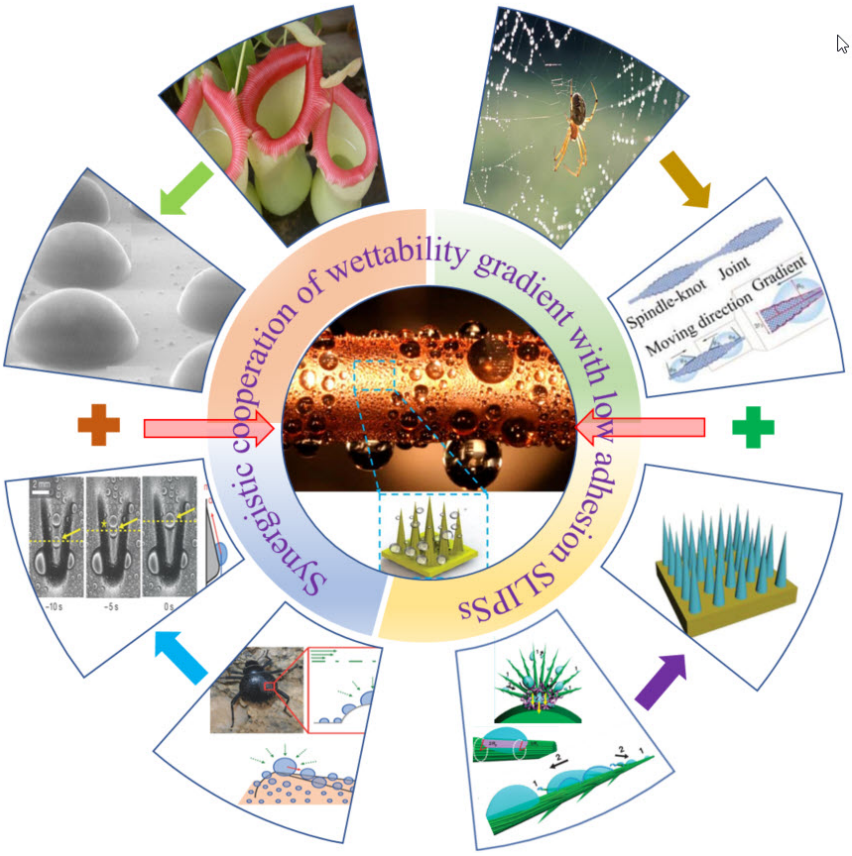

**References**


[1] Mousa MH, Miljkovic N, Nawaz K. Review of heat transfer enhancement techniques for single phase flows. Renewable and Sustainable Energy Reviews. 2021;137:110566.

[2] United Nations Sustainable Development Goal 7. https://sdgs.un.org/goals/goal7.

[3] Zheng S-F, Gross U, Wang X-D. Dropwise condensation: From fundamentals of wetting, nucleation, and droplet mobility to performance improvement by advanced functional surfaces. Advances in Colloid and Interface Science. 2021;295:102503.

[4] Thakur S, Dasmahapatra AK, Bandyopadhyay D. Functional liquid droplets for analyte sensing and energy harvesting. Advances in Colloid and Interface Science. 2021;294:102453.

[5] Khan SA, Tahir F, Baloch AAB, Koc M. Review of micro–nanoscale surface coatings application for sustaining dropwise condensation. Coatings. 2019;9:117-28.

[6] Wilkins DG, Bromley LA, Read SM. Dropwise and filmwise condensation of water vapor on gold. AIChE Journal. 1973:119-23.

[7] Graham C, Griffith P. Drop size distributions and heat transfer in dropwise condensation. International Journal of Heat and Mass Transfer. 1973;16:337-46.

[8] Westwater JW. Gold surfaces for condensation heat transfer. Gold Bulletin. 1981;14:95-101.

[9] Le Fevre EJ, Rose JW. An experimental study of heat transfer by dropwise condensation. International Journal of Heat and Mass Transfer. 1965;8:1117-33.

[10] Rose JW. Dropwise condensation theory and experiment: a review. Proceedings of the Institution of Mechanical Engineers, Part A: Journal of Power and Energy. 2002;216:115-28.

[11] Cho HJ, Preston DJ, Zhu Y, Wang EN. Nanoengineered materials for liquid–vapour phase-change heat transfer. Nature Reviews Materials. 2016;2:16092-17.

[12] Miljkovic N, Enright R, Nam Y, Lopez K, Dou N, Sack J, et al. Jumping-droplet-enhanced condensation on scalable superhydrophobic nanostructured surfaces. Nano Letters. 2012;13:179-87.

[13] Ma J, Sett S, Cha H, Yan X, Miljkovic N. Recent developments, challenges, and pathways to stable dropwise condensation: A perspective. Applied Physics Letters. 2020;116:260501.

[14] Beér JM. High efficiency electric power generation: The environmental role. Progress in Energy and Combustion Science. 2007;33:107-34.

[15] Mapped: The world's coal power plants. https://www.carbonbrief.org/mapped-worlds-coal-power-plants.

[16] Liu Z, Preston DJ. Enhanced condensation for improved energy efficiency. Joule. 2019;3:1182-4.

[17] Edalatpour M, Liu L, Jacobi AM, Eid KF, Sommers AD. Managing water on heat transfer surfaces: A critical review of techniques to modify surface wettability for applications with condensation or evaporation. Applied Energy. 2018;222:967-92.

[18] Lee Y-T, Hong S, Chien L-H, Lin C-J, Yang A-S. Heat transfer and pressure drop of film condensation in a horizontal minitube for HFO1234yf refrigerant. Applied Energy. 2020;274:115183.

[19] Zhang L, Yang S, Xu H. Experimental study on condensation heat transfer characteristics of steam on horizontal twisted elliptical tubes. Applied Energy. 2012;97:881-7.

[20] Tanasawa I. Advances in condensation heat transfer. Advances in heat transfer. 1991;21:55-139.

[21] Rose JW. Dropwise condensation theory. International Journal of Heat and Mass Transfer. 1981;24:191-4.

[22] Paxson AT, Yagüe JL, Gleason KK, Varanasi KK. Stable dropwise condensation for enhancing heat

transfer via the initiated chemical vapor deposition (iCVD) of grafted polymer films. Advanced Materials. 2014;26:418-23.
[23] Wen R, Xu S, Ma X, Lee Y-C, Yang R. Three-Dimensional Superhydrophobic Nanowire Networks for Enhancing Condensation Heat Transfer. Joule. 2018;2:269-79.
[24] Wen R, Li Q, Wu J, Wu G, Wang W, Chen Y, et al. Hydrophobic copper nanowires for enhancing condensation heat transfer. Nano Energy. 2017;33:177-83.
[25] Wen R, Lan Z, Peng B, Xu W, Yang R, Ma X. Wetting Transition of Condensed Droplets on Nanostructured Superhydrophobic Surfaces: Coordination of Surface Properties and Condensing Conditions. ACS Applied Materials & Interfaces. 2017;9:13770-7.
[26] Snustad I, Røe IT, Brunsvold A, Ervik Å, He J, Zhang Z. A review on wetting and water condensation - Perspectives for CO2 condensation. Advances in Colloid and Interface Science. 2018;256:291-304.
[27] Xiao R, Miljkovic N, Enright R, Wang EN. Immersion condensation on oil-infused heterogeneous surfaces for enhanced heat transfer. Scientific Reports. 2013;3:1988-1--6.
[28] Rykaczewski K, Paxson AT, Staymates M, Walker ML, Sun X, Anand S, et al. Dropwise condensation of low surface tension fluids on omniphobic surfaces. Scientific Reports. 2014;4:4158.
[29] Weisensee PB, Wang Y, Hongliang Q, Schultz D, King WP, Miljkovic N. Condensate droplet size distribution on lubricant-infused surfaces. International Journal of Heat and Mass Transfer. 2017;109:187-99.
[30] Sett S, Sokalski P, Boyina K, Li L, Rabbi KF, Auby H, et al. Stable dropwise condensation of ethanol and hexane on rationally designed ultrascalable nanostructured lubricant-infused surfaces. Nano Letters. 2019;19:5287-96.
[31] Preston DJ, Lu Z, Song Y, Zhao Y, Wilke KL, Antao DS, et al. Heat transfer enhancement during water and hydrocarbon condensation on lubricant infused surfaces. Scientific Reports. 2018;8:540-9.
[32] Sharma CS, Lam CWE, Milionis A, Eghlidi H, Poulikakos D. Self-sustained cascading coalescence in surface condensation. ACS Applied Materials & Interfaces. 2019;11:27435-42.
[33] Lv FY, Zhang P. Fabrication and characterization of superhydrophobic surfaces on aluminum alloy substrates. Applied Surface Science. 2014;321:166-72.
[34] Pan S, Guo R, Björnmalm M, Richardson JJ, Li L, Peng C, et al. Coatings super-repellent to ultralow surface tension liquids. Nature Materials. 2018;17:1040-7.
[35] Papadopoulos P, Mammen L, Deng X, Vollmer D, Butt H-J. How superhydrophobicity breaks down. Proceedings of the National Academy of Sciences. 2013;110:3254-8.
[36] Yeong YH, Milionis A, Loth E, Bayer IS. Microscopic receding contact line dynamics on pillar and irregular superhydrophobic surfaces. Scientific Reports. 2015;5:8384-10.
[37] Stamatopoulos C, Schutzius TM, Köppl CJ, Hayek NE, Maitra T, Hemrle J, et al. On the shedding of impaled droplets: the role of transient intervening layers. Scientific Reports. 2016;6:18875-9.
[38] Parker AR, Lawrence CR. Water capture by a desert beetle. Nature. 2001;414:33-4.
[39] Mukherjee R, Berrier AS, Murphy KR, Vieitez JR, Boreyko JB. How surface orientation affects jumping-droplet condensation. Joule. 2019;3:1360-76.
[40] Furmidge CGL. Studies at phase interfaces. I. The sliding of liquid drops on solid surfaces and a theory for spray retention. Journal of Colloid Science. 1962;17:309-24.
[41] Eral HB, 't Mannetje DJCM, Oh JM. Contact angle hysteresis: a review of fundamentals and applications. Colloid and Polymer Science. 2013;291:247-60.

[42] Anand S, Paxson AT, Dhiman R, Smith JD, Varanasi KK. Enhanced condensation on lubricant-impregnated nanotextured surfaces. ACS Nano. 2012;6:10122-9.
[43] Sharma CS, Combe J, Giger M, Emmerich T, Poulikakos D. Growth rates and spontaneous navigation of condensate droplets through randomly structured textures. ACS Nano. 2017;11:1673-82.
[44] Chavan S, Cha H, Orejon D, Nawaz K, Singla N, Yeung YF, et al. Heat transfer through a condensate droplet on hydrophobic and nanostructured superhydrophobic surfaces. Langmuir. 2016;32:7774-87.
[45] Wong T-S, Kang SH, Tang SKY, Smythe EJ, Hatton BD, Grinthal A, et al. Bioinspired self-repairing slippery surfaces with pressure-stable omniphobicity. Nature. 2011;477:443-7.
[46] Bohn HF, Federle W. Insect aquaplaning: nepenthes pitcher plants capture prey with the peristome, a fully wettable water-lubricated anisotropic surface. Proceedings of the National Academy of Sciences. 2004;101:14138-43.
[47] Villegas M, Zhang Y, Abu Jarad N, Soleymani L, Didar TF. Liquid-infused surfaces: a review of theory, design, and applications. ACS Nano. 2019;13:8517-36.
[48] Box F, Thorogood C, Guan JH. Guided droplet transport on synthetic slippery surfaces inspired by a pitcher plant. Journal of The Royal Society Interface. 2019;16:20190323-7.
[49] Baumli P, D'Acunzi M, Hegner KI, Naga A, Wong WSY, Butt H-J, et al. The challenge of lubricant-replenishment on lubricant-impregnated surfaces. Advances in Colloid and Interface Science. 2021;287:102329.
[50] Luo JT, Geraldi NR, Guan JH, McHale G, Wells GG, Fu YQ. Slippery liquid-infused porous surfaces and droplet transportation by surface acoustic waves. Physical Review Applied. 2017;7:014017-9.
[51] Zhang C, Adera S, Aizenberg J, Chen Z. Why Are Water Droplets Highly Mobile on Nanostructured Oil-Impregnated Surfaces? ACS Applied Materials & Interfaces. 2021;13:15901-9.
[52] Zhang P, Lv FY, Askounis A, Orejon D, Shen B. Role of impregnated lubricant in enhancing thermosyphon performance. International Journal of Heat and Mass Transfer. 2017;109:1229-38.
[53] Sun J, Weisensee PB. Microdroplet self-propulsion during dropwise condensation on lubricant-infused surfaces. Soft Matter. 2019;15:4808-17.
[54] Liu C, Sun Y, Huanng J, Guo Z, Liu W. External-field-induced directional droplet transport: A review. Advances in Colloid and Interface Science. 2021;295:102502.
[55] Sattari A, Hanafizadeh P, Hoorfar M. Multiphase flow in microfluidics: From droplets and bubbles to the encapsulated structures. Advances in Colloid and Interface Science. 2020;282:102208.
[56] Hui Guan J, Ruiz-Gutiérrez É, Xu BB, Wood D, McHale G, Ledesma-Aguilar R, et al. Drop transport and positioning on lubricant-impregnated surfaces. Soft Matter. 2017;13:3404-10.
[57] Azad MAK, Barthlott W, Koch K. Hierarchical surface architecture of plants as an inspiration for biomimetic fog collectors. Langmuir. 2015;31:13172-9.
[58] Zeng X, Qian L, Yuan X, Zhou C, Li Z, Cheng J, et al. Inspired by stenocara beetles: from water collection to high-efficiency water-in-oil emulsion separation. ACS Nano. 2017;11:760-9.
[59] Liu L, Liu S, Schelp M, Chen X. Rapid 3D Printing of Bioinspired Hybrid Structures for High-Efficiency Fog Collection and Water Transportation. ACS Applied Materials & Interfaces. 2021.
[60] Shi R, Tian Y, Wang L. Bioinspired Fibers with Controlled Wettability: From Spinning to Application. ACS Nano. 2021;15:7907-30.
[61] Zhang C, Zhang B, Ma H, Li Z, Xiao X, Zhang Y, et al. Bioinspired pressure-tolerant asymmetric slippery surface for continuous self-transport of gas bubbles in aqueous environment. ACS Nano.

2018;12:2048-55.
[62] Zheng Y, Cheng J, Zhou C, Xing H, Wen X, Pi P, et al. Droplet motion on a shape gradient surface. Langmuir. 2017;33:4172-7.
[63] Wang L, Shi W, Hou Y, Zhang M, Feng S, Zheng Y. Droplet transport on a nano- and microstructured surface with a wettability gradient in low-temperature or high-humidity environments. Advanced Materials Interfaces. 2015;2:1500040-7.
[64] Si Y, Wang T, Li C, Yu C, Li N, Gao C, et al. Liquids unidirectional transport on dual-scale arrays. ACS Nano. 2018;12:9214-22.
[65] Li J, Zhou X, Tao R, Zheng H, Wang Z. Directional Liquid Transport from the Cold Region to the Hot Region on a Topological Surface. Langmuir. 2021;37:5059-65.
[66] Dai H, Dong Z, Jiang L. Directional liquid dynamics of interfaces with superwettability. Science Advances. 2020;6:eabb5528.
[67] Li H, Li A, Zhao Z, Xue L, Li M, Song Y. Precise Droplet Manipulation Based on Surface Heterogeneity. Accounts of Materials Research. 2021;2:230-41.
[68] Malinowski R, Parkin IP, Volpe G. Advances towards programmable droplet transport on solid surfaces and its applications. Chemical Society Reviews. 2020.
[69] Bonn D, Eggers J, Indekeu J, Meunier J, Rolley E. Wetting and spreading. Reviews of Modern Physics. 2009;81:739-805.
[70] de Gennes PG. Wetting: statics and dynamics. Reviews of Modern Physics. 1985;57:827-63.
[71] Chaudhury MK, Whitesides GM. How to Make Water Run Uphill. Science. 1992;256:1539.
[72] Hirai Y, Mayama H, Matsuo Y, Shimomura M. Uphill Water Transport on a Wettability-Patterned Surface: Experimental and Theoretical Results. ACS Applied Materials & Interfaces. 2017;9:15814-21.
[73] Chandesris B, Soupremanien U, Dunoyer N. Uphill motion of droplets on tilted and vertical grooved substrates induced by a wettability gradient. Colloids and Surfaces A: Physicochemical and Engineering Aspects. 2013;434:126-35.
[74] Daniel S, Chaudhury MK, Chen JC. Fast Drop Movements Resulting from the Phase Change on a Gradient Surface. Science. 2001;291:633-6.
[75] Orejon D, Shardt O, Waghmare PR, Kumar Gunda NS, Takata Y, Mitra SK. Droplet migration during condensation on chemically patterned micropillars. RSC Advances. 2016;6:36698-704.
[76] Jing-Tang Y, Chen JC, Ker-Jer H, Yeh JA. Droplet manipulation on a hydrophobic textured surface with roughened patterns. Journal of Microelectromechanical Systems. 2006;15:697-707.
[77] Kita Y, Mackenzie Dover C, Askounis A, Takata Y, Sefiane K. Drop mobility on superhydrophobic microstructured surfaces with wettability contrasts. Soft Matter. 2018;14:9418-24.
[78] Shastry A, Case MJ, Böhringer KF. Directing Droplets Using Microstructured Surfaces. Langmuir. 2006;22:6161-7.
[79] Sommers AD, Panth M, Eid KF. Self-propelled water droplet movement on a laser-etched radial gradient copper surface. Applied Thermal Engineering. 2020;173:115226.
[80] Liu C, Sun J, Li J, Xiang C, Che L, Wang Z, et al. Long-range spontaneous droplet self-propulsion on wettability gradient surfaces. Scientific Reports. 2017;7:7552.
[81] Zhang S, Huang J, Chen Z, Yang S, Lai Y. Liquid mobility on superwettable surfaces for applications in energy and the environment. Journal of Materials Chemistry A. 2019;7:38-63.

[82] Daniel S, Chaudhury MK. Rectified Motion of Liquid Drops on Gradient Surfaces Induced by Vibration. Langmuir. 2002;18:3404-7.
[83] Zhao H, Orejon D, Mackenzie-Dover C, Valluri P, Shanahan MER, Sefiane K. Droplet motion on contrasting striated surfaces. Applied Physics Letters. 2020;116:251604.
[84] Zhao H, Orejon D, Sefiane K, Shanahan MER. Droplet motion and oscillation on contrasting micro-striated surfaces. Journal of Fluid Mechanics. 2021;916:A54.
[85] Ju J, Zheng Y, Jiang L. Bioinspired One-Dimensional Materials for Directional Liquid Transport. Accounts of Chemical Research. 2014;47:2342-52.
[86] Ju J, Bai H, Zheng Y, Zhao T, Fang R, Jiang L. A multi-structural and multi-functional integrated fog collection system in cactus. Nature communications. 2012;3:1247-6.
[87] Chen W, Guo Z. Hierarchical fibers for water collection inspired by spider silk. Nanoscale. 2019;11:15448-63.
[88] Lorenceau É, QuÉRÉ D. Drops on a conical wire. Journal of Fluid Mechanics. 2004;510:29-45.
[89] Ju J, Xiao K, Yao X, Bai H, Jiang L. Bioinspired conical copper wire with gradient wettability for continuous and efficient fog collection. Advanced Materials. 2013;25:5937-42.
[90] Yilbas BS, Al-Sharafi A, Ali H, Al-Aqeeli N. Dynamics of a water droplet on a hydrophobic inclined surface: influence of droplet size and surface inclination angle on droplet rolling. RSC Advances. 2017;7:48806-18.
[91] Smith JD, Dhiman R, Anand S, Reza-Garduno E, Cohen RE, McKinley GH, et al. Droplet mobility on lubricant-impregnated surfaces. Soft Matter. 2013;9:1772-80.
[92] Boreyko JB, Polizos G, Datskos PG, Sarles SA, Collier CP. Air-stable droplet interface bilayers on oil-infused surfaces. Proceedings of the National Academy of Sciences. 2014;111:7588-93.
[93] Pham QN, Zhang S, Montazeri K, Won Y. Droplets on slippery lubricant-infused porous surfaces: a macroscale to nanoscale perspective. Langmuir. 2018;34:14439-47.
[94] Maeda Y, Lv F, Zhang P, Takata Y, Orejon D. Condensate droplet size distribution and heat transfer on hierarchical slippery lubricant infused porous surfaces. Applied Thermal Engineering. 2020;176:115386.
[95] Günay AA, Sett S, Ge Q, Zhang T, Miljkovic N. Cloaking Dynamics on Lubricant-Infused Surfaces. Advanced Materials Interfaces. 2020;7:2000983.
[96] Malik FT, Clement RM, Gethin DT, Krawszik W, Parker AR. Nature's moisture harvesters: a comparative review. Bioinspiration & Biomimetics. 2014;9:031002.
[97] Wang J, Yi S, Yang Z, Chen Y, Jiang L, Wong C-P. Laser Direct Structuring of Bioinspired Spine with Backward Microbarbs and Hierarchical Microchannels for Ultrafast Water Transport and Efficient Fog Harvesting. ACS Applied Materials & Interfaces. 2020;12:21080-7.
[98] Zheng Y, Bai H, Huang Z, Tian X, Nie F-Q, Zhao Y, et al. Directional water collection on wetted spider silk. Nature. 2010;463:640-3.
[99] Park K-C, Kim P, Grinthal A, He N, Fox D, Weaver JC, et al. Condensation on slippery asymmetric bumps. Nature. 2016;531:78-82.
[100] Launay G, Sadullah MS, McHale G, Ledesma-Aguilar R, Kusumaatmaja H, Wells GG. Self-propelled droplet transport on shaped-liquid surfaces. Scientific Reports. 2020;10:14987.
[101] Daniel D, Timonen JVI, Li R, Velling SJ, Aizenberg J. Oleoplaning droplets on lubricated surfaces. Nature Physics. 2017;13:1020-7.

[102] Yu L, Chen GY, Xu H, Liu X. Substrate-independent, transparent oil-repellent coatings with self-healing and persistent easy-sliding oil repellency. ACS Nano. 2016;10:1076-85.
[103] Howell C, Grinthal A, Sunny S, Aizenberg M, Aizenberg J. Designing liquid-infused surfaces for medical applications: a review. Advanced Materials. 2018;30:1802724-26.
[104] Zhang P, Lv FY. A review of the recent advances in superhydrophobic surfaces and the emerging energy-related applications. Energy. 2015;82:1068-87.
[105] Togasawa R, Ohnuki F, Shiratori S. A biocompatible slippery surface based on a boehmite nanostructure with omniphobicity for hot liquids and boiling stability. ACS Applied Nano Materials. 2018;1:1758-65.
[106] Wang J, Kato K, Blois AP, Wong T-S. Bioinspired omniphobic coatings with a thermal self-repair function on industrial materials. ACS Applied Materials & Interfaces. 2016;8:8265-71.
[107] Jing X, Guo Z. Durable lubricant-impregnated surfaces for water collection under extremely severe working conditions. ACS Applied Materials & Interfaces. 2019;11:35949-58.
[108] Guo L, Tang GH. Dropwise condensation on bioinspired hydrophilic-slippery surface. RSC Advances. 2018;8:39341-51.
[109] Lee C, Kim H, Nam Y. Drop impact dynamics on oil-Infused nanostructured surfaces. Langmuir. 2014;30:8400-7.
[110] Zhu J-L, Shi W-Y, Wang T-S, Feng L. Spontaneous thermocapillary motion of condensation droplets. Applied Physics Letters. 2020;116:243703.
[111] Seo D, Lee J, Lee C, Nam Y. The effects of surface wettability on the fog and dew moisture harvesting performance on tubular surfaces. Scientific Reports. 2016;6:24276-11.
[112] Preston DJ, Song Y, Lu Z, Antao DS, Wang EN. Design of lubricant infused surfaces. ACS Applied Materials & Interfaces. 2017;9:42383-92.
[113] Solomon BR, Khalil KS, Varanasi KK. Drag reduction using lubricant-impregnated surfaces in viscous laminar flow. Langmuir. 2014;30:10970-6.
[114] Dai X, Sun N, Nielsen SO, Stogin BB, Wang J, Yang S, et al. Hydrophilic directional slippery rough surfaces for water harvesting. Science Advances. 2018;4:0919-1--10.
[115] Tripathy A, Lam CWE, Davila D, Donati M, Milionis A, Sharma CS, et al. Ultrathin Lubricant-Infused Vertical Graphene Nanoscaffolds for High-Performance Dropwise Condensation. ACS Nano. 2021.
[116] Laney SK, Michalska M, Li T, Ramirez FV, Portnoi M, Oh J, et al. Delayed Lubricant Depletion of Slippery Liquid Infused Porous Surfaces Using Precision Nanostructures. Langmuir. 2021;37:10071-8.
[117] Yan X, Chen F, Sett S, Chavan S, Li H, Feng L, et al. Hierarchical condensation. ACS Nano. 2019;13:8169-84.
[118] Li J, Zheng H, Yang Z, Wang Z. Breakdown in the directional transport of droplets on the peristome of pitcher plants. Communications Physics. 2018;1:35-7.
[119] Zhong L, Zhang R, Li J, Guo Z, Zeng H. Efficient fog harvesting based on 1D copper wire inspired by the plant pitaya. Langmuir. 2018;34:15259-67.
[120] Heng X, Xiang M, Lu Z, Luo C. Branched ZnO wire structures for water collection inspired by cacti. ACS Applied Materials & Interfaces. 2014;6:8032-41.
[121] Yu Z, Yun FF, Wang Y, Yao L, Dou S, Liu K, et al. Desert beetle-inspired superwettable patterned

surfaces for water harvesting. Small. 2017;13:1701403-6.
[122] Bai H, Ju J, Sun R, Chen Y, Zheng Y, Jiang L. Controlled fabrication and water collection ability of bioinspired artificial spider silks. Advanced Materials. 2011;23:3708-11.
[123] Hernández SC, Bennett CJC, Junkermeier CE, Tsoi SD, Bezares FJ, Stine R, et al. Chemical gradients on graphene to drive droplet motion. ACS Nano. 2013;7:4746-55.
[124] Feng S, Wang S, Liu C, Zheng Y, Hou Y. Controlled droplet transport on a gradient adhesion surface. Chemical Communications. 2015;51:6010-3.
[125] Wang S, Feng S, Hou Y, Zheng Y. Controlling of water collection ability by an elasticity-regulated bioinspired fiber. Macromolecular Rapid Communications. 2015;36:459-64.
[126] Xing Y, Wang S, Feng S, Shang W, Deng S, Wang L, et al. Controlled transportation of droplets and higher fog collection efficiency on a multi-scale and multi-gradient copper wire. RSC Advances. 2017;7:29606-10.
[127] Wu X, Bai H, Zhang J, Chen Fe, Shi G. Copper Hydroxide Nanoneedle and Nanotube Arrays Fabricated by Anodization of Copper. The Journal of Physical Chemistry B. 2005;109:22836-42.
[128] Xiao X, Zhang C, Ma H, Zhang Y, Liu G, Cao M, et al. Bioinspired slippery cone for controllable manipulation of gas bubbles in low-surface-tension environment. ACS Nano. 2019;13:4083-90.
[129] Feng S, Wang S, Gao L, Li G, Hou Y, Zheng Y. Controlled directional water-droplet spreading on a high-adhesion surface. Angewandte Chemie International Edition. 2014;53:6163-7.
[130] Feng S, Wang S, Tao Y, Shang W, Deng S, Zheng Y, et al. Radial Wettable Gradient of Hot Surface to Control Droplets Movement in Directions. Scientific Reports. 2015;5:10067.
[131] Ghosh A, Ganguly R, Schutzius TM, Megaridis CM. Wettability patterning for high-rate, pumpless fluid transport on open, non-planar microfluidic platforms. Lab on a Chip. 2014;14:1538-50.
[132] Wu H, Zhu K, Cao B, Zhang Z, Wu B, Liang L, et al. Smart design of wettability-patterned gradients on substrate-independent coated surfaces to control unidirectional spreading of droplets. Soft Matter. 2017;13:2995-3002.
[133] Xing Y, Shang W, Wang Q, Feng S, Hou Y, Zheng Y. Integrative bioinspired surface with wettable patterns and gradient for enhancement of fog collection. ACS Applied Materials & Interfaces. 2019;11:10951-8.
[134] Luo C. Theoretical exploration of barrel-shaped drops on cactus spines. Langmuir. 2015;31:11809-13.
[135] Liang Y-E, Tsao H-K, Sheng Y-J. Drops on hydrophilic conical fibers: gravity effect and coexistent states. Langmuir. 2015;31:1704-10.
[136] Xu T, Lin Y, Zhang M, Shi W, Zheng Y. High-efficiency fog collector: water unidirectional transport on heterogeneous rough conical wires. ACS Nano. 2016;10:10681-8.
[137] Yu C, Cao M, Dong Z, Wang J, Li K, Jiang L. Spontaneous and directional transportation of gas bubbles on superhydrophobic cones. Advanced Functional Materials. 2016;26:3236-43.
[138] Peng Y, He Y, Yang S, Ben S, Cao M, Li K, et al. Magnetically induced fog harvesting via flexible conical arrays. Advanced Functional Materials. 2015;25:5967-71.
[139] Huang Y, Stogin BB, Sun N, Wang J, Yang S, Wong T-S. A switchable cross-species liquid repellent surface. Advanced Materials. 2017;29:1604641-7.
[140] Zhou H, Zhang M, Li C, Gao C, Zheng Y. Excellent fog-droplets collector via integrative janus membrane and conical spine with micro/nanostructures. Small. 2018;14:1801335-7.

[141] Wen C, Guo H, Bai H, Xu T, Liu M, Yang J, et al. Beetle-inspired hierarchical antibacterial interface for reliable fog harvesting. ACS Applied Materials & Interfaces. 2019;11:34330-7.
[142] Ghosh A, Beaini S, Zhang BJ, Ganguly R, Megaridis CM. Enhancing dropwise condensation through bioinspired wettability patterning. Langmuir. 2014;30:13103-15.
[143] Chen H, Zhang L, Zhang P, Zhang D, Han Z, Jiang L. A novel bioinspired continuous unidirectional liquid spreading surface structure from the peristome surface of nepenthes alata. Small. 2017;13:1601676-6.
[144] Chen H, Zhang P, Zhang L, Liu H, Jiang Y, Zhang D, et al. Continuous directional water transport on the peristome surface of nepenthes alata. Nature. 2016;532:85-9.
[145] Yu C, Zhang L, Ru Y, Li N, Li C, Gao C, et al. Drop cargo transfer via unidirectional lubricant spreading on peristome-mimetic surface. ACS Nano. 2018;12:11307-15.
[146] Zhou S, Yu C, Li C, Dong Z, Jiang L. Programmable unidirectional liquid transport on peristome-mimetic surfaces under liquid environments. Journal of Materials Chemistry A. 2019;7:18244-8.
[147] Wang D, Zhang X, Zhang D. Fabrication of a Peristome Surface Structure of Nepenthes alata by Elliptical Vibration Cutting. Nanomanufacturing and Metrology. 2018;1:209-16.
[148] Tian X, Chen Y, Zheng Y, Bai H, Jiang L. Controlling water capture of bioinspired fibers with hump structures. Advanced Materials. 2011;23:5486-91.
[149] Xue Y, Chen Y, Wang T, Jiang L, Zheng Y. Directional size-triggered microdroplet target transport on gradient-step fibers. Journal of Materials Chemistry A. 2014;2:7156-60.
[150] Quéré D. Thin films flowing on vertical fibers. Europhysics Letters (EPL). 1990;13:721-6.
[151] Dong H, Wang N, Wang L, Bai H, Wu J, Zheng Y, et al. Bioinspired electrospun knotted microfibers for fog harvesting. Chemphyschem : a European Journal of Chemical Physics and Physical Chemistry. 2012;13:1153-6.
[152] Thakur N, Ranganath AS, Agarwal K, Baji A. Electrospun bead-on-string hierarchical fibers for fog harvesting application. Macromolecular Materials and Engineering. 2017;302:1700124-9.
[153] Li C, Liu Y, Gao C, Li X, Xing Y, Zheng Y. Fog harvesting of a bioinspired nanocone-decorated 3D fiber network. ACS Applied Materials & Interfaces. 2019;11:4507-13.
[154] Chen Y, Li K, Zhang S, Qin L, Deng S, Ge L, et al. Bioinspired Superwettable Microspine Chips with Directional Droplet Transportation for Biosensing. ACS Nano. 2020;14:4654-61.
[155] Bai H, Zhao T, Wang X, Wu Y, Li K, Yu C, et al. Cactus kirigami for efficient fog harvesting: simplifying a 3D cactus into 2D paper art. Journal of Materials Chemistry A. 2020;8:13452-8.
[156] Kajiya T, Wooh S, Lee Y, Char K, Vollmer D, Butt H-J. Cylindrical chains of water drops condensing on microstructured lubricant-infused surfaces. Soft Matter. 2016;12:9377-82.
[157] Lin J, Tan X, Shi T, Tang Z, Liao G. Leaf vein-inspired hierarchical wedge-shaped tracks on flexible substrate for enhanced directional water collection. ACS Applied Materials & Interfaces. 2018;10:44815-24.
[158] Liang X, Li D, Li S, Xu C, Guo Z. Artificial Leaf for Switchable Droplet Manipulation. Langmuir. 2021;37:5745-52.
[159] Liu W, Fan P, Cai M, Luo X, Chen C, Pan R, et al. An integrative bioinspired venation network with ultra-contrasting wettability for large-scale strongly self-driven and efficient water collection. Nanoscale. 2019;11:8940-9.
[160] Lv X, Jiao Y, Wu S, Li C, Zhang Y, Li J, et al. Anisotropic Sliding of Underwater Bubbles On

Microgrooved Slippery Surfaces by One-Step Femtosecond Laser Scanning. ACS Applied Materials & Interfaces. 2019;11:20574-80.
[161] Jiao Y, Lv X, Zhang Y, Li C, Li J, Wu H, et al. Pitcher plant-bioinspired bubble slippery surface fabricated by femtosecond laser for buoyancy-driven bubble self-transport and efficient gas capture. Nanoscale. 2019;11:1370-8.
[162] Wang Y, Liang X, Ma K, Zhang H, Wang X, Xin JH, et al. Nature-inspired windmill for water collection in complex windy environments. ACS Applied Materials & Interfaces. 2019;11:17952-9.
[163] El Fil B, Kini G, Garimella S. A review of dropwise condensation: Theory, modeling, experiments, and applications. International Journal of Heat and Mass Transfer. 2020;160:120172.
[164] Dai X, Stogin BB, Yang S, Wong T-S. Slippery wenzel state. ACS Nano. 2015;9:9260-7.
[165] Liu X, Cheng P. Dropwise condensation theory revisited part II. droplet nucleation density and condensation heat flux. International Journal of Heat and Mass Transfer. 2015;83:842-9.
[166] Tress M, Karpitschka S, Papadopoulos P, Snoeijer JH, Vollmer D, Butt H-J. Shape of a sessile drop on a flat surface covered with a liquid film. Soft Matter. 2017;13:3760-7.
[167] Karpitschka S, Pandey A, Lubbers LA, Weijs JH, Botto L, Das S, et al. Liquid drops attract or repel by the inverted cheerios effect. Proceedings of the National Academy of Sciences. 2016;113:7403-7.
[168] Carre A, Gastel J-C, Shanahan MER. Viscoelastic effects in the spreading of liquids. Nature. 1996;379:432-4.
[169] Schellenberger F, Xie J, Encinas N, Hardy A, Klapper M, Papadopoulos P, et al. Direct observation of drops on slippery lubricant-infused surfaces. Soft Matter. 2015;11:7617-26.
[170] Wooh S, Butt H-J. A photocatalytically active lubricant-impregnated surface. Angewandte Chemie International Edition. 2017;56:4965-9.
[171] Sadullah MS, Semprebon C, Kusumaatmaja H. Drop dynamics on liquid-infused surfaces: the role of the lubricant ridge. Langmuir. 2018;34:8112-8.
[172] Ge Q, Raza A, Li H, Sett S, Miljkovic N, Zhang T. Condensation of Satellite Droplets on Lubricant-Cloaked Droplets. ACS Applied Materials & Interfaces. 2020;12:22246-55.
[173] Anand S, Rykaczewski K, Subramanyam SB, Beysens D, Varanasi KK. How droplets nucleate and grow on liquids and liquid impregnated surfaces. Soft Matter. 2015;11:69-80.
[174] Kajiya T, Schellenberger F, Papadopoulos P, Vollmer D, Butt H-J. 3D imaging of water-drop condensation on hydrophobic and hydrophilic lubricant-impregnated surfaces. Scientific Reports. 2016;6:23687-10.
[175] Sun J, Jiang X, Weisensee PB. Enhanced Water Nucleation and Growth Based on Microdroplet Mobility on Lubricant-Infused Surfaces. Langmuir. 2021;37:12790-801.
[176] Kreder MJ, Daniel D, Tetreault A, Cao Z, Lemaire B, Timonen JVI, et al. Film dynamics and lubricant depletion by droplets moving on lubricated surfaces. Physical Review X. 2018;8:031053-16.
[177] Gulfam R, Orejon D, Choi C-H, Zhang P. Phase-Change Slippery Liquid-Infused Porous Surfaces with Thermo-Responsive Wetting and Shedding States. ACS Applied Materials & Interfaces. 2020;12:34306-16.
[178] Yao Y, Aizenberg J, Park K-C. Dropwise condensation on hydrophobic bumps and dimples. Applied Physics Letters. 2018;112:151605-4.
[179] Keiser A, Keiser L, Clanet C, Quéré D. Drop friction on liquid-infused materials. Soft Matter. 2017;13:6981-7.

[180] Rapoport L, Solomon BR, Varanasi KK. Mobility of yield stress fluids on lubricant-impregnated surfaces. ACS Applied Materials & Interfaces. 2019;11:16123-9.
[181] Li H, Aili A, Alhosani MH, Ge Q, Zhang T. Directional passive transport of microdroplets in oil-infused diverging channels for effective condensate removal. ACS Applied Materials & Interfaces. 2018;10:20910-9.
[182] Sirohia GK, Dai X. Designing air-independent slippery rough surfaces for condensation. International Journal of Heat and Mass Transfer. 2019;140:777-85.
[183] Baratian D, Dey R, Hoek H, van den Ende D, Mugele F. Breath Figures under Electrowetting: Electrically Controlled Evolution of Drop Condensation Patterns. Physical Review Letters. 2018;120:214502.
[184] Wikramanayake ED, Perry J, Bahadur V. AC electrowetting promoted droplet shedding on hydrophobic surfaces. Applied Physics Letters. 2020;116:193701.
[185] Moradi M, Chini SF, Rahimian MH. Vibration-enhanced condensation heat transfer on superhydrophobic surfaces: An experimental study. AIP Advances. 2020;10:095123.
[186] Seo D, Shim J, Lee C, Nam Y. Brushed lubricant-impregnated surfaces (BLIS) for long-lasting high condensation heat transfer. Scientific Reports. 2020;10:2959.
[187] Holmes HR, Böhringer KF. Transport velocity of droplets on ratchet conveyors. Advances in Colloid and Interface Science. 2018;255:18-25.
[188] Ju J, Yao X, Yang S, Wang L, Materials LJJAF. Cactus stem inspired cone-arrayed surfaces for efficient fog collection. Advanced Functional Materials. 2014;24:6933-8.
[189] Liu C, Xue Y, Chen Y, Zheng Y. Effective directional self-gathering of drops on spine of cactus with splayed capillary arrays. Scientific Reports. 2015;5:17757-8.
[190] Alheshibri MH, Rogers NG, Sommers AD, Eid KF. Spontaneous movement of water droplets on patterned Cu and Al surfaces with wedge-shaped gradients. Applied Physics Letters. 2013;102:174103-4.
[191] Chowdhury IU, Sinha Mahapatra P, Sen AK. Self-driven droplet transport: effect of wettability gradient and confinement. Physics of Fluids. 2019;31:042111-12.
[192] Xianhua T, Yiying Z, Tielin S, Zirong T, Guanglan L. Patterned gradient surface for spontaneous droplet transportation and water collection: simulation and experiment. Journal of Micromechanics and Microengineering. 2016;26:115009-9.
[193] Wang M, Liu Q, Zhang H, Wang C, Wang L, Xiang B, et al. Laser direct writing of tree-shaped hierarchical cones on a superhydrophobic film for high-efficiency water collection. ACS Applied Materials & Interfaces. 2017;9:29248-54.
[194] Kai H, Toyosato R, Nishizawa M. Space-filling open microfluidic channels designed to collect water droplets. RSC Advances. 2018;8:15985-90.
[195] Huang J-J, Huang H, Wang X. Numerical study of drop motion on a surface with stepwise wettability gradient and contact angle hysteresis. Physics of Fluids. 2014;26:062101-44.
[196] Prakash M, Quéré D, Bush JWM. Surface tension transport of prey by feeding shorebirds: The capillary ratchet. Science. 2008;320:931-394.
[197] Chan DYC, Klaseboer E, Manica R. Film drainage and coalescence between deformable drops and bubbles. Soft Matter. 2011;7:2235-64.
[198] Pinchasik B-E, Kappl M, Butt H-J. Small structures, big droplets: the role of nanoscience in fog

harvesting. ACS Nano. 2016;10:10627-30.
[199] Bai F, Wu J, Gong G, Guo L. Biomimetic “cactus spine” with hierarchical groove structure for efficient fog collection. Advanced Science. 2015;2:1500047-5.
[200] Chen H, Ran T, Gan Y, Zhou J, Zhang Y, Zhang L, et al. Ultrafast water harvesting and transport in hierarchical microchannels. Nature Materials. 2018;17:935-42.
[201] Li J, Song Y, Zheng H, Feng S, Xu W, Wang Z. Designing biomimetic liquid diodes. Soft Matter. 2019;15:1902-15.
[202] Jiang Y, Savarirayan S, Yao Y, Park K-C. Fog collection on a superhydrophilic wire. Applied Physics Letters. 2019;114:083701-5.
[203] Liu J, li S. Capillarity-driven migration of small objects: A critical review. The European Physical Journal E. 2019;42.
[204] Hu R, Wang N, Hou L, Cui Z, Liu J, Li D, et al. A bioinspired hybrid membrane with wettability and topology anisotropy for highly efficient fog collection. Journal of Materials Chemistry A. 2019;7:124-32.
[205] Yan X, Huang Z, Sett S, Oh J, Cha H, Li L, et al. Atmosphere-mediated superhydrophobicity of rationally designed micro/nanostructured surfaces. ACS Nano. 2019;13:4160-73.
[206] Yan X, Zhang L, Sett S, Feng L, Zhao C, Huang Z, et al. Droplet jumping: effects of droplet size, surface structure, pinning, and liquid properties. ACS Nano. 2019;13:1309-23.
[207] Liu C, Ju J, Zheng Y, Jiang L. Asymmetric ratchet effect for directional transport of fog drops on static and dynamic butterfly wings. ACS Nano. 2014;8:1321-9.
[208] Zhu Y, Tso CY, Ho TC, Leung MKH, Yao S. Coalescence-Induced Jumping Droplets on Nanostructured Biphilic Surfaces with Contact Electrification Effects. ACS Applied Materials & Interfaces. 2021;13:11470-9.
[209] Wu J, Wang N, Wang L, Dong H, Zhao Y, Jiang L. Unidirectional water-penetration composite fibrous film via electrospinning. Soft Matter. 2012;8:5996-9.
[210] Cao M, Li K, Dong Z, Yu C, Yang S, Song C, et al. Superhydrophobic “pump”: continuous and spontaneous antigravity water delivery. Advanced Functional Materials. 2015;25:4114-9.
[211] Wang Z, Li Y, Li S, Guo J, Zhang S. Janus porous membrane with conical nanoneedle channel for rapid unidirectional water transport. Chemical Communications. 2018;54:10954-7.
[212] Kashchiev D. Nucleation: Basic theory with applications. Oxford: Butterworth-Heinemann; 2000.
[213] Rose JW, Glicksman LR. Dropwise condensation—The distribution of drop sizes. International Journal of Heat and Mass Transfer. 1973;16:411-25.
[214] Ho JY, Rabbi KF, Sett S, Wong TN, Miljkovic N. Dropwise condensation of low surface tension fluids on lubricant-infused surfaces: Droplet size distribution and heat transfer. International Journal of Heat and Mass Transfer. 2021;172:121149.
[215] Lv FY, Zhang P, Orejon D, Askounis A, Shen B. Heat transfer performance of a lubricant-infused thermosyphon at various filling ratios. International Journal of Heat and Mass Transfer. 2017;115, Part A:725-36.
[216] Tsuchiya H, Tenjimbayashi M, Moriya T, Yoshikawa R, Sasaki K, Togasawa R, et al. Liquid-infused smooth surface for improved condensation heat transfer. Langmuir. 2017;33:8950-60.
[217] Medici M-G, Mongruel A, Royon L, Beysens D. Edge effects on water droplet condensation. Physical Review E. 2014;90:062403-12.

[218] Kim P, Kreder MJ, Alvarenga J, Aizenberg J. Hierarchical or Not? Effect of the Length Scale and Hierarchy of the Surface Roughness on Omniphobicity of Lubricant-Infused Substrates. Nano Letters. 2013;13:1793-9.

[219] Wong WSY, Hegner KI, Donadei V, Hauer L, Naga A, Vollmer D. Capillary Balancing: Designing Frost-Resistant Lubricant-Infused Surfaces. Nano Letters. 2020;20:8508-15.

[220] Sett S, Yan X, Barac G, Bolton LW, Miljkovic N. Lubricant-Infused Surfaces for Low-Surface-Tension Fluids: Promise versus Reality. ACS Applied Materials & Interfaces. 2017;9:36400-8.

[221] Sett S, Oh J, Cha H, Veriotti T, Bruno A, Yan X, et al. Lubricant-Infused Surfaces for Low-Surface-Tension Fluids: The Extent of Lubricant Miscibility. ACS Applied Materials & Interfaces. 2021;13:23121-33.

[222] Adera S, Alvarenga J, Shneidman AV, Zhang CT, Davitt A, Aizenberg J. Depletion of Lubricant from Nanostructured Oil-Infused Surfaces by Pendant Condensate Droplets. ACS Nano. 2020;14:8024-35.

[223] Sheng Z, Ding Y, Li G, Fu C, Hou Y, Lyu J, et al. Solid–Liquid Host–Guest Composites: The Marriage of Porous Solids and Functional Liquids. Advanced Materials. 2021;2104851-31.

[224] Lee J, Shin S, Jiang Y, Jeong C, Stone HA, Choi C-H. Oil-Impregnated Nanoporous Oxide Layer for Corrosion Protection with Self-Healing. Advanced Functional Materials. 2017;27:1606040-11.

[225] Veronesi F, Guarini G, Corozzi A, Raimondo M. Evaluation of the Durability of Slippery, Liquid-Infused Porous Surfaces in Different Aggressive Environments: Influence of the Chemical-Physical Properties of Lubricants. 2021;11:1170.

[226] Wang D, Sun Q, Hokkanen MJ, Zhang C, Lin F-Y, Liu Q, et al. Design of robust superhydrophobic surfaces. Nature. 2020;582:55-9.

[227] Chang HC, Rajagopal MC, Hoque MJ, Oh J, Li L, Li J, et al. Composite Structured Surfaces for Durable Dropwise Condensation. International Journal of Heat and Mass Transfer. 2020;156:119890.

[228] Li M, Chen Y, Luo W, Cheng X. Durable and Flexible Hydrophobic Surface with a Micropatterned Composite Metal–Polymer Structure. Langmuir. 2021;37:5838-45.